ABSTRACT

Title of Document: FORMATION AND PIEZOELECTRICITY OF SELF-ASSEMBLED $PbTiO_3$-$CoFe_2O_4$ NANOSTRUCTURAL FILMS

Zhuopeng Tan, Doctor of Philosophy, 2008

Directed By: Professor Alexander L. Roytburd,
Dept. of Materials Science and Engineering

Dr. Igor Levin,
National Institute of Standards and Technology

Main tasks of our research include: (1) exploring optimum growth conditions for PLD deposition of self-assembled nanophase $PbTiO_3$-$CoFe_2O_4$ films with different compositions and orientations; (2) analyzing morphologies and nanostructures of the two-phase films to clarify relative effects of elastic energy and interface energy on the self-assembled film formation; (3) investigating stress state and relaxation of stresses arising as a result of a paraelectric-ferroelectric transformation in $PbTiO_3$; (4) exploring ferroelectric state in the confined $PbTiO_3$ nanophase in the films with {110} and {111} orientations.

Principal results of the research are: (1). Optimum PLD growth conditions to obtain high quality films with distinct separation of epitaxial $PbTiO_3$ and $CoFe_2O_4$ nanophases are found after systematic studies. (2). Nano-facets along {111} plane between $PbTiO_3$ and $CoFe_2O_4$ phases are found to be generic in addition to

orientation dependent macroscopic interfaces. We have concluded that accounting of interface and surface energies is important for description of nano-faceting of interfaces and the near substrate zone of the films while the two-phase morphologies are determined by the elastic interactions; (3). The investigation of the stress state of the {001} film arising due to paraelectric-ferroelectric transition of $PbTiO_3$ have discovered the polydomain nanostructure of the ferroelectric phase with ~50-60% *c*-domains. Piezoresponse of $PbTiO_3$ should be reduced dramatically by combined effects of dissolution of Fe in $PbTiO_3$, *a* domains and constraints. The relative large d_{zz} from previous research must contain large extrinsic contribution due to movement of nano-domain walls. (4). Switching spectroscopy piezoresponse force microscopy (SS-PFM) is used to characterize local piezo- ferroelectric property of confined ferroelectrics in {110} and {111} films with composition of $1/3PbTiO_3$-$2/3CoFe_2O_4$. It is proved that $PbTiO_3$ nano-inclusions exhibit ferroelectricity in both films. 180^o domain switching is observed under measurement condition (<10V) for the {110} films but not for the {111} film. Quantitatively, both films yield a piezoresponse of about 15% compared to bulk single crystal $PbTiO_3$. It is a reasonable value of intrinsic piezoeffect taking into account mechanical and electrical constraints (depolarizing field) as well as the effect of Fe dissolution and possible in-plane domains.

FORMATION AND PIEZOELECTRICITY OF SELF-ASSEMBLED $PbTiO_3$-$CoFe_2O_4$ NANOSTRUCTURAL FILMS

By

Zhuopeng Tan

Dissertation submitted to the Faculty of the Graduate School of the
University of Maryland, College Park, in partial fulfillment
of the requirements for the degree of
Doctor of Philosophy
2008

Advisory Committee:
Professor Alexander L. Roytburd, Chair
Dr. Igor Levin, Co-advisor
Professor Manfred Wuttig
Associate Professor Ichiro Takeuchi
Associate Professor Hugh Bruck

© Copyright by
Zhuopeng Tan
2008

Dedication

To my parents and my sister

for their unconditional love and never-ending support

Acknowledgements

I would like to thank my knowledgeable advisor, Alexander L. Roytburd, for his support, encouragement and guidance. Without his help, I would not be able to finish my my dissertation. I would also like to thank Dr. Igor Levin serving as my co-advisor for his great effort, very productive discussions and advices.

I would like to acknowledge the many individuals who contribute to this work either directly or indirectly including but not limited to:

National Institute of Standards and Technology (Gaithersburg, MD)

Dr. Peter Schenck, Dr. Kao-Shuo Chang, Dr. Leonid A. Bendersky, Dr. Albert V. Davydov, Dr. Alexander J. Shapiro, Dr. Julia Slutsker, Dr. Guang-Yao Liu, Dr. Jian-Hua Li, Ms. Sandra W. Claggett

Oak Ridge National Laboratory (Oak Ridge, TN)

Dr. Sergei V. Kalinin, Dr. Art Baddorf, Dr. Brian Rodriguez, Dr. Katyayani Seal, Dr. Stephen Jesse

.

Table of Contents

Dedication ii
Acknowledgements iii
Table of Contents iv
List of Tables vi
List of Figures vii
Chapter 1 Introduction 1
Chapter 2 Thermodynamic Aspects of Epitaxial Self-Assembled Nanostructures 5
2.1 Introduction 5
2.2 Elastic Energy vs. Surface Energy Anisotropy 7
    2.21. Elastic Energy Approach 7
    2.2.2 Surface Energy Anisotropy Approach 12
2.3 Conclusion 14

Chapter 3 Growth of Epitaxial Self-Assembled Nanostructures of xPbTiO$_3$-(1-x)CoFe$_2$O$_4$ Using Pulsed Laser Deposition 16

3.1. Introduction 16
3.2. Experiment Setup 17
3.3. Effects of Growth Parameters 18
    3.3.1. Substrate Temperature 18
    3.3.2. Laser Fluence, O2 Pressure and Target-Substrate Distance 24

3.4 Intrinsic and Extrinsic Shortcomings of PLD System 30
3.5 Conclusion 37

Chapter 4 Morphology and Nanostructure of PbTiO$_3$-CoFe$_2$O$_4$ Films 39

4.1 Introduction 39
4.2 Bottom Zone Morphology and Interfaces 42
4.3 Main Zone: Morphology and Interface Nanostructure 46
    4.3.1 Interface Nanostructure for (001) Oriented Films 46
    4.3.2 Interface Nanostructures for (110) Oriented Films 49
    4.3.3 Interface Nanostructures for (111) Oriented Films 52
4.4 Top Zone Structures 54
4.5 Discussion and Conclusion 55

Chapter 5 Accommodation of Transformation Strains in Self-Assembled CoFe$_2$O$_4$-PbTiO$_3$ Nanostructures 58

5.1 Introduction 58

5.2 Experiments……………………………………………………………58
5.3 Effect of Constraint on T_c and Nanostructure of $PbTiO_3$ ……………………64
5.4 Conclusion……………………………………………………………72

Chapter 6 Piezoelectric Properties of Nano-$PbTiO_3$ Ferroelectrics Embedded in Ferromagnetic Film……………………………………………73

6.1 Introduction……………………………………………………………73
6.2 Measurement techniques………………………………………………74
  6.2.1 Conventional PFM Qualitative Measurement…………………………74
  6.2.2 Quantitative Hysteresis Loop Acquisition……………………………77
  6.2.3 Switching Spectroscopy piezoresponse force microscopy………………82
6.3 Experimental Results obtained by SS-PFM………………………………85
  6.3.1 SS-PFM Results for (110) Oriented Thin Film…………………………86
  6.3.2 SS-PFM Results for (111) Oriented Thin Film…………………………88
  6.3.3 SS-PFM Results for (001) Oriented Thin Film…………………………89
  6.3.4 Lateral Piezoresponse…………………………………………………89
6.4 Discussion……………………………………………………………90
6.5 Conclusion……………………………………………………………95

Summary……………………………………………………………97

Appendices…………………………………………………………101
Bibliography………………………………………………………102

List of Tables

Table 3.1 Oxide film growth temperatures……………….………..…………………..19

Table 3.2 Growth parameters and qualities of 2/3$CoFe_2O_4$-1/3$PbTiO_3$ films.………21

Table 3.3 Result of EDAX scanning on the 2/3$CoFe_2O_4$+1/3$PbTiO_3$ target surface after deposition……………………………………………………………………..34

Table 3.4 List of vapor pressure for target chemical elements [64]…………………34

Table 3.5 Result of EDAX scanning on the well area on the 2/3$CoFe_2O_4$+1/3$PbTiO_3$ target surface after deposition. (Refer to figure 3.10 for scanning area and the scanning spectrum)……………………………………...…...…………………35

Table 5.1 Room temperature values of lattice parameters of $PbTiO_3$ and $CoFe_2O_4$ in the composite x$PbTiO_3$-(1-x)$CoFe_2O_4$ films. The numbers in parentheses represent combined statistical uncertainties (1σ) from the x-ray profile fitting and squares refinements using four nonequivalent reflections……………………………………59

.

List of Figures

Figure 2.1 Schematic drawings of (a)–(b) a coherent two-phase structure on a substrate, (c)–(d) semicoherent structure with the interphase boundaries partially relaxed along the normal to the substrate, (e)–(f) semicoherent structure with a partially relaxed film/substrate interface. [21]………………………………………. 7

Figure 2.2 (a),(b) and (c) are phase field modeling predictions (left) and experimental TEM plan view images (right) for $2/3PbTiO_3$-$1/3CoFe_2O_4$ films; (d),(e) and (f) are phase field modeling predictions (left) and experimental TEM plan view images (right) for $1/3PbTiO_3$-$2/3CoFe_2O_4$ films……………………………………….......10

Figure 2.3 Schematic drawing of differently oriented cubic substrates indicating their distinct in-plane anisotropy…………………………………………………………..10

Figure 2.4 Schematics of perovskite-spinel nanostructures on (001) and (111) substrate. (a) Demonstration of different surface energy relationships for different oriented substrates based on Winterbottom constructions. Blue blocks represent spinel component and grey blocks are perovskite component. (b) Shapes of equilibrium crystalline nucleus of a perovskite and a spinel. (c) spinel phase forms nanopillars embedded in a perovskite matrix on (001) substrate (d) Nanopillars of perovskite phase embedded in a spinel matrix on a (111) substrate [22]………………………..…13

Figure 3.1 (a) PLD system employed in our study. (b). schematic drawing of the laser and chamber system……………………………………………………………17

Figure 3.2 Schematic illustration of substrate temperature impact on metallic film structures. The longitudinal axis is T_s/T_m [44]…………………………………………..18

Figure.3.3. Films deposited on $SrTiO_3(001)$ substrates from a $2/3PbTiO_3$-$1/3CoFe_2O_4$ target with 150mtorr oxygen pressure and $1.0J/cm^2$ laser fluence. Only growth temperatures are different. (a) 883K. (b) 903K. ……………………………………....22

Figure.3.4 Films deposited on $SrTiO_3(111)$ from a $2/3CoFe_2O_4$-$1/3PbTiO_3$ target with 100mtorr oxygen pressure and $1J/cm^2$ power density. Only growth temperature is different. (a) 883K. (b) 903K. (c) 923K..22

Figure.3.5. XRD spectrums for 2/3$PbTiO_3$-1/3$CoFe_2O_4$ films deposited on $SrTiO_3$(100) substrate at temperature of 883K, 0.83 J/cm^2 power density, 5Hz repetition rate. (a) Deposited under 134mtorr. (b) Deposited under 165mtorr..……....27

Figure 3.6 films deposited on $SrTiO_3$(111) substrate with a composition of 1/3$PbTiO_3$-2/3$CoFe_2O_4$ under temperature of 903K, 1.0J/cm^2 power density, 5Hz repetition rate. (a) (d) are XRD spectrum and SEM image from film deposited under 80mTorr oxygen pressure. (b) (e) are XRD spectrum and SEM image from film grown under 100mtorr oxygen pressure. (c) (f) are XRD spectrum and SEM image from film grown under 200mtorr oxygen pressure………………..………………...27

Fig 3.7.SEM images of 2/3$CoFe_2O_4$-1/3$PbTiO_3$ target surface after 40 minutes exposure to 1.0 J/cm^2 laser irradiation. (a) Target surface under low magnification. Upper right corner is an unexposed area on the target after deposition. (b) Target surface under higher magnification. Circled areas have cone structure and ripple structure is observed on the rest area (c) Schematic drawing of target after deposition. The grey area is the laser scanning area; the white area is the unexposed area. (d) Zoom in image of one of the circled areas in fig.3.7b shows cone structure. (e) Zoom in image of an area from fig.3.7b shows ripple structure. (f) Image of laser beam on the target……………………………………………..…………………….…32

Figure 3.8, plume image (a) at the very beginning of 80 minutes deposition, power density is 1.2 J/cm^2, (b) at the end of the same deposition process. (c) Schematic curve of deposition rate as function of time. The inset is experimental data from Foltyn [66]……………………………………...…………………………....33

Figure 3.9 Spectrum of EDAX scanning on cone crown area. The cross-line position is where the EDAX scanning performed…………………………………………..…34

Figure 3.10 Spectrum of EDAX scanning on well area. The cross line position is where we performed the EDAX scanning………………………………….…………..35

Figure 3.11 Spectrum of EDAX scanning on unexposed area on the target………...36

Figure 4.1 SEM topography of x$PbTiO_3$-(1-x)$CoFe_2O_4$ film morphology on $SrTiO_3$ of various orientations. White area denotes $PbTiO_3$ and black area denotes $CoFe_2O_4$....39

Figure 4.2 (a) Cross-sectional TEM image shows a $CoFe_2O_4$ inclusion embedded in $PbTiO_3$ matrix in x=2/3 film on (110) $SrTiO_3$ substrate. (b) Three different zones of a simplified single inclusion embedded in matrix……………………………………..41

Figure 4.3 (a) Cross-sectional TEM images of $CoFe_2O_4$ embedded in $PbTiO_3$ matrix of x=2/3 film on (001) $SrTiO_3$. Image on the right is the higher resolution TEM image on area around a single $CoFe_2O_4$ inclusion circled by dash line on the left side image. (b) Schematic illustration of wetting/non-wetting scenarios on (001) and (110) $SrTiO_3$ substrates……………………..…………………………………………………43

Figure 4.4 (a) Cross-sectional TEM image of x=1/3 film on (111) $SrTiO_3$. (b) Schematics of $PbTiO_3$ with side {111} interfaces. (c) Schematics of wetting/non-wetting of spinel ($CoFe_2O_4$) and perovskite ($PbTiO_3$) on (111) $SrTiO_3$ substrate......44

Figure 4.5 (a) Cross-sectional and plan-view TEM images for x=2/3 film of ~30nm thickness on (110) $SrTiO_3$. (b) Cross-sectional TEM image for x=2/3 film of ~100nm thickness on (110) $SrTiO_3$…………………………………………………………...45

Figure4.6 (a),(b),(c) Cross-sectional and plan-view TEM images of the $CoFe_2O_4$ rods in the x = 2/3 film grown on (001) $SrTiO_3$. (d),(e) Macro- and nanoscale schematics of single $CoFe_2O_4$ rod embedded in $PbTiO_3$ matrix……………………………..….47

Figure 4.7 (a) Crystallographic illustration of out-of-plane zigzagging {111} plane (A,B) with average (011) plane normal to the substrate. Those dash blue lines are guide to eye showing an example of zigzagging. (b) Crystallographic top view illustration. Solid blue and dash orange lines are projected {111} planes on (001) film surface…………………………………...……………………………………..…48

Figure 4.8 Schematics of dislocations at the $PbTiO_3$ and $CoFe_2O_4$ interface……....49

Figure 4.9 (a),(b),(c) Cross-sectional, plan-view TEM images of $CoFe_2O_4$ lamellas in x=2/3 film grown on (110) $SrTiO_3$. (d) Schematic of single $CoFe_2O_4$ lamellae embedded in $PbTiO_3$ matrix. (e) Crystallographic illustration of in-plane zigzag {111} planes (A, B_1, B_2) along <112> direction. (f). Crystallographic top view of {111} planes projected on (101) plane. Blue and orange line are different {111} planes….51

Figure 4.10 (a)Plan-view TEM image of $PbTiO_3$ platelets in x=2/3 film grown on (110) $SrTiO_3$. (b) SEM image of x=1/3 film on (110) $SrTiO_3$. $PbTiO_3$ appears as platelets embedded in $CoFe_2O_4$ matrix (c) Schematic of $PbTiO_3$ platelets embedded in $CoFe_2O_4$ matrix……………………………………………………………………52

Figure 4.11 (a),(b) Cross-sectional and plan-view images of the x = 1/3 films on the (111) $SrTiO_3$ showing the $PbTiO_3$ rods (bright) in the $CoFe_2O_4$ matrix (dark). c) Low-magnification high-resolution TEM image showing faceting of the $PbTiO_3$ nanorods. (d),(e) Schematics of micro- and nanoscale single $PbTiO_3$ pillar embedded in $CoFe_2O_4$ matrix on (111) $SrTiO_3$ substrate. (f) Crystallographic illustration of {111} planes on (111) surface. (g) Crystallographic top view illustration of {111} planes projected on $(1\bar{1}1)$ plane. The dash blue lines denote the intersection of projected {111} planes on film surface along <112> traces...…………………………………53

Figure 4.12 Nanostructure of x=1/3 film on (111) $SrTiO_3$ substrate. (a) SEM topography. (b) Cross-sectional TEM image showing $PbTiO_3$ top side facets marked by dash blue circle. (c) Schematics of $PbTiO_3$ top region side facets circled in (b) by dash blue line…………………………. ……………………………………..….54

Figure 5.1 X-Ray spectrum for $2/3CoFe_2O_4$-$1/3PbTiO_3$ film on $SrTiO_3(001)$ substrate. Full width at half maximum (FWHM) are 0.49°, 0.29° for 004_{CFO} and 004_{CFO} peaks respectively………………………………………………………………..…60

Figure.5.2 Rocking curves for 002_{PTO} and 004_{CFO} peaks in fig.5.1. (a) 002_{PTO} rocking curve with FWHM of 0.79° (b) 004_{CFO} rocking curve with FWHM of 0.73°……….61

Figure. 5.3 Out-of-plane ($a_\perp$) and in-plane ($a_{||}$) lattice parameters of $CoFe_2O_4$ (black squares and red dots) divided by 2, $PbTiO_3$,(green and blue triangles) and $SrTiO_3$ (purple and light blue triangles) in the $xPbTiO_3$-$(1-x)CoFe_2O_4$ films on $SrTiO_3(100)$ substrate measured as a function of temperature. Lattice parameters of bulk $PbTiO_3$ [70] are shown in (a) using asterisks. (a) x=2/3 and (b) x=1/3………………..............62

Figure 5.4 Plan-view (a) and cross-sectional (b) TEM images of the x=1/3 film. Twin domains in $PbTiO_3$ are observed as circled…………………………………………66

Figure 5.5 Low-resolution reciprocal space maps encompassing 200 $SrTiO_3$, 002/200 $PbTiO_3$, and 004 $CoFe_2O_4$ reflections for films with x=2/3 [(a) and (b)] and x=1/3 [(c) and (d)] acquired at 298K ((a) and (c)) and 823K ((b) and (d)). Appearance of a-domains in $PbTiO_3$ below a ferroelectric transition can be observed………………..67

Figure 5.6 Schematics of $PbTiO_3$ domains. Cubic is the phase above transition temperature. After cooled down, it can be transformed into three types of stressed tetragonal domains denoted by grey (c domain), white (a_1 domain) and yellow (a_2 domain) bars……………………………………….......……………………..….69

Figure 5.7 Schematic illustration of phase transformation of $PbTiO_3$ in self-assembled film on $SrTiO_3$ substrate. (1).constrained but stress-free state at high temperature (a),(b); (2).constrained state of pure c domain film at room temperature (c),(d); (3).constrained relaxed states of polydomain (a_1,a_2 and c domains) film at room temperature (e),(f)….……………………………………………………….……..69

Figure 6.1 Standard PFM setup for vertical and lateral piezoresponse acquisition….75

Figure 6.2 (1) Schematics of a structure consisting of two piezoelectric domains with opposite orientations separated by a non-piezoelectric stripe. (2) Schematics of expected PFM amplitude and phase images……………………………………....76

Figure 6.3 (1) Schematics of modified Sawyer-Tower circuit. (2) Schematic illustration of ferroelectric polarization hysteresis loop (P-E loop). (3) Experimental polarization hysteresis loops of $2/3PbTiO_3$-$1/3CoFe_2O_4$ thin film on (100) $SrTiO_3$ substrate [52]……………………………………….....……………………..77

Figure 6.4 Schematics of dc bias waveform. t1 is the writing period and t4 is the reading period. t3 is a waiting interval……………………………………………80

Figure 6.5 (1) Illustration of butterfly amplitude loop. (2) Illustration of phase loop. (3) Piezoresponse (piezoelectric) hysteresis loop generated based on amplitude and phase data in (1) and (2). (4) Schematics of transforming d_{zz} piezoresponse hysteresis loop to polarization hysteresis loop………………..……….……………………..81

Figure 6.6 Typical SS-PFM setup including two function generators, a summation amplifier (Σ) two lock-in amplifiers and a photolithography scanner head………...83

Figure 6.7 (1) Illustration of a pathway grid used in SS-PFM measurement. Data will be collected at each of the intersection. (2) Illustration of a piezoelectric hysteresis loop from one single point at the intersection……………………………………84

Figure 6.8 $1/3PbTiO_3$-$2/3CoFe_2O_4$ (110) oriented film (1) SEM Topography image. The dark-grey platelets with width of ~15nm are $PbTiO_3$ (PTO) and the rest is $CoFe_2O_4$ (CFO) matrix. (2) SS-PFM map of piezoresponse (3) schematics of the

$PbTiO_3$ platelets identified based on the SS-PFM image. (4) Conventional PFM amplitude image (5) Conventional PFM phase image coupled with (4)……….......87

Figure 6.9 Piezoelectric hysteresis loops and calculated piezoresponse. (1),(2),(4) are piezoelectric hysteresis loops at point 1,2 and 4. (3a) Amplitude curve at point 3. (3b) Phase curve at point 3. (3c) Piezoelectric hysteresis loop at point 3………………...87

Figure 6.10 (111) oriented $1/3PbTiO_3$-$2/3CoFe_2O_4$ thin film on $SrTiO_3(111)$ substrate. (1) SEM topography image. (2) Amplitude image from PFM measurement. (3) Phase image from PFM measurement. (4) SS-PFM map (5) One typical piezoelectric loop with relatively strong piezoreponse from SS-PFM measurement…..........................88

Figure 6.11. (100) oriented film of composition $1/3PbTiO_3$-$2/3CoFe_2O_4$. (1) SEM topography. (2) SS-PFM results including (a) amplitude curve, (b) phase curve and (c) generated piezoelectric hysteresis loop..……………………………………………..89

Figure 6.12 PFM lateral piezoresponse. (1) and (2) are amplitude and phase image respectively for (110) oriented $1/3PbTiO_3$-$2/3CoFe_2O_4$ film. (3) and (4) are amplitude and phase image respectively for (111) $1/3PbTiO_3$-$2/3CoFe_2O_4$ oriented film. Both (111) and (110) oriented film are measured under the same experimental conditions. (5) Schematics of intruded $PbTiO_3$ nanorods out of the $CoFe_2O_4$ matrix for the (111) oriented film…..…………………………………………………………………90

Figure 6.13(a) Tip coordinate system (x_1,x_2,z). (b) 2D projection from the top. r is the tip radius, a is the x coordinate of the tip center. 0 point of x axis is at the interface of $CoFe_2O_4/PbTiO_3$…………………………………………..……………………91

Figure 6.14 (1) Normalized calculated piezoresponse as a function of tip position and experimental results (points 1 to 4). (2) Illustration of tip position with respect to $PbTiO_3$ nanoplatelets………....…..………………………………………………..93

Chapter 1. Introduction

Multiferroic materials which exhibit coupled ferromagnetic and ferroelectric properties have attracted tremendous interests since magnetoelectric effect was discovered in Cr_2O_3 [1]. Magnetoelectricity (ME) is defined as the induction of magnetization by an electrical field while electromagnetism (EH) refers to the induction of an electrical field due to changing of magnetic field. Bulk laminate magnetoelectric composites that consist of piezoelectric and magnetostrictive layers exhibit ME/EH effect that are orders of magnitude larger than those exhibited by the best single-phase multiferroic materials [2,3,4,5,6,7,8]. However, composite layered multiferroics have great deficiencies in a thin film configuration because the ME/EH response is effectively suppressed by the strong substrate clamping. The clamping effect in thin film heterostructures can be minimized if the interfaces between the two constituent phases are perpendicular to the film surface. In the recent few years, the advances in thin film deposition technique enable growth of artificial structures that are inaccessible by traditional methods [9]. Vertically separated two-phase multiferroic nanostructure were successfully fabricated using pulsed laser deposition (PLD) for $BaTiO_3$-$CoFe_2O_4$ system in 2004 [10]. Other two-phase multiferroic systems (Fe_2O_3-$BiFeO_3$, $BiFeO_3$-$CoFe_2O_4$, $PbTiO_3$-$CoFe_2O_4$) were grown most recently using PLD [11,12,13,14]. Other than grown by PLD, multiferroic films have been prepared using sol-gel technique [15]. Composition spreads along in-plane direction were used to fabricate structure with tunable multiferroic properties in [16].

This study is a continuation of the research on design, fabrication and

ABSTRACT

Title of Document: FORMATION AND PIEZOELECTRICITY OF SELF-ASSEMBLED $PbTiO_3$-$CoFe_2O_4$ NANOSTRUCTURAL FILMS

Zhuopeng Tan, Doctor of Philosophy, 2008

Directed By: Professor Alexander L. Roytburd,
Dept. of Materials Science and Engineering

Dr. Igor Levin,
National Institute of Standards and Technology

Main tasks of our research include: (1) exploring optimum growth conditions for PLD deposition of self-assembled nanophase $PbTiO_3$-$CoFe_2O_4$ films with different compositions and orientations; (2) analyzing morphologies and nanostructures of the two-phase films to clarify relative effects of elastic energy and interface energy on the self-assembled film formation; (3) investigating stress state and relaxation of stresses arising as a result of a paraelectric-ferroelectric transformation in $PbTiO_3$; (4) exploring ferroelectric state in the confined $PbTiO_3$ nanophase in the films with {110} and {111} orientations.

Principal results of the research are: (1). Optimum PLD growth conditions to obtain high quality films with distinct separation of epitaxial $PbTiO_3$ and $CoFe_2O_4$ nanophases are found after systematic studies. (2). Nano-facets along {111} plane between $PbTiO_3$ and $CoFe_2O_4$ phases are found to be generic in addition to

orientation dependent macroscopic interfaces. We have concluded that accounting of interface and surface energies is important for description of nano-faceting of interfaces and the near substrate zone of the films while the two-phase morphologies are determined by the elastic interactions; (3). The investigation of the stress state of the {001} film arising due to paraelectric-ferroelectric transition of $PbTiO_3$ have discovered the polydomain nanostructure of the ferroelectric phase with ~50-60% *c*-domains. Piezoresponse of $PbTiO_3$ should be reduced dramatically by combined effects of dissolution of Fe in $PbTiO_3$, *a* domains and constraints. The relative large d_{zz} from previous research must contain large extrinsic contribution due to movement of nano-domain walls. (4). Switching spectroscopy piezoresponse force microscopy (SS-PFM) is used to characterize local piezo- ferroelectric property of confined ferroelectrics in {110} and {111} films with composition of $1/3PbTiO_3$-$2/3CoFe_2O_4$. It is proved that $PbTiO_3$ nano-inclusions exhibit ferroelectricity in both films. 180^o domain switching is observed under measurement condition (<10V) for the {110} films but not for the {111} film. Quantitatively, both films yield a piezoresponse of about 15% compared to bulk single crystal $PbTiO_3$. It is a reasonable value of intrinsic piezoeffect taking into account mechanical and electrical constraints (depolarizing field) as well as the effect of Fe dissolution and possible in-plane domains.

FORMATION AND PIEZOELECTRICITY OF SELF-ASSEMBLED $PbTiO_3$-$CoFe_2O_4$ NANOSTRUCTURAL FILMS

By

Zhuopeng Tan

Dissertation submitted to the Faculty of the Graduate School of the
University of Maryland, College Park, in partial fulfillment
of the requirements for the degree of
Doctor of Philosophy
2008

Advisory Committee:
Professor Alexander L. Roytburd, Chair
Dr. Igor Levin, Co-advisor
Professor Manfred Wuttig
Associate Professor Ichiro Takeuchi
Associate Professor Hugh Bruck

© Copyright by
Zhuopeng Tan
2008

Dedication

To my parents and my sister

for their unconditional love and never-ending support

Acknowledgements

I would like to thank my knowledgeable advisor, Alexander L. Roytburd, for his support, encouragement and guidance. Without his help, I would not be able to finish my my dissertation. I would also like to thank Dr. Igor Levin serving as my co-advisor for his great effort, very productive discussions and advices.

I would like to acknowledge the many individuals who contribute to this work either directly or indirectly including but not limited to:

National Institute of Standards and Technology (Gaithersburg, MD)

Dr. Peter Schenck, Dr. Kao-Shuo Chang, Dr. Leonid A. Bendersky, Dr. Albert V. Davydov, Dr. Alexander J. Shapiro, Dr. Julia Slutsker, Dr. Guang-Yao Liu, Dr. Jian-Hua Li, Ms. Sandra W. Claggett

Oak Ridge National Laboratory (Oak Ridge, TN)

Dr. Sergei V. Kalinin, Dr. Art Baddorf, Dr. Brian Rodriguez, Dr. Katyayani Seal, Dr. Stephen Jesse

.

Table of Contents

Dedication ii
Acknowledgements iii
Table of Contents iv
List of Tables vi
List of Figures vii
Chapter 1 Introduction 1
Chapter 2 Thermodynamic Aspects of Epitaxial Self-Assembled Nanostructures 5
2.1 Introduction 5
2.2 Elastic Energy vs. Surface Energy Anisotropy 7
  2.21. Elastic Energy Approach 7
  2.2.2 Surface Energy Anisotropy Approach 12
2.3 Conclusion 14

Chapter 3 Growth of Epitaxial Self-Assembled Nanostructures of xPbTiO$_3$-(1-x)CoFe$_2$O$_4$ Using Pulsed Laser Deposition 16

3.1. Introduction 16
3.2. Experiment Setup 17
3.3. Effects of Growth Parameters 18
  3.3.1. Substrate Temperature 18
  3.3.2. Laser Fluence, O2 Pressure and Target-Substrate Distance 24

3.4 Intrinsic and Extrinsic Shortcomings of PLD System 30
3.5 Conclusion 37

Chapter 4 Morphology and Nanostructure of PbTiO$_3$-CoFe$_2$O$_4$ Films 39

4.1 Introduction 39
4.2 Bottom Zone Morphology and Interfaces 42
4.3 Main Zone: Morphology and Interface Nanostructure 46
  4.3.1 Interface Nanostructure for (001) Oriented Films 46
  4.3.2 Interface Nanostructures for (110) Oriented Films 49
  4.3.3 Interface Nanostructures for (111) Oriented Films 52
4.4 Top Zone Structures 54
4.5 Discussion and Conclusion 55

Chapter 5 Accommodation of Transformation Strains in Self-Assembled CoFe$_2$O$_4$-PbTiO$_3$ Nanostructures 58

5.1 Introduction 58

5.2 Experiments……………………………………………………….………………..58
5.3 Effect of Constraint on T_c and Nanostructure of $PbTiO_3$ ……………..…..……64
5.4 Conclusion……………………………………………………...…………..72

Chapter 6 Piezoelectric Properties of Nano-$PbTiO_3$ Ferroelectrics Embedded in Ferromagnetic Film

……………………………………...……….…..…73
6.1 Introduction…………………………….…………….…..……………………73
6.2 Measurement techniques…………………….…………………….….……….74
    6.2.1 Conventional PFM Qualitative Measurement………...………...………………74
    6.2.2 Quantitative Hysteresis Loop Acquisition…………………………....………77
    6.2.3 Switching Spectroscopy piezoresponse force microscopy……...……..………...82
6.3 Experimental Results obtained by SS-PFM…………………...……………..……..85
    6.3.1 SS-PFM Results for (110) Oriented Thin Film……………..……..…………..86
    6.3.2 SS-PFM Results for (111) Oriented Thin Film……………...…..………..……..88
    6.3.3 SS-PFM Results for (001) Oriented Thin Film………….…………….……..89
    6.3.4 Lateral Piezoresponse…………………………….……..………………89
6.4 Discussion………...……………………………………….………………..90
6.5 Conclusion……………..…………….…………………………………………..95

Summary…………………………….…………………………..…………..97

Appendices…………………………...…………….…………………………101
Bibliography……………………………..………….……………………………..102

List of Tables

Table 3.1 Oxide film growth temperatures…………….………..…………………..19

Table 3.2 Growth parameters and qualities of 2/3$CoFe_2O_4$-1/3$PbTiO_3$ films.………21

Table 3.3 Result of EDAX scanning on the 2/3$CoFe_2O_4$+1/3$PbTiO_3$ target surface after deposition……………………………………………………………………..34

Table 3.4 List of vapor pressure for target chemical elements [64]…………………34

Table 3.5 Result of EDAX scanning on the well area on the 2/3$CoFe_2O_4$+1/3$PbTiO_3$ target surface after deposition. (Refer to figure 3.10 for scanning area and the scanning spectrum)…………………………………...…...…………………35

Table 5.1 Room temperature values of lattice parameters of $PbTiO_3$ and $CoFe_2O_4$ in the composite x$PbTiO_3$-(1-x)$CoFe_2O_4$ films. The numbers in parentheses represent combined statistical uncertainties (1σ) from the x-ray profile fitting and squares refinements using four nonequivalent reflections……………………………………59

.

List of Figures

Figure 2.1 Schematic drawings of (a)–(b) a coherent two-phase structure on a substrate, (c)–(d) semicoherent structure with the interphase boundaries partially relaxed along the normal to the substrate, (e)–(f) semicoherent structure with a partially relaxed film/substrate interface. [21]……………….……………………. 7

Figure 2.2 (a),(b) and (c) are phase field modeling predictions (left) and experimental TEM plan view images (right) for 2/3$PbTiO_3$-1/3$CoFe_2O_4$ films; (d),(e) and (f) are phase field modeling predictions (left) and experimental TEM plan view images (right) for 1/3$PbTiO_3$-2/3$CoFe_2O_4$ films.……………………………….……….....10

Figure 2.3 Schematic drawing of differently oriented cubic substrates indicating their distinct in-plane anisotropy……………..…………………………...…………10

Figure 2.4 Schematics of perovskite-spinel nanostructures on (001) and (111) substrate. (a) Demonstration of different surface energy relationships for different oriented substrates based on Winterbottom constructions. Blue blocks represent spinel component and grey blocks are perovskite component. (b) Shapes of equilibrium crystalline nucleus of a perovskite and a spinel. (c) spinel phase forms nanopillars embedded in a perovskite matrix on (001) substrate (d) Nanopillars of perovskite phase embedded in a spinel matrix on a (111) substrate [22]……………………..…13

Figure 3.1 (a) PLD system employed in our study. (b). schematic drawing of the laser and chamber system…………………………………………………………17

Figure 3.2 Schematic illustration of substrate temperature impact on metallic film structures. The longitudinal axis is T_s/T_m [44]……………………….………….…..18

Figure.3.3. Films deposited on $SrTiO_3$(001) substrates from a 2/3$PbTiO_3$-1/3$CoFe_2O_4$ target with 150mtorr oxygen pressure and 1.0J/cm^2 laser fluence. Only growth temperatures are different. (a) 883K. (b) 903K. ………………………….……....22

Figure.3.4 Films deposited on $SrTiO_3$(111) from a 2/3$CoFe_2O_4$-1/3$PbTiO_3$ target with 100mtorr oxygen pressure and 1J/cm^2 power density. Only growth temperature is different. (a) 883K. (b) 903K. (c) 923K..22

Figure.3.5. XRD spectrums for $2/3PbTiO_3$-$1/3CoFe_2O_4$ films deposited on $SrTiO_3$(100) substrate at temperature of 883K, 0.83 J/cm^2 power density, 5Hz repetition rate. (a) Deposited under 134mtorr. (b) Deposited under 165mtorr..….....27
Figure 3.6 films deposited on $SrTiO_3$(111) substrate with a composition of $1/3PbTiO_3$-$2/3CoFe_2O_4$ under temperature of 903K, 1.0J/cm^2 power density, 5Hz repetition rate. (a) (d) are XRD spectrum and SEM image from film deposited under 80mTorr oxygen pressure. (b) (e) are XRD spectrum and SEM image from film grown under 100mtorr oxygen pressure. (c) (f) are XRD spectrum and SEM image from film grown under 200mtorr oxygen pressure………………..………………...27
Fig 3.7.SEM images of $2/3CoFe_2O_4$-$1/3PbTiO_3$ target surface after 40 minutes exposure to 1.0 J/cm^2 laser irradiation. (a) Target surface under low magnification. Upper right corner is an unexposed area on the target after deposition. (b) Target surface under higher magnification. Circled areas have cone structure and ripple structure is observed on the rest area (c) Schematic drawing of target after deposition. The grey area is the laser scanning area; the white area is the unexposed area. (d) Zoom in image of one of the circled areas in fig.3.7b shows cone structure. (e) Zoom in image of an area from fig.3.7b shows ripple structure. (f) Image of laser beam on the target…………………………………………..……………………..…32
Figure 3.8, plume image (a) at the very beginning of 80 minutes deposition, power density is 1.2 J/cm^2, (b) at the end of the same deposition process. (c) Schematic curve of deposition rate as function of time. The inset is experimental data from Foltyn [66]……………………………………...……………………………....33
Figure 3.9 Spectrum of EDAX scanning on cone crown area. The cross-line position is where the EDAX scanning performed……………………………………….…34
Figure 3.10 Spectrum of EDAX scanning on well area. The cross line position is where we performed the EDAX scanning…………………………….…………..35
Figure 3.11 Spectrum of EDAX scanning on unexposed area on the target………...36

Figure 4.1 SEM topography of $xPbTiO_3$-$(1-x)CoFe_2O_4$ film morphology on $SrTiO_3$ of various orientations. White area denotes $PbTiO_3$ and black area denotes $CoFe_2O_4$....39

Figure 4.2 (a) Cross-sectional TEM image shows a $CoFe_2O_4$ inclusion embedded in $PbTiO_3$ matrix in x=2/3 film on (110) $SrTiO_3$ substrate. (b) Three different zones of a simplified single inclusion embedded in matrix……………………………………..41

Figure 4.3 (a) Cross-sectional TEM images of $CoFe_2O_4$ embedded in $PbTiO_3$ matrix of x=2/3 film on (001) $SrTiO_3$. Image on the right is the higher resolution TEM image on area around a single $CoFe_2O_4$ inclusion circled by dash line on the left side image. (b) Schematic illustration of wetting/non-wetting scenarios on (001) and (110) $SrTiO_3$ substrates………………………..……………………………………………………43

Figure 4.4 (a) Cross-sectional TEM image of x=1/3 film on (111) $SrTiO_3$. (b) Schematics of $PbTiO_3$ with side {111} interfaces. (c) Schematics of wetting/non-wetting of spinel ($CoFe_2O_4$) and perovskite ($PbTiO_3$) on (111) $SrTiO_3$ substrate......44

Figure 4.5 (a) Cross-sectional and plan-view TEM images for x=2/3 film of ~30nm thickness on (110) $SrTiO_3$. (b) Cross-sectional TEM image for x=2/3 film of ~100nm thickness on (110) $SrTiO_3$………………………………………………………...45

Figure4.6 (a),(b),(c) Cross-sectional and plan-view TEM images of the $CoFe_2O_4$ rods in the x = 2/3 film grown on (001) $SrTiO_3$. (d),(e) Macro- and nanoscale schematics of single $CoFe_2O_4$ rod embedded in $PbTiO_3$ matrix……………………………...….47

Figure 4.7 (a) Crystallographic illustration of out-of-plane zigzagging {111} plane (A,B) with average (011) plane normal to the substrate. Those dash blue lines are guide to eye showing an example of zigzagging. (b) Crystallographic top view illustration. Solid blue and dash orange lines are projected {111} planes on (001) film surface…………………………………...……………………………………...…48

Figure 4.8 Schematics of dislocations at the $PbTiO_3$ and $CoFe_2O_4$ interface……....49

Figure 4.9 (a),(b),(c) Cross-sectional, plan-view TEM images of $CoFe_2O_4$ lamellas in x=2/3 film grown on (110) $SrTiO_3$. (d) Schematic of single $CoFe_2O_4$ lamellae embedded in $PbTiO_3$ matrix. (e) Crystallographic illustration of in-plane zigzag {111} planes (A, B_1, B_2) along <112> direction. (f). Crystallographic top view of {111} planes projected on (101) plane. Blue and orange line are different {111} planes….51

Figure 4.10 (a)Plan-view TEM image of $PbTiO_3$ platelets in x=2/3 film grown on (110) $SrTiO_3$. (b) SEM image of x=1/3 film on (110) $SrTiO_3$. $PbTiO_3$ appears as platelets embedded in $CoFe_2O_4$ matrix (c) Schematic of $PbTiO_3$ platelets embedded in $CoFe_2O_4$ matrix……………………………………………………………………52

Figure 4.11 (a),(b) Cross-sectional and plan-view images of the x = 1/3 films on the (111) $SrTiO_3$ showing the $PbTiO_3$ rods (bright) in the $CoFe_2O_4$ matrix (dark). c) Low-magnification high-resolution TEM image showing faceting of the $PbTiO_3$ nanorods. (d),(e) Schematics of micro- and nanoscale single $PbTiO_3$ pillar embedded in $CoFe_2O_4$ matrix on (111) $SrTiO_3$ substrate. (f) Crystallographic illustration of {111} planes on (111) surface. (g) Crystallographic top view illustration of {111} planes projected on $(1\bar{1}1)$ plane. The dash blue lines denote the intersection of projected {111} planes on film surface along <112> traces..…………………………………53

Figure 4.12 Nanostructure of x=1/3 film on (111) $SrTiO_3$ substrate. (a) SEM topography. (b) Cross-sectional TEM image showing $PbTiO_3$ top side facets marked by dash blue circle. (c) Schematics of $PbTiO_3$ top region side facets circled in (b) by dash blue line…………………………. ……………………………………...….54

Figure 5.1 X-Ray spectrum for $2/3CoFe_2O_4$-$1/3PbTiO_3$ film on $SrTiO_3(001)$ substrate. Full width at half maximum (FWHM) are 0.49°, 0.29° for 004_{CFO} and 004_{CFO} peaks respectively…………………………………………………………………..…60

Figure.5.2 Rocking curves for 002_{PTO} and 004_{CFO} peaks in fig.5.1. (a) 002_{PTO} rocking curve with FWHM of 0.79° (b) 004_{CFO} rocking curve with FWHM of 0.73°……….61

Figure. 5.3 Out-of-plane ($a_\perp$) and in-plane ($a_\parallel$) lattice parameters of $CoFe_2O_4$ (black squares and red dots) divided by 2, $PbTiO_3$,(green and blue triangles) and $SrTiO_3$ (purple and light blue triangles) in the $xPbTiO_3$-$(1-x)CoFe_2O_4$ films on $SrTiO_3(100)$ substrate measured as a function of temperature. Lattice parameters of bulk $PbTiO_3$ [70] are shown in (a) using asterisks. (a) x=2/3 and (b) x=1/3…………….............62

Figure 5.4 Plan-view (a) and cross-sectional (b) TEM images of the x=1/3 film. Twin domains in $PbTiO_3$ are observed as circled…………………………………………66

Figure 5.5 Low-resolution reciprocal space maps encompassing 200 $SrTiO_3$, 002/200 $PbTiO_3$, and 004 $CoFe_2O_4$ reflections for films with x=2/3 [(a) and (b)] and x=1/3 [(c) and (d)] acquired at 298K ((a) and (c)) and 823K ((b) and (d)). Appearance of a-domains in $PbTiO_3$ below a ferroelectric transition can be observed………………..67

Figure 5.6 Schematics of $PbTiO_3$ domains. Cubic is the phase above transition temperature. After cooled down, it can be transformed into three types of stressed tetragonal domains denoted by grey (c domain), white (a_1 domain) and yellow (a_2 domain) bars…………………………………………........………………………..….69

Figure 5.7 Schematic illustration of phase transformation of $PbTiO_3$ in self-assembled film on $SrTiO_3$ substrate. (1).constrained but stress-free state at high temperature (a),(b); (2).constrained state of pure c domain film at room temperature (c),(d); (3).constrained relaxed states of polydomain (a_1,a_2 and c domains) film at room temperature (e),(f)….……………………………………………………….……..69

Figure 6.1 Standard PFM setup for vertical and lateral piezoresponse acquisition….75

Figure 6.2 (1) Schematics of a structure consisting of two piezoelectric domains with opposite orientations separated by a non-piezoelectric stripe. (2) Schematics of expected PFM amplitude and phase images……………………………………....76

Figure 6.3 (1) Schematics of modified Sawyer-Tower circuit. (2) Schematic illustration of ferroelectric polarization hysteresis loop (P-E loop). (3) Experimental polarization hysteresis loops of $2/3PbTiO_3$-$1/3CoFe_2O_4$ thin film on (100) $SrTiO_3$ substrate [52]…………………………………………....……………………..77

Figure 6.4 Schematics of dc bias waveform. t1 is the writing period and t4 is the reading period. t3 is a waiting interval……………………………………………80

Figure 6.5 (1) Illustration of butterfly amplitude loop. (2) Illustration of phase loop. (3) Piezoresponse (piezoelectric) hysteresis loop generated based on amplitude and phase data in (1) and (2). (4) Schematics of transforming d_{zz} piezoresponse hysteresis loop to polarization hysteresis loop………………..……….……………………..81

Figure 6.6 Typical SS-PFM setup including two function generators, a summation amplifier (Σ) two lock-in amplifiers and a photolithography scanner head………...83

Figure 6.7 (1) Illustration of a pathway grid used in SS-PFM measurement. Data will be collected at each of the intersection. (2) Illustration of a piezoelectric hysteresis loop from one single point at the intersection……………………………………84

Figure 6.8 $1/3PbTiO_3$-$2/3CoFe_2O_4$ (110) oriented film (1) SEM Topography image. The dark-grey platelets with width of ~15nm are $PbTiO_3$ (PTO) and the rest is $CoFe_2O_4$ (CFO) matrix. (2) SS-PFM map of piezoresponse (3) schematics of the

$PbTiO_3$ platelets identified based on the SS-PFM image. (4) Conventional PFM amplitude image (5) Conventional PFM phase image coupled with (4)…………........87

Figure 6.9 Piezoelectric hysteresis loops and calculated piezoresponse. (1),(2),(4) are piezoelectric hysteresis loops at point 1,2 and 4. (3a) Amplitude curve at point 3. (3b) Phase curve at point 3. (3c) Piezoelectric hysteresis loop at point 3………………...87

Figure 6.10 (111) oriented $1/3PbTiO_3$-$2/3CoFe_2O_4$ thin film on $SrTiO_3$(111) substrate. (1) SEM topography image. (2) Amplitude image from PFM measurement. (3) Phase image from PFM measurement. (4) SS-PFM map (5) One typical piezoelectric loop with relatively strong piezoreponse from SS-PFM measurement…..........................88

Figure 6.11. (100) oriented film of composition $1/3PbTiO_3$-$2/3CoFe_2O_4$. (1) SEM topography. (2) SS-PFM results including (a) amplitude curve, (b) phase curve and (c) generated piezoelectric hysteresis loop..……………………………………………..89

Figure 6.12 PFM lateral piezoresponse. (1) and (2) are amplitude and phase image respectively for (110) oriented $1/3PbTiO_3$-$2/3CoFe_2O_4$ film. (3) and (4) are amplitude and phase image respectively for (111) $1/3PbTiO_3$-$2/3CoFe_2O_4$ oriented film. Both (111) and (110) oriented film are measured under the same experimental conditions. (5) Schematics of intruded $PbTiO_3$ nanorods out of the $CoFe_2O_4$ matrix for the (111) oriented film…...……………………………………………………………90

Figure 6.13(a) Tip coordinate system (x_1,x_2,z). (b) 2D projection from the top. r is the tip radius, a is the x coordinate of the tip center. 0 point of x axis is at the interface of $CoFe_2O_4$/$PbTiO_3$……………………………………………..……………………91

Figure 6.14 (1) Normalized calculated piezoresponse as a function of tip position and experimental results (points 1 to 4). (2) Illustration of tip position with respect to $PbTiO_3$ nanoplatelets…………...…..……………………………………………..93

characterization of structures and properties of self-assembled nanostructures in $PbTiO_3$-$CoFe_2O_4$ films. $PbTiO_3$-$CoFe_2O_4$ system has been chosen due to a large spontaneous polarization with a large spontaneous strain of $PbTiO_3$ [17] and a significant magnetostriction of $CoFe_2O_4$ [18].

Growth of self-assembled two-phase films is attractive because it potentially capable to produce controlled patterned nanostructures which satisfy the demands of high density device units. Compared to self-assembling, the conventional lithography fabrication method of patterns is very expensive and complicated when the unit size scales down to nanometers [19]. Self-assembling growth technique using PLD is an experimentally simple one-step process. However, due to complexity of the PLD process, there is no theoretical model which realistically describes growth mechanism for a two-phase film. Therefore, a systematic experimental study should be conducted to find optimum conditions for a growth of self-assembled nanostructure with distinct separation of the phases using PLD.

Despite the lack of theoretical model for mechanism of nanostructure formation, the thermodynamic approach appears to be effective to describe and predict the morphology of a final structure. The thermodynamic theory taking into account the long range elastic interaction between nanophases and the phase field modeling based on this theory could successfully predict the dependence of $xPbTiO_3$-$(1-x)CoFe_2O_4$ film morphologies on the substrate orientation[20,21]. However, this modeling which neglects the anisotropy of interfacial energy can not explain some observed features of the self-assembled nanostructure, particularly nano-faceting of interfaces. Other study attempt to explain some peculiarities of the film structure taking into account only anisotropy of surface energies of the constituent phases and the substrate [22,12]. However, these studies can not explain entire spectrum of observed morphologies. Therefore, more detail studies of film structures are necessary to clarify effects of elastic energies and interface energies on the morphologies and interface nanostructures. It is important for the improvement of theoretical modeling for design multiferroic films with controlled structures.

Internal stress in 3D epitaxial $PbTiO_3$-$CoFe_2O_4$ films is important both for formation of its nanostructure as well as for the magnetoelectric properties. While due to the special nanostructure of interfaces included interface dislocations, the internal stress is effectively relaxed at relatively high temperatures between growth temperature and Curie temperature of $PbTiO_{3.}$ However, the large stresses should arise again at paraelectric-ferroelectric transformation of $PbTiO_3$. Taking into account the large spontaneous strain of $PbTiO_3$, its accommodation in the constrained phases is critical for mechanical and physical properties of the films. Therefore, the investigation of this stress state and its relaxation should be a necessary element of this study.

As individual piezoelectric and/or ferroelectric nanopillars have the potential applications towards high density electronic devices, strong interests are stirred examining local properties of individual ferroelectric/piezoelectric pillars/rods [23,24, 25]. In {110}/{111} oriented films of $1/3PbTiO_3$-$2/3CoFe_2O_4$ composition, $PbTiO_3$ forms nanoplatelets/nanorods embedded in $CoFe_2O_4$ matrix. It makes it possible to obtain piezo-/ferroelectric properties of confined single $PbTiO_3$ inclusions in self-assembled films. A newly developed technique, switching spectroscopy piezoresponse force microscopy (SS-PFM), should be used for local ferroelectric property characterization [26].

Thus, the main tasks of this research are:

1. Exploring optimum growth conditions for PLD deposition of self-assembled nanophase $PbTiO_3$-$CoFe_2O_4$ films with different compositions and orientations.
2. Analyzing the morphology and nanostructure of the two-phase films to clarify relative effects of elastic energy and interface energy on the film formation of self-assembled film nanostructures.
3. Investigating a stress state and the relaxation of stresses arising as a result of a paraelectric-ferroelectric transformation in $PbTiO_3$.
4. Exploring ferroelectric state in the confined $PbTiO_3$ nanophases in the films with {110} and {111} orientations.

Chapter 2 Thermodynamic Aspects of Epitaxial Self-Assembled Nanostructures

2.1 Introduction

Comprehensive theoretical modeling of self-assembled nanostructure should take into account details of mechanism and kinetics of several processes leading to the formation of a two-phase epitaxial film. There are many works devoted to modeling of spinodal decomposition in epitaxial films where the kinetics of structure formation is determined by surface and volume diffusion [27,28]. There are also theoretical works considering phase separation during co-deposition of different phases [29]. However, there are no theoretical modeling which enables to describe adequately the formation of a multiphase film during PLD deposition due to complexity of this process including laser-target interaction, materials transport to the substrate, its interaction with substrate, nucleation and growth.

At the same time, if the deposition is not very fast, final two-phase structure may be close to equilibrium and can be described using thermodynamic approach. This approach has been successfully applied to analysis of transversely modulated structures [10] and allows one to design film with controlled morphology by changing substrate orientations [20,21]. The fundamental principle of this approach is following: in nano-scale multiphase systems the trend to equilibrium results in establishing epitaxial relations between phases and consequently partial transformation of interface energy into energy of epitaxial stress. Thus, the individual nanophases act as elastic domains, which self-assemble to minimize the long-range elastic fields in the film. The resulting phase architectures are similar to polydomain heterostructures arising at phase transitions in single-phase epitaxial films [30,31]. Then, the final equilibrium two-phase structures corresponding to the minimum of free energy including elastic energy and energy of interfaces can be modeled as a result of a virtual phase transformation that mimics evolution of an initially uniform state to a final equilibrium two-phase structure. The phase field modeling of this transformation serves as a computational tool for design of equilibrium two-phase nanostructure. The validity of this approach has been demonstrated through successful prediction of effect of film orientation on its morphology [20]. It has been shown that variation of substrate orientation is an effective way of controlling the phase-architectures in self-assembled composite nanostructures.

The different thermodynamic approach on self-assembled nanostructure formation has been proposed assuming that the formation of the nanostructure was attributed entirely to the distinct surface energy anisotropies of the composite phases [22,12]. It has presented explanation for some structure characteristics of perovskite-spinel films.

The existent thermodynamic approaches to interpret nanostructure formation in two-phase perovskite-spinel film emphasize two different thermodynamic contributions: elastic energy and surface/interface energy. They are rather complementary than competitive and should be combined to develop comprehensive thermodynamic theory of this phenomenon and to improve modeling for design of multiferroic films with controlled structure.

2.2 Elastic Energy vs. Surface Energy Anisotropy

2.2.1 Elastic Energy Approach

The phase field modeling of $PbTiO_3$-$CoFe_2O_4$ nanostructural films is based on the following physical arguments illustrated in fig.2.1.

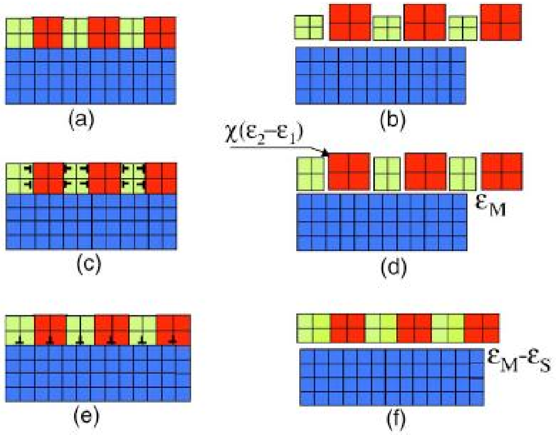
(a)
(b)
$\chi(\varepsilon_2-\varepsilon_1)$
ε_M
(c)
(d)
ε_M-ε_S
(e)
(f)

Figure 2.1 Schematic drawings of (a)–(b) a coherent two-phase structure on a substrate, (c)–(d) semicoherent structure with the interphase boundaries partially relaxed along the normal to the substrate, (e)–(f) semicoherent structure with a partially relaxed film/substrate interface. [21].

Elastic interactions arise in multiphase nanostructures due to epitaxy, resulting in formation of coherent or semicoherent interphase boundaries and film/substrate interfaces. The stress state in the coherent multiphase film/substrate system (fig.2.1a) can be described using the self-strains of the component phases, as determined from the differences in the lattice parameters of the undistorted phases and a substrate, the latter being used as a reference state. A coherent two-phase nanostructure consisting of $PbTiO_3$ (a_1=3.96 Å) and $CoFe_2O_4$ (a_2=8.38 Å/2=4.19 Å) on a $SrTiO_3$ (a_s=3.95 Å) substrate can be described by a distorted cubic lattice (Figs. 1a and 1b). Since both phases are cubic at the growth temperature, the self-strains correspond to a pure dilatation, $\varepsilon_1=(a_1-a_s)/a_s$=0.0025 and $\varepsilon_2=(a_2-a_s)/a_s$=0.061. Equilibrium nanostructures may consist of coherent phases (fig.2.1a), however, the nanostructures grown experimentally are semicoherent and feature misfit dislocations (figs. 2.1c–2.1f). Therefore, the strain relaxation along the interfaces (both interphase boundaries and film/substrate interface) needs to be considered. The relaxation along the interphase boundaries occurs during deposition preferentially in a direction normal to the substrate (Figs. 2.1c and 2.1d), since the relaxation parallel to the substrate is limited by the small lateral scale of the component phases (typically <50 nm). In such partially-relaxed systems, the difference between the self-strains of the phases in a film acquires a tetragonal symmetry:

$$\Delta\varepsilon = \varepsilon_0 \begin{pmatrix} 1 & 0 & 0 \\ 0 & 1 & 0 \\ 0 & 0 & \chi \end{pmatrix}$$

where $\varepsilon_0 = \varepsilon - \varepsilon_2$, $\chi<1$ is a relaxation parameter. The final film thicknesses (>200 nm) typically exceed the critical values needed for formation of misfit dislocations so that the film/substrate interface becomes semicoherent (Figs. 2.1e and 2.1f) which results in the relaxation of the average stresses in the film. This relaxation can be described by an effective change in the substrate lattice parameter, $a_s^{eff} = a_s(1-\rho_m b)$, where ρ_m

is the misfit dislocation density and b is the dislocation Burgers vector [18,19].

Near equilibrium, the arrangement of phases, their morphologies, and the relaxation parameters of the interfaces (χ, a_s^{eff}) can be found by minimizing the sum of the elastic and interfacial energies for a given phase fraction.

A 3D phase-field model described the nanostructures as a continuous field of the order parameter $\eta(r)$. The equilibrium arrangements of phases were determined by minimizing the free energy, F, which included both interfacial (isotropic) and elastic (anisotropic) energy terms, with respect to η. The equation $\partial F/\partial\eta(r)=0$ was solved using a relaxation procedure that considered a virtual phase transformation from the unstable initial phase ($\eta=0$) to a two-phase state corresponding to the two minima of the specific free energy $f(\eta)= f_0(\eta-\eta^2)^2$, where $\eta_{01}=-1$ and $\eta_{02}=1$ and f_0 is the specific free energy at $\eta=0$. The time evolution of the phase field of the order parameters, as described by the time dependent Landau–Ginzburg equation, was solved using the microelasticity approach [20,32 33].

In fig.2.2, results of the phase field modeling are presented together with experimental data for {001}, {110} and {111} substrate orientations. The calculated morphologies correctly predict the effects of substrate orientations on the nanostructure architectures. In particular, even such nontrivial morphological changes as lamellar to labyrinth [Figs. 2.2b(left) and 2.2c(left)], with substrate orientation varying from (110) to (111), and labyrinth to rod [Fig. 2.2e(left),2.2f(left)], with the $PbTiO_3$ fraction decreasing from 2/3 to 1/3, were reproduced. This strikingly consistent agreement between the experimental and calculated data, obtained despite the assumption of thermodynamic equilibrium, provides strong support for the dominant role of elastic interphase interactions in defining the morphologies of the nanostructures. In particular, the modeling showed that the morphologies [figs.2.2a-2.2f (left)], are determined by the in-plane elastic anisotropy [fig.2.3] and as dictated by the substrate orientation.

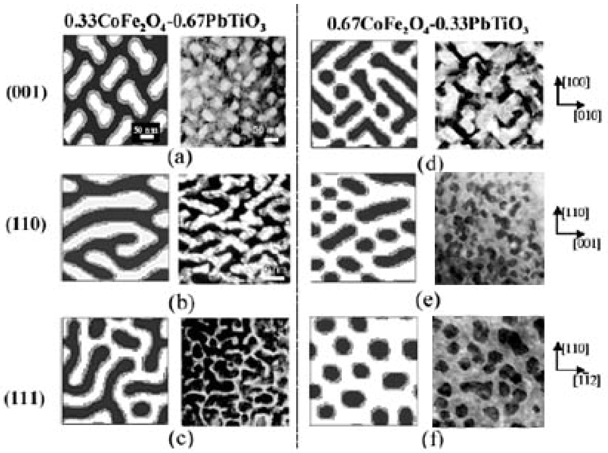
$0.33CoFe_2O_4$-$0.67PbTiO_3$
$0.67CoFe_2O_4$-$0.33PbTiO_3$
(001)
(110)
(111)
50 nm
50 nm
[100]
[010]
[110]
[001]
[110]
$[\bar{1}12]$
(a)
(b)
(c)
(d)
(e)
(f)

Fig.2.2 (a),(b) and (c) are phase field modeling predictions (left) and experimental TEM plan view images (right) for 2/3$PbTiO_3$-1/3$CoFe_2O_4$ films; (d),(e) and (f) are phase field modeling predictions (left) and experimental TEM plan view images (right) for 1/3$PbTiO_3$-2/3$CoFe_2O_4$ films.

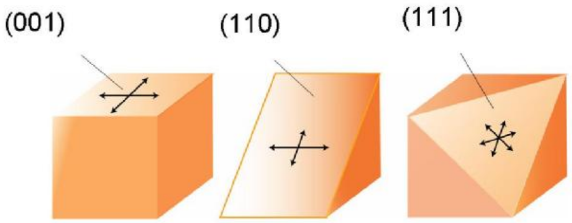

Figure 2.3 Schematic drawing of differently oriented cubic substrates indicating their distinct in-plane anisotropy

According to the simulations, the principal morphological differences for differently oriented substrates originate from the positive elastic anisotropy of spinel–perovskite films, which modifies the symmetry of the stress state as a function of orientation. For relatively large film thicknesses (>200 nm), the strain along the film–substrate interface was relaxed completely so that the substrate had no effect on the phase morphologies other than providing the epitaxial orientation of the phases.

The significant discrepancy between this phase-field modeling and the experiment is a rod–matrix reversal with varying phase fractions in the films grown on (001) substrates, which was predicted by simulations but could not be observed experimentally (Figs. 2.2a and 2.2d). This discrepancy can be attributed, at least in part, to the inadequacy of the assumption of identical elastic moduli for the spinel and perovskite phases because, at equilibrium, a more rigid phase forms inclusions, whereas a softer phase becomes a matrix [34]. In particular, for the (100) substrate orientation, $CoFe_2O_4$ exhibits a substantially larger in-plane stiffness than $PbTiO_3$ [34, 35,36] and, therefore, is expected to form isolated pillars, regardless of phase fractions. However, this discrepancy can be addressed to peculiarity of structure formation at first stage of film growth which will be discussed later.

The phase field modeling neglecting anisotropy of interface energy can not reveal also nano-faceting structure. It should be mention that there are two special plane orientations of epitaxial films. One of them corresponds to the best atomic fitting between film and substrate. It usually lies along close-packed crystallographic plane and has minimum interface energy. The other epitaxial interface corresponds to minimum elastic energy and may lies along even irrational plane. The orientation of this plane is determined by minimum misfit between lattices. These interfaces have complex nanostructure and nonuniform stress distribution near the interface. The distorted near interface layer determines the effective thickness of this macroscopic interface [37].

2.2.2 Surface Energy Anisotropy Approach

The thermodynamic approach based on surface energy anisotropy [22] suggested that the different structures on different orientation substrates were merely a result of the different surface energies between phases and the substrate. To the nucleation and growth on a substrate, the equilibrium shape of a crystalline nucleus can be determined by the substrate surface energy, γ_1, interface energy, γ_{12} and surface energy of the crystalline phase, γ_2, based on the Winterbottom construction [22,38]. Applied the Winterbottom construction to perovskite-spinel nanostructure (fig.2.4) results in different morphologies as the surface energy relationships varies.

For perovskite-spinel system, the surface energy approach proposed nanopillars of spinel phase distributed in perovskite matrix on (001) substrate (fig.2.4c) and nanopillars of perovskite phase distributed in spinel matrix on (111) substrate (fig.2.4d). Both cases did not depend on the percentage of the phases. For (110) oriented substrate, both spinel and perovskite phases could have comparable wetting conditions with similar nucleation barriers, thus lead to a maze pattern in which neither phase formed matrix or pillars [12,22].

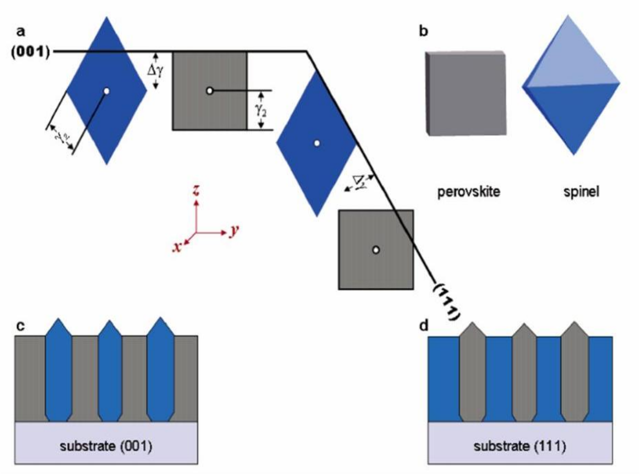

Figure.2.4 Schematics of perovskite-spinel nanostructures on (001) and (111) substrate. (a) Demonstration of different surface energy relationships for different oriented substrates based on Winterbottom constructions. Blue blocks represent spinel component and grey blocks are perovskite component. (b) Shapes of equilibrium crystalline nucleus of a perovskite and a spinel. (c) spinel phase forms nanopillars embedded in a perovskite matrix on (001) substrate (d) Nanopillars of perovskite phase embedded in a spinel matrix on a (111) substrate [22].

The (001) oriented xPbTiO$_3$-(1-x)CoFe$_2$O$_4$ film morphologies (figs.2.2a and 2.2c) were predicted well by the surface energy approach. According to the Winterbottom construction, regardless of the phase fractions, the spinel phase forms pillars embedded in perovskite matrix (fig.2.4c). However, for CoFe$_2$O$_4$-BiFeO$_3$ nanostructures grown on a buffer CoFe$_2$O$_4$ layer on (001) MgO substrate, a lack of wetting for the CoFe$_2$O$_4$ phase on CoFe$_2$O$_4$ buffer layer was observed [22]. The lack of wetting for CoFe$_2$O$_4$ was contradicted to the surface energy approach as the energy of the homoepitaxial CoFe$_2$O$_4$/CoFe$_2$O$_4$ interface should be close to zero as opposed to the energy of the BiFeO$_3$/CoFe$_2$O$_4$ interface. The surface energy approach also fails to explain the morphological difference as observed for the xPbTiO$_3$-(1-x)CoFe$_2$O$_4$ nanostructures on (110) SrTiO$_3$ substrate [figs.2.2b and 2.2e]. Clearly, CoFe$_2$O$_4$ does not "wet" the (110) substrate. From fig.2.2e, the non-wetting CoFe$_2$O$_4$ forms a continuous matrix and PbTiO$_3$ grows as isolated pillars while it wets the (110) substrate.

Nevertheless, distinct interfacial configurations that produce an impression of the wetting/non-wetting behavior for the spinel and perovskite phases in the nanostructures grown on differently oriented substrates could influence the resulting phase architectures. However, proper analyses of these configurations necessitate consideration of all interfacial energies involved as well as the epitaxial strain energy.

2.3 Conclusion

In spite of the lack of theoretical model of mechanism of nanostructure formation, the thermodynamic approach appears to be effective to describe and predict the morphology of final structure. The thermodynamic theory taking into account the long range elastic interaction between nanophases and the phase field modeling based on this theory could successfully predict the dependence of xPbTiO$_3$-(1-x)CoFe$_2$O$_4$ film morphologies on substrate orientation. However, this modeling neglecting anisotropy of interface energy can not explain some experimental observed features of film nanostructure, particularly nano-faceting of interfaces. On the other side, there is a successful attempt to explain some peculiarities of the film structure taking into account only anisotropy of surface energies of constituent phases and substrate [12,22]. Therefore, more detail studies of film structure is necessary to clarify effects of elastic energy and interface energy on morphology and interface nanostructures. It is important for the improvement of theoretical modeling for design multiferroic films with controlled structures. The existent thermodynamic approaches to interpret nanostructure formation in two-phase perovskite-spinel film emphasize two different thermodynamic contributions: elastic energy and surface/interface energy. They are rather complementary than competitive and should be combined to develop comprehensive thermodynamic theory of this phenomenon and to improve modeling for design of multiferroic films with controlled structure.

Chapter 3 Growth of Epitaxial Self-Assembled Nanostructures of xPbTiO$_3$-(1-x)CoFe$_2$O$_4$ Using Pulsed Laser Deposition

3.1. Introduction

Pulsed laser deposition (PLD) is a very powerful technique for making thin films. It has drawn intense interests in the past 30 years [39,40]. Theoretically, PLD can be used to deposit films of any material due to high output power of the laser beam (can be larger than 10^8 W/cm^2). Material processing using laser beams is always based on reactions taking place in the surface layer of the target material due to the interaction between the electromagnetic waves and the atoms and electrons. Typically, these reactions involve extensive heating and evaporation of the surface leading to consequent chemical or physical reactions in the surface, thus altering the structure of the material in some desired way, perhaps by initiating a chemical reaction between the target material and surrounding gas or liquid phase, or simply by removing and ablating the target material away.

Though the theories of dynamics of laser-target interactions were studied before the PLD was employed in experiments [41,42,43] and many researches have been done discussing the effects of growth parameters, it is hard to give a complete and self-consistent model for PLD process because of its complexity. In addition, the studies have been done so far are mostly limited to single phase growth, condition for PLD deposition of two-phase film from a mixed compound target is left unknown. Thereby, it is worthwhile to experimentally study optimum conditions for PLD growth of two-phase self-assembled nanostructures from a $PbTiO_3$/$CoFe_2O_4$ mixed target.

3.2. Experiment Setup

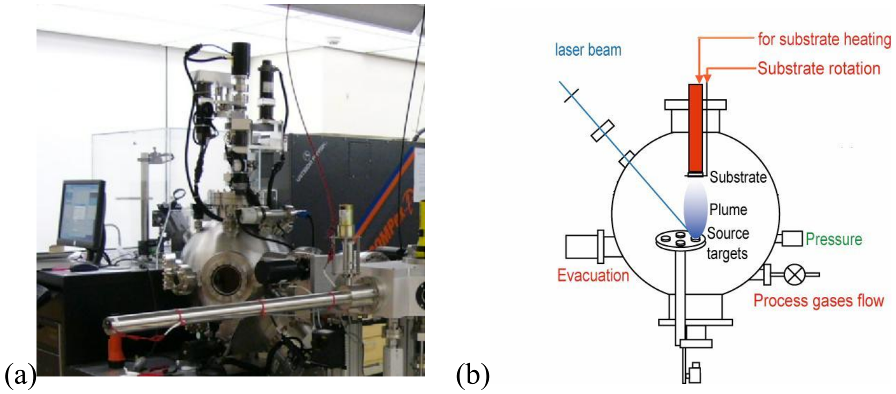
(a)
(b)
laser beam
for substrate heating
Substrate rotation
Substrate
Plume
Source targets
Pressure
Evacuation
Process gases flow

Figure 3.1 (a) PLD system employed in our study. (b). schematic drawing of the laser and chamber system.

$CoFe_2O_4$-$PbTiO_3$ self-assembled films are fabricated from $xPbTiO_3$–$(1\text{-}x)CoFe_2O_4$ (x=1/3,2/3) mixed targets using a KrF excimer laser system with a wavelength of 248nm, pulse duration of 20ns, adjustable repetition rate from 1Hz to 20Hz and controllable system output laser energy from 160mj to 400mj. Figure 3.1a is a picture of the employed Neocera PLD system. Fig.3.1b schematically illustrates the geometrical arrangements of laser beam, target and substrates inside the vacuum chamber.

Single crystal $SrTiO_3$ is used as substrate because of small lattice mismatch and similar crystal structure with $PbTiO_3$. Before loaded into the chamber, substrates are cleaned by orderly soaking them in chloroform, acetone and isopropanol under ultrasonic agitation. Substrate is heated by thermal radiator after the PLD chamber has been vacuumed to below 10^{-5} Torr. Substrate temperature can be raised up to 800^0C, which is the limit of our thermal radiator. Oxygen is introduced into the chamber after the substrate temperature has been stabilized to minimize the effects of outgas from the chamber.

3.3. Effects of Growth Parameters

3.3.1. Substrate Temperature

Based on experimental data from other researchers, Grovenor and Hentzell [44] found that for metallic film growth, when the substrate temperature (T_s) is less than $0.3T_m$ (T_m is the melting point of the target material), it usually has a structure consisting of textured and fibrous grains and the macroscopic texture may contains many individual small grains as illustrated in figure 3.2. When $0.3T_m<T_s<0.5T_m$, a uniform columnar grain structure is usually observed with an aspect ratio less than 1. When $T_s>0.5T_m$, the film structure changes to a uniform film with grains having an aspect ratio larger than 1 [44].

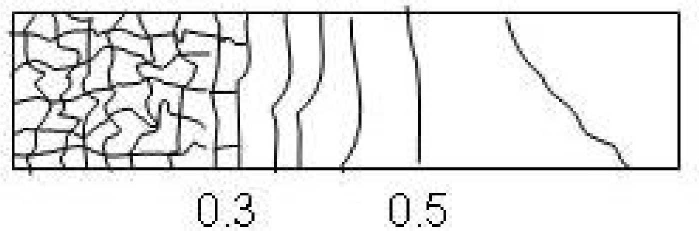

Figure 3.2 Schematic illustration of substrate temperature impact on metallic film structures. The longitudinal axis is T_s/T_m [44].

Table 3.1 is a list of temperatures used for epitaxial oxide film growth. It is found that the growth temperature is about $0.5T_m$, which is similar to what Grovenor [44] observed for metallic uniform film growth temperatures.Usually, the ideal grow temperature has a range rather than a particular temperature, but it is found that the temperature range is centered at $0.5T_m$.

Table 3.1 Oxide film growth temperatures

Materials	Sub	Ts/Tm
$CoFe_2O_4$	MgO	873-1073k/1843k[50,51]
$LiNbO_3$	Al_2O_3	773k/1528k [45]
$SrTiO_3$	$SrTiO_3$	1023k/2353k [46]
$BaTiO_3$	MgO	1053k/1923k [47]

For our film growth, because Pb is easy to lose at elevated temperatures, it is hard to keep the stoichiometric Pb/Ti ratio for temperatures around 721K [$T_m(PbTiO_3)$=1443K]. Above 823K, PbO tends to decompose during the film formation; as a result, the ratio of Pb/Ti decreases rapidly as TiO_2 is much more stable than PbO[48]. However, high growth temperature is desired for better crystallinity and self-assembly since the film pattern formation heavily relies on the diffusion during the growth. Essentially, it is a self-contradicting phenomenon to grow epitaxial self-assembled nanostructures with Pb involved. In order to compensate Pb loss during growth at temperatures higher than 823K, extra 10-15% mole fraction of PbO was added to our PLD targets.

In addition to the Pb loss problem, two-phase deposition itself has its own problem on growth temperature compared to single-phase growth. During single phase growth, there is usually a growth temperature range which does not cause distinct difference on film quality. For example, for pure single crystal $PbTiO_3$ film prepared by PLD, growth temperature can be varied from 653K to 823K [48,49] without destroying film quality; for pure single crystal $CoFe_2O_4$ film growth by PLD, it was found that the film quality was kept almost the same from 873K to 1073K leaving all other conditions unaltered [50,51].From the others' experiences on individual single crystal $PbTiO_3$ film and $CoFe_2O_4$ film growth, there is no temperature which suits both $PbTiO_3$ and $CoFe_2O_4$ simultaneously. However, as the extra amount of PbO can compensate Pb loss at high temperature, it is possible to find a temperature which suits both phases. According to the empirical $0.5T_m$ rule, T_s should be around 921K [52]. We chose 903K as a starting test temperature after taking into account the volatilization of Pb under high temperatures.

Films of composition $1/3PbTiO_3$-$1/3CoFe_2O_4$ grown under various temperatures ranging from 863K to 923K with 20 degrees step size are listed in table 3.2 (for growth conditions used for film of composition $2/3PbTiO_3$-$1/3CoFe_2O_4$, please refer to appendix 1). Fig.3.3a and 3.3b are SEM images from films with composition $2/3PbTiO_3$-$1/3CoFe_2O_4$ grown at 883K and 903K respectively. Growth conditions other than temperature were kept same. Film quality (fig.3.3a and fig3.3b) is distinctly different though there is only 20 degrees difference in growth temperatures.

Table 3.2 Growth parameters and qualities of 2/3$CoFe_2O_4$-1/3$PbTiO_3$ films

Substrate	Temp (K)	Distance (cm)	Laser fluence (J/cm^2)	Repetition rate(Hz)	O_2 (mTorr)	Pulses	Film quality
STO(100)	903	6.5	1.1	10	100	72000	No film
STO(100)	863	6.5	1.1	10	100	48000	No film
STO(110)	863	6.5	1.1	20	100	48000	No film
STO(111)	903	6.5	1.1	20	100	48000	No film
STO(111)	903	6.5	1.1	20	65	48000	Bad
STO(111)	883	4.5	0.7	5	100	12000	Bad
STO(111)	903	4.5	0.8	5	100	20000	Bad
STO(100)	903	4.8	0.8	3	160	24000	Bad
STO(111)	903	4.8	1.0	5	80	24000	Bad
STO(111)	888	4.8	1.1	5	100	24000	Fair
STO(111)	903	4.6	1.1	10	100	24000	Fair
STO(111)	923	4.5	1.1	10	100	24000	Bad
STO(111)	903	4.5	1.1	5	100	24000	Fair
STO(111)	903	4.6	1	5	84	48000	Bad
STO(110)	903	3.8	0.9	5	100	24000	Good
STO(110)	903	3.7	1	5	100	24000	Good
STO(111)	903	3.7	1	5	100	24000	Good
STO(110)	903	3.7	1	5	100	24000	Good
STO(111)	883	3.7	1	5	100	24000	Fair
STO(111)	923	3.7	1	5	100	24000	Fair
STO(111)	903	3.7	1	5	100	12000	Fair
STO(111)	903	3.7	0.9	5	100	900	Good
STO(111)	903	3.7	1	5	100	48000	Fair
STO(111)	903	3.7	1.4	5	200	12000	Fair

No film: no film on substrate is observed.

Bad: Well organized self-assembled nanostructures is not observed (refer to fig.3.4a for films with structures fall in this category).

Fair: Self-assembled nanostructure is observed together with defective features. For example, film shown in fig.3.4c. It has a self-assembled nanostructure, but the coarse matrix surface degrades film quality.

Good: Clear self-assembled nanostructure with no distinct deficiencies (refer to fig.3.4b for films with structures fall in this category).

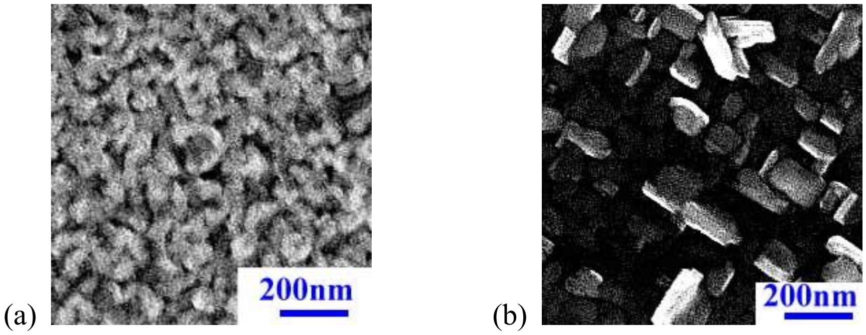

Fig.3.3. Films deposited on $SrTiO_3$(001) substrates from a $2/3PbTiO_3$-$1/3CoFe_2O_4$ target with 150mtorr oxygen pressure and 1.0J/cm^2 laser fluence. Only growth temperatures are different. (a) 883K. (b) 903K.

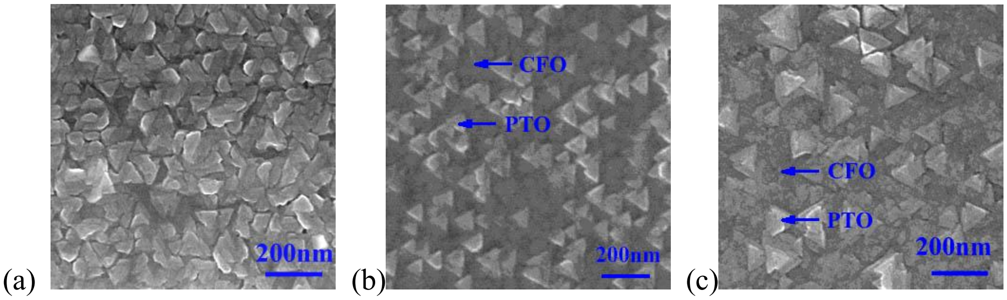

Fig.3.4 Films deposited on $SrTiO_3$(111) from a $2/3CoFe_2O_4$-$1/3PbTiO_3$ target with 100mtorr oxygen pressure and 1J/cm^2 power density. Only growth temperature is different. (a) 883K. (b) 903K. (c) 923K

In fig.3.3a, very dense intertwined features are observed, while in fig 3.3b, there are clear features of two-phase separation. Fig.3.4a to 3.4c are SEM topography images for films with the other composition ($2/3CoFe_2O_4$-$1/3PbTiO_3$). Film shown in fig 3.4a was grown at 883K, very dense $PbTiO_3$ triangles are observed. As the growth temperature is increased by 20 degrees to 903K, the density of $PbTiO_3$ triangles is decreased as demonstrated in fig 3.4b. Fig 3.4c shows clear isolated $PbTiO_3$ triangles from film grown at temperatures of 923K. Fig.3.4c demonstrates a $PbTiO_3$ pattern with the best self-organization among all three samples (fig.3.4a to 3.4c); however, the $CoFe_2O_4$ matrix surface becomes rough under this growth condition. Despite the different fraction of phases in films shown in fig.3.3 and fig.3.4, same trend is observed: higher temperature helps in terms of self-organization. Quality of all films is very sensitive to variation of temperature. The optional growth temperature for our self-assembled structure is near the lower limit of $CoFe_2O_4$ range and higher limit of $PbTiO_3$ range. That explains why the quality of the two-phase film is so much more sensitive than single phase growth to the temperature variations.

If the growth temperature range of each individual phase has a wide overlap, such as $BaTiO_3$-$CoFe_2O_4$ system, then the growth temperature for two-phase self-assembled structures can be expected to have a wide range. As it was reported for $BaTiO_3$-$CoFe_2O_4$ system, the growth temperature can be varied from 1123K to 1223K without destroying self assembling features. However, the wide overlap does not mean that the film structures will be the same for films grown within this temperature range. Rather, the growth temperature within the overlap range still has clear effects on film structures. As observed, the size of isolated nanopillars and spacing between pillars changes along with the temperature though self-assembled structures are preserved. The size of pillars and spacing between pillars are controlled by kinetics factors. As it was suggested that self-assembled decomposition is controlled kinetically by surface diffusion according to equation [53]:

$$\frac{\partial c}{\partial t} = \widetilde{D}_s \nabla^2 c + \frac{v}{\delta}(c_o - c) \tag{3.1}$$

where c is film composition and $\widetilde{D}_s$ is surface interdiffusivity of the two phases. It is clear that the surface diffusivity has dramatic effects on the nanostructure. Because of the intrinsic difference on surface diffusivity for the two components, the structure is expected to be sensitive to the temperature change as the temperature influence on surface diffusivity of each component is different. The size and spacing dependence on temperature is unambiguously different from one-phase growth [54].

Based on results from films grown at various growth temperatures, 903K is determined to be the most suitable PLD growth temperature for $CoFe_2O_4$-$PbTiO_3$ film.

3.3.2. Laser Fluence, O_2 Pressure and Target-Substrate Distance

Laser fluence, oxygen pressure and target-substrate distance are connected to each other. Target-substrate distance is determined by the plasma plume size and the plume size changes along with change of laser fluence or oxygen pressure. After laser fluence or oxygen pressure has been adjusted, the target-substrate distance needs to be adjusted as well to accommodate the change of plume size.

When a laser beam hits the target, if the laser fluence is higher than the threshold value, a Knudsen layer on the target surface will be generated due to high collision volume within nanoseconds. A luminous plume expansion will occur after the generation of Knudsen layer. The threshold energy density depends on material properties, such as mass density, heat capacity and reflectivity R to excimer laser irradiation. The actual energy on the target which causes the evaporation equals to the absorbed incident energy minus the losses by plasma absorption E_p and the conduction losses E_c:

$$(1-R)(E-E_p)-E_c=\Delta X_t[\rho C_p \Delta T+\Delta H] \tag{3.2}$$

where E is the incident laser energy, ρ is the mass density, ΔT is the change of target temperature, ΔH is the volume latent heat, ΔX_t is the thickness of the target material evaporated per pulse, C_p is the heat capacity of target material. For most of the oxides, the energy threshold falls within a range from 0.1J/cm^2 to 0.5J/cm^2. For PNZT, the threshold is 0.5J/cm^2 for incident laser beam with a 308nm wavelength, however, for high quality film growth, a higher power density is required [40,55,57,59,60]. Usually, a power density about 1.0J/cm^2 or higher is desirable for stoichiometric growth because it helps overcome the target surface composition segregation during deposition. The increase of the surface area after formation of target surface structures lowers the power density. Higher power density at the initial stage can ensure the power density is enough for epitaxial growth during the whole growth process. However, too much power will bring more particulates to the film surface, which seriously jeopardizes film qualities. The power density for our experiments is around 1J/cm^2 in order to satisfy the needs for material transport process and at the same time keep the density of particulates on film surface within an acceptable level.

If it is in vacuum, the plume generated by the laser will expand without changing its angular distribution and the intensity will reduce as it propagates. If ambient gas exists, in general, the ambient gas will confine the plume and slow down the propagation process, thus a stronger fluorescence and sharper boundary can be observed at the same time [56,57]. For our experiments, since it is an oxide target and in order to avoid oxygen deficit and help maintain stoichiometric Pb/Ti ratio, all the depositions are run under oxygen environment instead of in vacuum. All the species generated by the laser in the plume are confined with a fluorescence edge and interacted with the oxygen before they reach the substrate. Since Pb is unreactive to oxygen, higher oxygen pressure helps keep the Pb/Ti ratio better in the film. However, the deposition rate will decease after the oxygen pressure is raised as a result of interaction between species and the oxygen molecules during plume expansion which will bring changes to film structures. If the deposition rate is too low, it can even suppress the self-assembling features.

For single phase growth, there is a range of oxygen pressure which will not cause distinct changes to film qualities. $PD^n=Const$ is an empirical rule for the relationship between oxygen pressure and the target-substrate distance. P is oxygen pressure and D represents the target-substrate distance. n is a power to the distance, which depends on the particular system. Kim et al. [58] took n=2 and Castro-rodriguez et. al took n=3 [59,60]. This relationship was drawn based on an optimal growth rate for the best quality film from single phase growth. For our experiments, films are grown from two-phase mixed targets and each of the two phases has quite different optimum growth conditions individually. Several oxygen pressures and target-substrate distance combinations are tested for both compositions as listed in table 3.1 and appendix.1. Each time, the target-substrate distance was adjusted to accommodate the plume size change after oxygen pressure was changed.

Figure 3.5a and 3.5b are XRD spectrums for films with a composition of

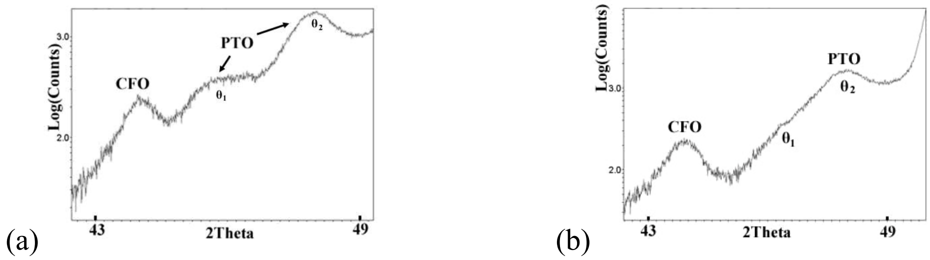

Fig.3.5. XRD spectrums for 2/3PbTiO$_3$-1/3CoFe$_2$O$_4$ films deposited on SrTiO$_3$(100) substrate at temperature of 883K, 0.83 J/cm^2 power density, 5Hz repetition rate. (a) Deposited under 134mtorr. (b) Deposited under 165mtorr.

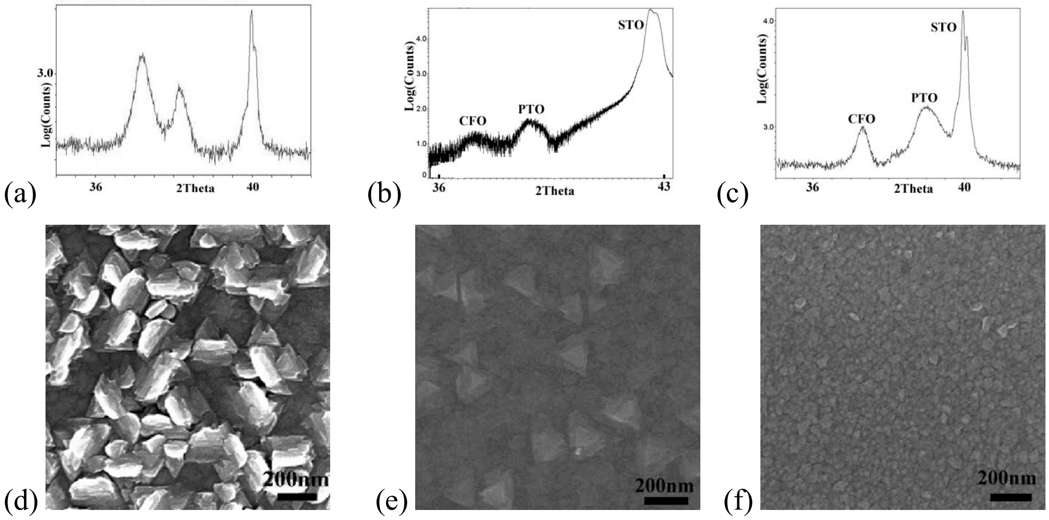

Figure 3.6 films deposited on SrTiO$_3$(111) substrate with a composition of 1/3PbTiO$_3$-2/3CoFe$_2$O$_4$ under temperature of 903K, 1.0J/cm^2 power density, 5Hz repetition rate. (a) (d) are XRD spectrum and SEM image from film deposited under 80mTorr oxygen pressure. (b) (e) are XRD spectrum and SEM image from film grown under 100mtorr oxygen pressure. (c) (f) are XRD spectrum and SEM image from film grown under 200mtorr oxygen pressure.

1/3$CoFe_2O_4$-2/3$PbTiO_3$ on $SrTiO_3$(001) substrates. One was grown under 134mTorr oxygen pressure (fig 3.5a), the other one was grown under 165mTorr oxygen pressure (fig.3.5b). Other growth parameters were kept the same for these two films. Two $PbTiO_3$ peaks are observed in fig 3.5a and the peak at higher 2θ angle is strengthened as the oxygen pressure is raised from 134mTorr to 165mTorr. The two $PbTiO_3$ peaks in fig 3.5a are PTO(002) and (200) respectively. Changing oxygen pressure results in volume fraction changes between these two types of domains. It can be seen from the XRD spectrum, 165mTorr oxygen pressure promotes growth of $PbTiO_3$(200) which is undesired because it will degrade the polarization response in normal direction. Reduction of perovskite phase fraction was also observed in PLZST film after oxygen pressure was raised to over 125mTorr [61]. Stabilization of $PbTiO_3$(200) under high oxygen pressure is possibly because high valence lead oxides (Pb_3O_4 and PbO_2) are stable forms under high oxygen pressure and results in a distortion of the crystal structure [62].

The oxygen effect on structures is observed as well for films of the other composition (*x*=1/3) (fig.3.6)., $PbTiO_3$(111) peaks are observed for *x*=1/3 films grown on $SrTiO_3$(111) substrates (fig 3.6a,3.6b and 3.6c) under three different oxygen pressures. The relative ratio of $PbTiO_3$(111) diffraction intensity against $CoFe_2O_4$(222) diffraction intensity increases as oxygen pressure is increased from 80mTorr (fig.3.6a) to 100mTorr (fig.3.6b) and then further increased to 200mTorr (fig.3.6c). At the same time, film structures (fig.3.6d, 3.6e, 3.6f) are observed to change along with changes of oxygen pressure. Fig.3.6d shows dense $PbTiO_3$ triangles with equal side length of about 230nm for film grown under 80mTorr (fig.3.6d). After oxygen pressure was raised to 100mTorr, density of $PbTiO_3$ triangles is decreased and the side length of the $PbTiO_3$ triangles (~200nm) is slightly decreased as well (fig.3.6e). Film surface becomes rough and no self-assembled structures are observed after oxygen pressure was further increased to 200mTorr (fig.3.6f). It was also reported that crystal structures were deteriorated and surface became coarse due to excessive oxygen pressure [63,61].

From what we have observed, the deposition of two-phase self-assembling films has a much more stringent requirement on oxygen pressure than one component growth and the $PD^n=Const$ law is not valid anymore. Considering quality of self-assembled structure and crystallinity, oxygen pressure of 100mTorr gives the best result out of films (listed in table3.1 and appendix.1) grown under various oxygen pressures and is used for all further growths for $CoFe_2O_4$-$PbTiO_3$ films.

It is desirable to have a wide adjustable range for target-substrate distance. However, the adjustable distance depends on other growth parameters as well as the design of the PLD system. For the commercial Neocera PLD system employed in our experiment, the designed adjustable target-substrate distance is from ~6cm to ~10cm. The lower limit of the distance is shortened to ~3.7cm after a home-made substrate holder is added to the system. The self-assembled nanostructure of best quality is found to form at a target-substrate distance of ~3.7cm. As 3.7cm is the lower end limit of the adjustable range, distance shorter than 3.7cm is not able to explore.

3.4 Intrinsic and Extrinsic Shortcomings of PLD System

Target modification during deposition is a drawback associated with PLD growth. Target surface keeps being modified during growth and the plume shape changes as a result, thereby brings effects to film qualities. Nowadays, the only solution is to take out the target after deposition and reshape the surface on sandpapers. When the target is under irradiation, nothing can be done to the surface though the surface changes constantly along with the laser shots.

Figure 3.7a, 3.7b and 3.7d are SEM images from the same target but different locations after irradiated by 12000 laser pulses with power density of 1.0 J/cm^2. Fig.3.7a shows the target surface remains intact at the center as schematically demonstrated in fig.3.7c. Ripple surface structure is observed at adjacent areas to the intact center as a result of weak power densities. Figure 3.7b is a surface structure image from a place around $r=r_o/2$, where r_o is the radius of the target. Both cone and ripple surface structures are observed at this area. Areas having cone structure are circled in fig.3.7b and a higher magnification image of cone structure is demonstrated in fig.3.8d. Fig.3.8e is a zoom in image from a place in fig.3.8b showing the ripple surface structure. Usually, cone surface structure indicates an energy density higher than 1J/cm^2, which is desirable for epitaxial oxide film growth [40]. As the target is rastering and rotating during deposition as illustrated in fig 3.7c by the double side arrow and the arc arrow respectively, the area close to the target center area is expected to expose to the edge of the beam. As the laser beam has inhomogeneous power distribution with long tales (about 1mm on one side) of weak power density (fig 3.7f), it is understandable to have a ripple area of about 1mm width (fig.3.7a). Even within the center of the rastering target surface, occupation of areas with ripple structure is more than 1/3 as shown in fig 3.7b and 3.7e. As can be seen from fig.3.7e, those ripples are connected to each other and winding through the surface. As a counterpart of cone structure, ripple structure indicates a relatively low power density with a range roughly from 0.1 J/cm^2 to $0.9J/cm^2$ [40]. Based on the SEM images, slightly less than half of the area exposed to laser irradiation has ripple structure because of not enough power density. As a result of inhomogeneous power distribution within the beam, for incident laser irradiation with $1J/cm^2$ power density in average, only a small area within the center of the laser beam has a power density higher than $1J/cm^2$ while the surrounding area has a power density lower than $1J/cm^2$. Thus generates energetic species with a broad range of momentum from the very beginning. Due to the complexity of plume interaction with the oxygen environment, the effects of the broad range of specie momentum to the film quality are hard to predict. A predictable effect from the inhomogeneous power distribution is a slower growth rate on average. Though raise the power of incident beam can escalate the power density at the beam edge area, higher average power density is not desirable because the power density at beam center area will be too high and leads to dense particulates on the film surface.

With the formation of cone or ripple structures on the surface, the surface area increases and the power density decreases as a result. The decrease of the power density leads to a weaker plume because of the decrease of the density of species within the plume (fig.3.8, slightly out of focus for both images).

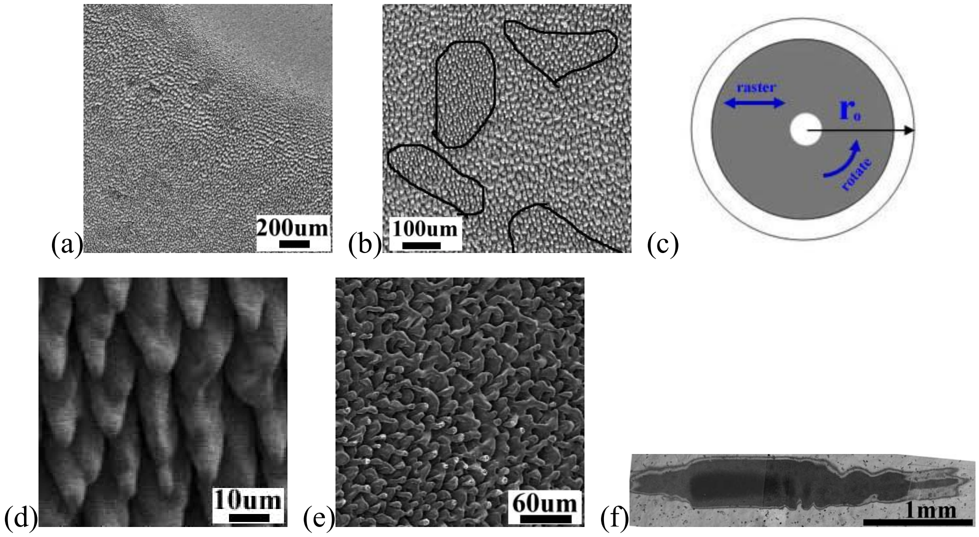

Fig 3.7.SEM images of $2/3CoFe_2O_4$-$1/3PbTiO_3$ target surface after 40 minutes exposure to 1.0 J/cm^2 laser irradiation. (a) Target surface under low magnification. Upper right corner is an unexposed area on the target after deposition. (b) Target surface under higher magnification. Circled areas have cone structure and ripple structure is observed on the rest area (c) Schematic drawing of target after deposition. The grey area is the laser scanning area; the white area is the unexposed area. (d) Zoom in image of one of the circled areas in fig.3.7b shows cone structure. (e) Zoom in image of an area from fig.3.7b shows ripple structure. (f) Image of laser beam on the target.

Compared to plume in fig.3.8b, it is clear that we have higher density of species within the plume in fig.3.8a and the plume in fig 3.8b skewed to the left with respect to the target normal direction and towards the laser beam incident direction. The

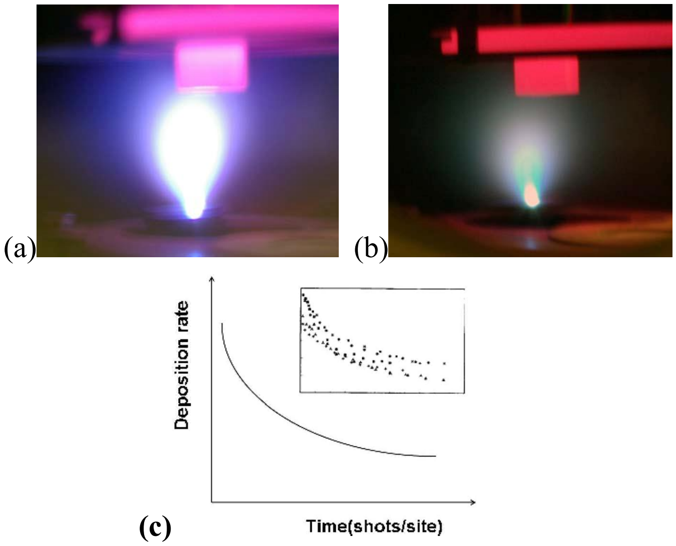

Figure 3.8, plume image (a) at the very beginning of 80 minutes deposition, power density is 1.2 J/cm^2, (b) at the end of the same deposition process. (c) Schematic curve of deposition rate as function of time. The inset is experimental data from Foltyn [66].

reduction of specie density is due to composition segregation on target surface and the increase of the target surface area. For our $CoFe_2O_4$-$PbTiO_3$ target, after deposition, Pb is not able to detect on the cone crown area (figure 3.9 cross line position) using EDAX. Based on the data in table 3.3, Co and Fe on the target surface have an atomic ratio of 1/2, which is the stoichiometric ratio of the original target. However, Pb disappears from the surface and atomic percentage of Ti is much higher than its percentage in the original target. In the original target, the Co/Ti atomic ratio is 2/1. On the target surface after deposition, Co/Ti only has an atomic ratio of less than ¼. Figure 3.11 is an EDAX spectrum from an area unexposed to the laser irradiation. Target composition segregation on the cone crown area after deposition is manifested if we compared results shown in fig 3.9 to results shown in figure 3.11.

Table 3.3 Result of EDAX scanning on the $2/3CoFe_2O_4+1/3PbTiO_3$ target surface after deposition. (Refer to figure 3.9 for scanning area and the scanning spectrum).

Elements	Wt %	At %
Ti	41.5	29.6
O	23.2	49.3
Fe	23.0	14.0
Co	12.3	7.1

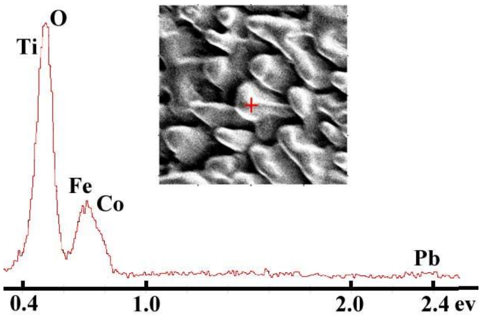

Figure 3.9 Spectrum of EDAX scanning on cone crown area. The cross-line position is where the EDAX scanning performed.

Table 3.4 List of vapor pressure for target chemical elements [64]

Vapor pressure of the chemical elements						
Pressure, atm	10^{-10}	10^{-8}	10^{-6}	10^{-4}	10^{-2}	1
elements	Temperature, C					
Cobalt Co	995	1161	1379	1686	2152	2928
Iron Fe	948	1109	1321	1617	2075	2862
Lead Pb	404	478	616	817	1140	1750
Titanium Ti	1124	1310	1554	1900	2421	3289

When we analyze the well area marked by the red-cross line in figure 3.10, Pb peak is clearly observed in the EDAX spectrum. Compared to figure 3.11, there is still composition segregation at the well area; however, the segregation here is not as severe as the cone crown area.

Table 3.5 Result of EDAX scanning on the well area on the $2/3CoFe_2O_4+1/3PbTiO_3$ target surface after deposition. (Refer to figure 3.10 for scanning area and the scanning spectrum).

Elements	Wt %	At %
Ti	58.4	68.8
Fe	18.8	19.0
Co	8.9	8.4
Pb	13.9	3.8

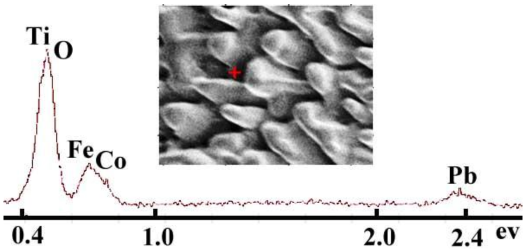

Figure 3.10 Spectrum of EDAX scanning on well area. The cross line position is where we performed the EDAX scanning

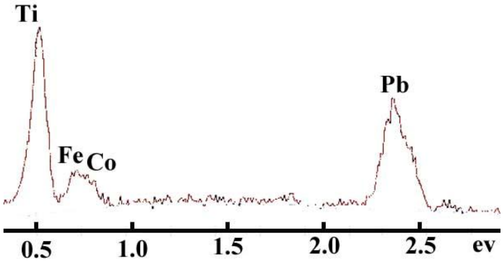

Figure 3.11 Spectrum of EDAX scanning on unexposed area on the target

Compare the vapor pressures listed in table 3.4 for all the elements in the target, Ti has the smallest vapor pressure, vapor pressures for Co and Fe are close and Pb has the highest vapor pressure. The smallest Ti vapor pressure and highest Pb vapor pressure support the EDAX findings very well. It is because of the different vapor pressure that causes a Ti-rich and Pb deficit thin layer on top of the cone and the composition gradually changes from the top to the well. This layer forms an obstacle for deposition and certainly affects the growth rate and film stoichiometry.

Usually, cones with a diameter of tens of microns are formed as surrounding material is removed by successive laser pulses, and as a result of this erosional formation process, they grow in length as laser exposure increases, and they point in the direction of the incident beam [65,66]. During the deposition, the plume shape changes as the surface composition segregation continues as can be seen in fig.3.9. The decrease of plume specie density as a function of the deposition time results in a time dependent decrease of deposition rate (fig.3.8c).

There are several approaches to relieve or avoid the surface composition segregation effect based on how it develops. Increase the power density is one of the possible solutions. Higher power density can increase the penetration depth within the target and remove more material including the top composition segregated surface. The drawback of high power density is particulates generated by high energy laser beam. Smaller spot size helps delay the formation of surface structure by reducing the number of shots per site and thus help maintain the plume status during deposition. However, smaller spot size generates smaller plume and the target-substrate distance has to be shorter to adopt the change. Improve the homogeneity of laser beam is another method as it helps generate plume with homogeneous distributions of species, thus provides wider range for power density adjustment. A better homogeneous beam status also helps delay the decay of growth rate which affects the structure anisotropy in normal direction.

3.5 Conclusion

Our PLD studies allow us to make some suggestions on optimum growth conditions for two-phase self-assembled films.

1. Optimum temperature range for growth of high quality epitaxial two-phase self-assembled structure is narrow. The optimum temperature for $CoFe_2O_4$-$PbTiO_3$ films independently on compositions and orientations is found to be 903K. Even 20 degrees changes of temperature result in severe structure degradations. This optimum temperature is located in the temperature range where the range of temperatures for optimum growth of epitaxial films for $CoFe_2O_4$ and $PbTiO_3$ are overlapped. For $CoFe_2O_4$, optimum temperatures locate in the interval of 200 degrees around $0.5T_m$ (T_m=1843k) and for $PbTiO_3$, optimum temperatures locate in the interval of ~80 degrees around $0.5T_m$ (T_m=1420k). 10%-15% of extra PbO was added to the compound target in order to achieve overlapping of optimum temperature ranges, though in a very narrow interval.

2. Laser fluence is an important factor as well because it affects plume size and the specie densities within plume, thus leads to different growth rates which results in different sizes and/or shapes of inclusions. Our experiments show that only when the growth rate is above a certain value, the three-dimensional self-assembled $PbTiO_3$-$CoFe_2O_4$ nanostructure can be formed. Laser fluence around 1J/cm^2 is necessary for our $PbTiO_3$-$CoFe_2O_4$ film growth to overcome irradiation resulted composition segregation on target surface and results in somewhat desired growth rate. However, if the incident power density is too high, particulate density will be

increased thus deteriorates film qualities. Choosing materials with close vapor pressures can help relieve composition segregation on target surface during irradiation and thereby alleviate problem of nonstoichiometry.

3. It is found that using high oxygen pressure does not improve film quality. For example, film coarsening is observed in film grown at oxygen pressure of about 150mTorr. However, maintaining sufficient oxygen pressure is essential to keep stoichiometric Pb/Ti ratio. Because of the contradiction, there is a narrow range of oxygen pressure centered at 100mTorr for optimum $PbTiO_3$-$CoFe_2O_4$ self-assembled film growth.

4. It is shown that $PD^n=const$ (P is oxygen pressure, D is the distance between the substrate and the target) rule for single-phase growth is not valid for two-phase self-assembling growth anymore.

Overall, growth conditions for self-assembled $PbTiO_3$-$CoFe_2O_4$ film are found to be ~903K growth temperature, ~1.0J/cm^2 laser fluence, 100mTorr oxygen pressure, 5Hz repetition rate and 3.7cm target-substrate distance as listed in table3.2.

Chapter 4 Morphology and Nanostructure of $PbTiO_3$-$CoFe_2O_4$ Films

4.1 Introduction

The examples of $x$$PbTiO_3$-($1$-$x$)$CoFe_2O_4$ thin films of different compositions fabricated on differently oriented $SrTiO_3$ substrates using PLD under optimum conditions (Ch. 3) are shown in fig.4.1. All these films demonstrate columnar morphology in the arrangement of constituent phases with distinct interfaces between them. This two phase morphology of the film, i.e. shape and size of the phases and

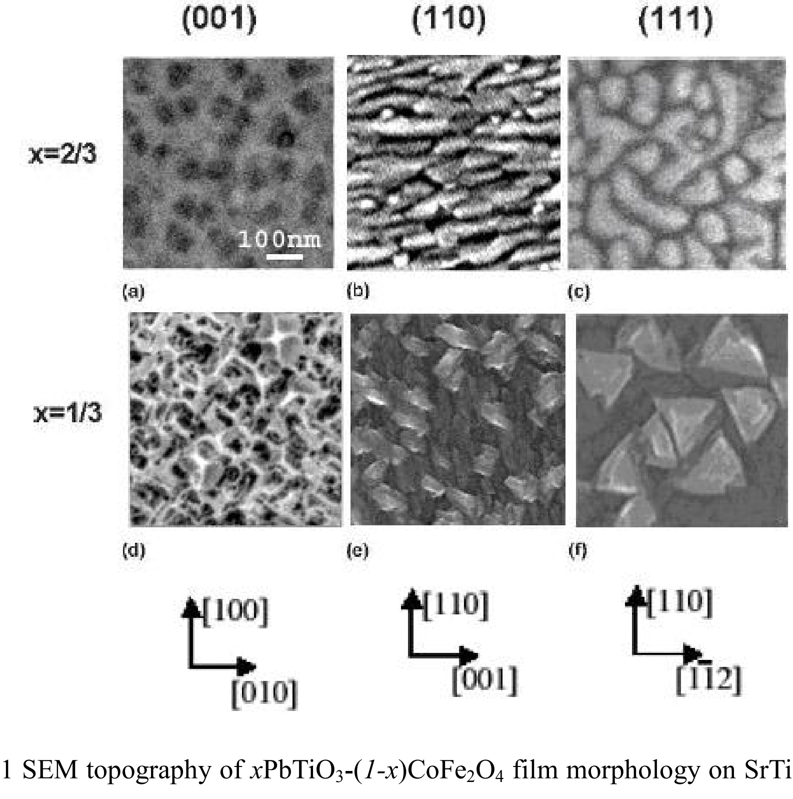

Figure 4.1 SEM topography of $x$$PbTiO_3$-($1$-$x$)$CoFe_2O_4$ film morphology on $SrTiO_3$ of various orientations. White area denotes $PbTiO_3$ and black area denotes $CoFe_2O_4$.

their mutual arrangement, can be described by configuration of interphase interfaces. Depending on the film orientation and/or phase fraction, $PbTiO_3$ can be either inclusions or matrix. For example, $CoFe_2O_4$ phase is observed to form inclusions embedded in $PbTiO_3$ matrix in x=2/3 film on (110) $SrTiO_3$ substrate (fig.4.2b). The interfaces determine crystallographical habitus of inclusion of one phase in the matrix of the other. However, despite an epitaxial (cube-on-cube) relation between the phases, the interfaces have no simple atomic structure even if they go along the close-packed crystallographic planes, for example, {110} or {112}. Usually, they have complex nanostructure formed by the nanosize facets and interface dislocations. Therefore, it is convenient to discuss the interfaces in two scales: nano-interfaces with atomically smooth plane structures and macro-interfaces formed by facets of nano-interface. The configuration of macro-interfaces determines the morphology of the films.

Nanostructure of macro-interfaces depends on many factors including growth phenomena and stress relaxation mechanisms in the phases. However, the formation of faceted interfaces can be explained thermodynamically as a combination of (1) an interface of best macroscopic fitting (corresponding to minimum of elastic energy due to misfit between phases) and (2) an interface of best nanoscopic fitting corresponding to the minimum of the interface energy. This approach is applied to the analysis of interfaces in this chapter.

Although all films have columnar morphology, the macroscopic interfaces can deviate from film normal direction near film surface and near the film/substrate interfaces. Therefore, it is useful to consider separately three different zones of the film: the main zone with interface normal to the film, the top (near surface) zone where the effect of free surface is important and bottom zone where the film growth begin and the structure is strongly determined on the formation of first few layers at the beginning of the growth. The study of nanostructure morphology in the bottom and the top zone as well as comprehensive analysis of experimental data obtained in ours and previous research for main zone allows us to draw an undoubtful conclusion about morphology and interface nanostructure in $CoFe_2O_4/PbTiO_3$ films.

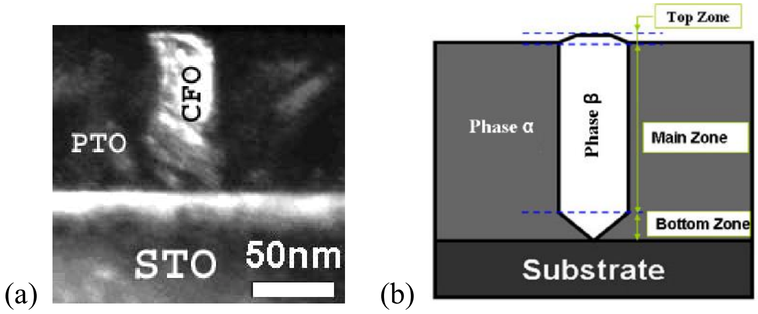

Figure 4.2 (a) Cross-sectional TEM image shows a $CoFe_2O_4$ inclusion embedded in $PbTiO_3$ matrix in x=2/3 film on (110) $SrTiO_3$ substrate. (b) Three different zones of a simplified single inclusion embedded in matrix.

*Characterization Techniques. S*tructures of $CoFe_2O_4$-$PbTiO_3$ films on $SrTiO_3$ substrate are analyzed using scanning electron microscope (SEM) and transmission electron microscope (TEM). Film surface is examined using Hitachi S-4700-II field emission SEM. TEM facility employed in our structure characterization is Philips FEI CM30. TEM sample are prepared using conventional process begin with cutting sample into slices with a low speed precision diamond wafering saw. After sectioning, the specimen slice is gone through mechanical thinning on diamond paper using Gatan apparatus until the sample is thinned down to about 90um. A Gatan dimpler is introduced to further thinning the specimen reducing ion milling times. The dimpling is performed by dripping an etchant onto a relatively soft wheel and grinding a spherical dimple into and partially through the sample so as to form very thin portions around the sample perforation. Gatan ion milling system equipped with a real-time camera is used to produce high quality TEM specimens. Double side, one side ion milling are selected for making cross-sectional TEM samples and plan-view TEM samples respectively.

4.2 Bottom Zone Morphology and Interfaces

For films on (001) $SrTiO_3$, $PbTiO_3$ is found to wet (Terms “wet, wetting, non-wetting” are used to describe our film/substrate interface configurations illustrated in fig.4.3b, 4.4c and do not imply the same meaning as the droplet on surface originality) the $SrTiO_3$ substrate surface while the $CoFe_2O_4$ forms an invert cone shape structure as shown in fig.4.3a. The high resolution cross-sectional image (fig.4.3a) shows sharp interface between $PbTiO_3$ and $CoFe_2O_4$ phases along {111} plane. Two-dimensional schematics of initial stage of $PbTiO_3/CoFe_2O_4$ film on (001) $SrTiO_3$ is illustrated in fig.4.3b.

The wetting/non-wetting situation of $PbTiO_3/CoFe_2O_4$ on (111) $SrTiO_3$ is different from films on (001) $SrTiO_3$ substrate. Even though $PbTiO_3$ has the same

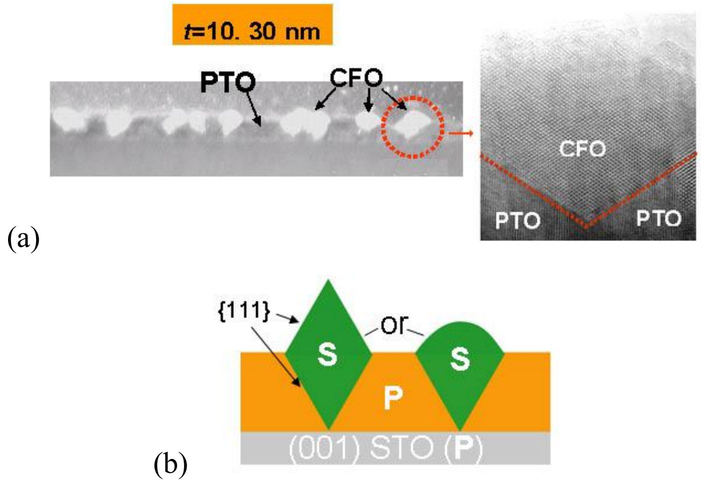

Figure 4.3 (a) Cross-sectional TEM images of $CoFe_2O_4$ embedded in $PbTiO_3$ matrix of x=2/3 film on (001) $SrTiO_3$. Image on the right is the higher resolution TEM image on area around a single $CoFe_2O_4$ inclusion circled by dash line on the left side image. (b) Schematic illustration of wetting/non-wetting scenarios on (001) and (110) $SrTiO_3$ substrates.

crystal structure as $SrTiO_3$ and better lattice fitting on $SrTiO_3$ than $CoFe_2O_4$, it is found experimentally that {111} spinel wets {111} $SrTiO_3$ surface and forms the matrix (fig.4.4a). Fig.4.4a is recorded along <110> zone axis. The angle between the two long green dash lines is about 71^o (fig.4.4a, 4.4b), which suggests that the interface between $PbTiO_3$ and $CoFe_2O_4$ is along {111} plane as well.

The possible explanation why $PbTiO_3$ forms matrix in (001) oriented films while $CoFe_2O_4$ forms matrix in (111) oriented films can be obtained on the basis of thermodynamic arguments. The available data suggest that significantly better lattice fitting of $PbTiO_3$ to $SrTiO_3$ [$a_{(PbTiO3)}$=3.97Å, $a_{(CoFe2O4)}/2$=4.23Å, $a_{(SrTiO3)}$=3.93Å at 903K] and less surface energy [$\gamma_{001(PbTiO3)}=0.97J/m^2$ [67,68], $\gamma_{001(CoFe2O4)}=1.486J/m^2$ [22] highly promote the formation of $PbTiO_3$ matrix on (001) $SrTiO_3$. However, for film of (111) orientation, $CoFe_2O_4$ has much less surface energy than $PbTiO_3$ [$\gamma_{111(PbTiO3)}$~$2.0 J/m^2$ [67,68], $\gamma_{111(CoFe2O4)}$=$0.208 J/m^2$ [22]] which helps $CoFe_2O_4$ to form matrix. In addition, since plane {111} is observed experimentally to be the best contact plane for spinel ($CoFe_2O_4$)/perovskite ($PbTiO_3$, $SrTiO_3$) structure in all three orientations (fig.4.3a, 4.4a, 4.5a), it is natural to suggest that the {111} interface between spinel and perovskite has low interface energy. Thus, the combined effect of lowest surface energy and low interface energy makes preferable growth of first layer of $CoFe_2O_4$ on $SrTiO_3$ although $PbTiO_3$ has better lattice fitting on $SrTiO_3$. With increase of film thickness and increase of elastic energy due to film/substrate misfit, film morphology might have minor changes; however, $CoFe_2O_4$ remains to be the matrix phase through the whole growth process.

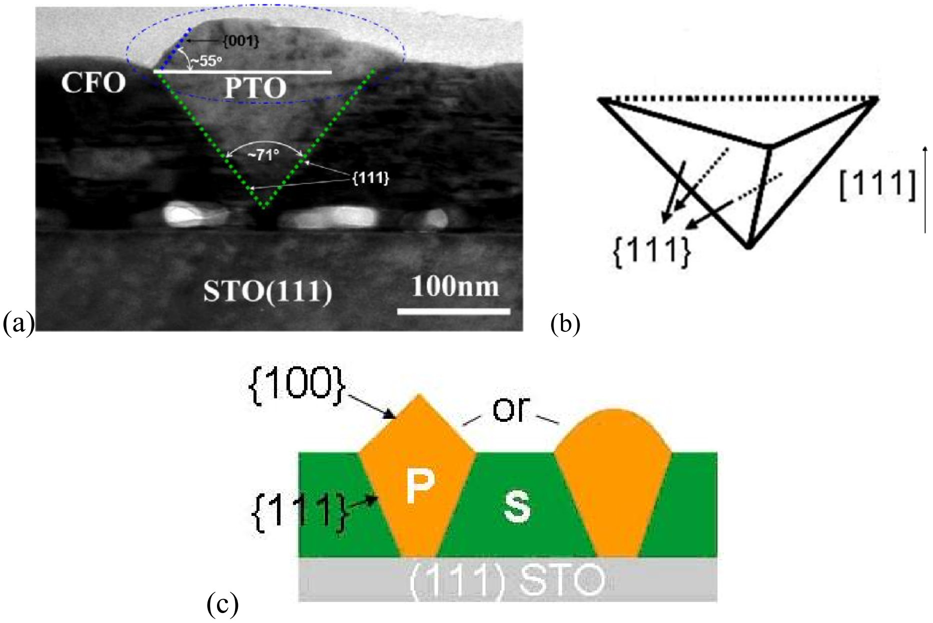

Figure 4.4 (a) Cross-sectional TEM image of x=1/3 film on (111) $SrTiO_3$. (b) Schematics of $PbTiO_3$ with side {111} interfaces. (c) Schematics of wetting/non-wetting of spinel ($CoFe_2O_4$) and perovskite ($PbTiO_3$) on (111) $SrTiO_3$ substrate.

The invert cone shape structure illustrated in fig.4.3a is valid only at the initial stage. At this stage, surface energy effects are very likely larger than the elastic energy effects. While the film grows thicker, effect from surface energy is fading out and elastic energy contribution becomes stronger and eventually results in a microscopical average interface perpendicular to the substrate. For example, for *x*=2/3 film of (110) orientation with 30 nm thickness, isolated $CoFe_2O_4$ with invert cone shape at the bottom is observed in cross-sectional and plan-view TEM images (fig.4.5a). For film

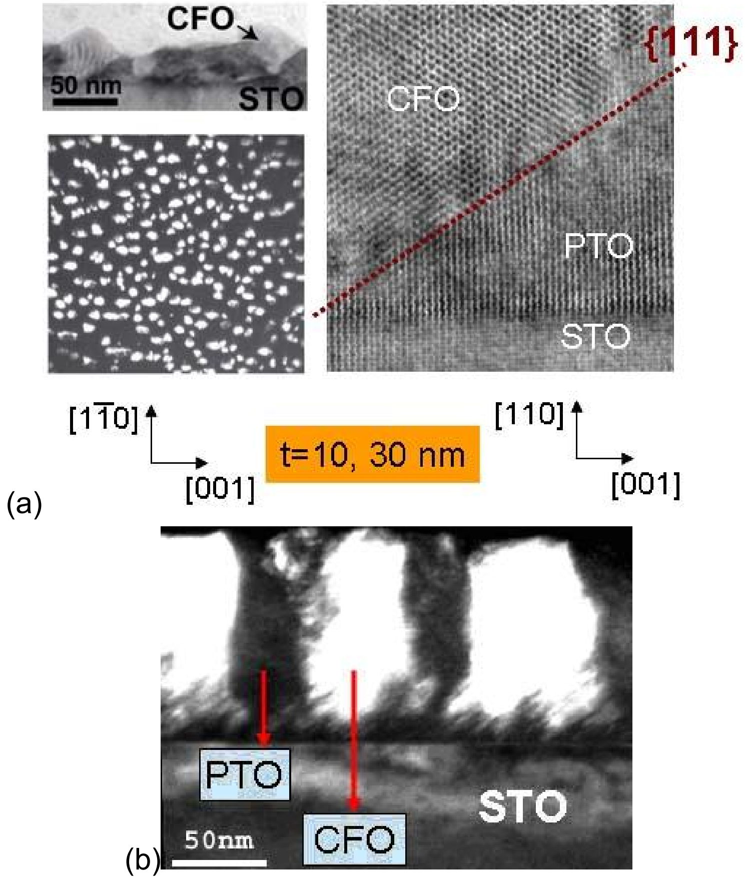

Figure 4.5 (a) Cross-sectional and plan-view TEM images for *x*=2/3 film of ~30nm thickness on (110) $SrTiO_3$. (b) Cross-sectional TEM image for *x*=2/3 film of ~100nm thickness on (110) $SrTiO_3$.

of the same composition and orientation, when thickness is increased to about 100nm, the average interface between the $PbTiO_3/CoFe_2O_4$ changes from inclined at an angle to perpendicular (fig.4.5b).

4.3 Main Zone: Morphology and Interface Nanostructure

4.3.1 Interface Nanostructure for (001) Oriented Films

For film of composition $2/3PbTiO_3$-$1/3CoFe_2O_4$, cross-sectional TEM images (fig.4.6a,b) show columnar structure with $CoFe_2O_4$ inclusion embedded in $PbTiO_3$ matrix. The average orientation of the $CoFe_2O_4$ pillars is along [001] normal to the substrate. The plan-view TEM image (fig.4.6c) shows that those $CoFe_2O_4$ pillars have rectangular shape and intersect film surface along <110> traces. The cross-sectional and plan-view TEM images (fig.4.6a,c) allow us to conclude that the pillars are formed by four macroscopic interfaces along {110} planes perpendicular to the substrate(fig.4.6d). These interfaces are corrugated and further investigation using high resolution TEM image (fig.4.6b) shows that these macroscopic interface are faceted along {111} planes (arrows indicates {111} facets) while maintaining average interfaces along {110} planes. In other words, the {110} interfaces are actually average (macroscopic) interface consisting of large number of small {111} facets (fig.4.6e). Crystallographically, {111} facets alternate about the vertical {110} plane normal to the substrate (fig 4.7a). In fig.4.7a and 4.7b, $CoFe_2O_4$ is presented by a simplified cubic structure. Yellow balls denote Co and Fe atoms; red balls denote oxygen atoms. Four yellow balls at the bottom plane outlines a (001) plane in fig.4.7a.

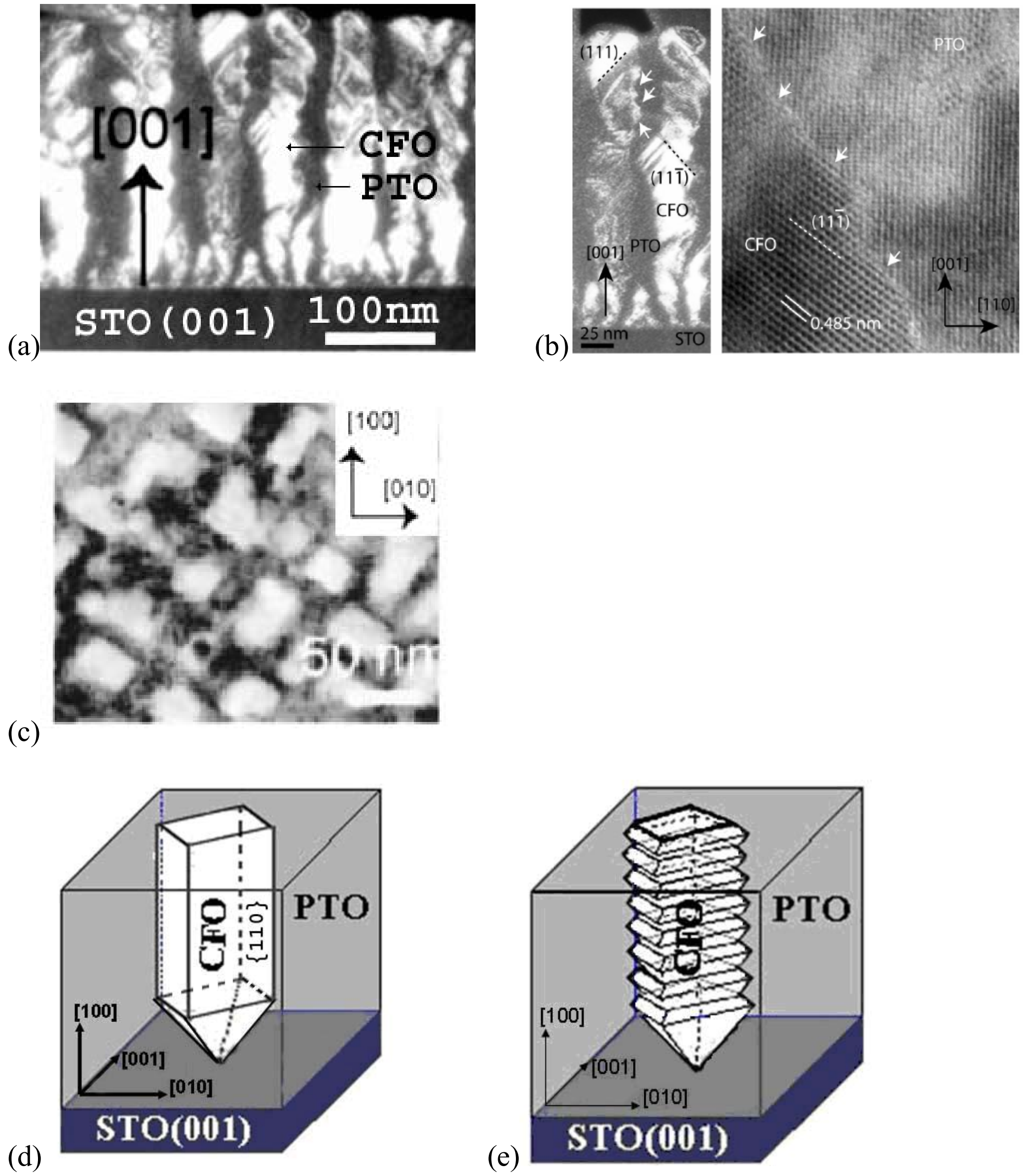
(a)
[001]
CFO
PTO
STO(001)
100nm
(b)
(111)
(111̄)
CFO
PTO
[001]
25 nm
STO
PTO
CFO
(111̄)
0.485 nm
[001]
[110]
(c)
[100]
[010]
50 nm
(d)
CFO
{110}
PTO
[100]
[001]
[010]
STO(001)
(e)
CFO
PTO
[100]
[001]
[010]
STO(001)

Figure4.6 (a),(b),(c) Cross-sectional and plan-view TEM images of the $CoFe_2O_4$ rods in the $x = 2/3$ film grown on (001) $SrTiO_3$. (d),(e) Macro- and nanoscale schematics of single $CoFe_2O_4$ rod embedded in $PbTiO_3$ matrix.

The light blue shadows are {111} planes; Planes marked as A and B are {111} planes of different orientations. As can be seen that the {111} facets can be constructed by zigzagging {111} planes about (011) plane under a sequence of ABAB or BABA as shown in fig.4.7a while maintained the average (011) plane at the same time. Note that the appearance of [110] traces at the film surface gives a {110} interface impression, it is just due to projection of {111} planes on (001) plane as shown in fig.4.7b. After projected {111} planes onto (001) plane, the projected structure (fig.4.7b) consists of two types of configurations: one is elongated along $[1\bar{1}0]$ direction marked by dash orange frame and the other is elongated along [110] direction marked by blue frame, which is found to be analogous to what observed in plan-view TEM (fig.4.6c).

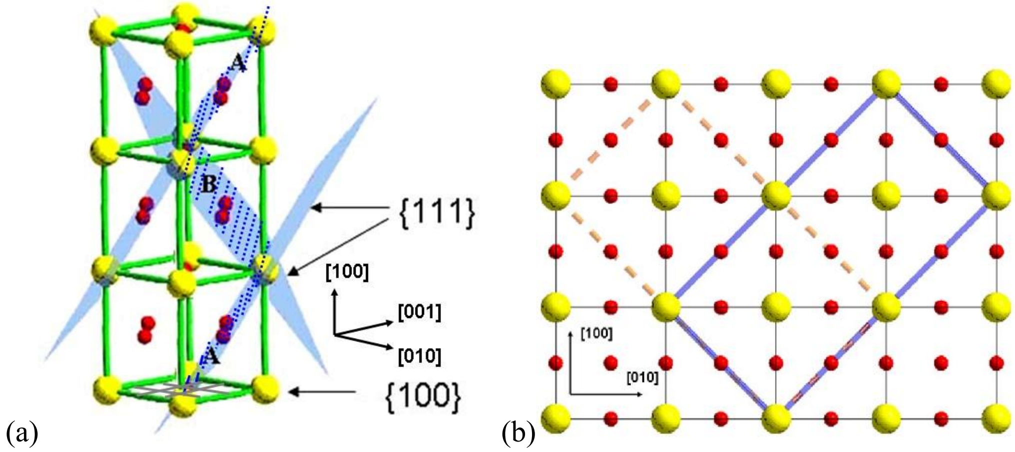

Figure 4.7 (a) Crystallographic illustration of out-of-plane zigzagging {111} plane (A,B) with average (011) plane normal to the substrate. Those dash blue lines are guide to eye showing an example of zigzagging. (b) Crystallographic top view illustration. Solid blue and dash orange lines are projected {111} planes on (001) film surface.

Due to complex nanostructure of interface, it is difficult to observe interface dislocations which are integrated in this nanostructure. However, it can be suggested that intersections of nano-facets form dislocation net which help reduce misfit between the phases. If {111} facets on interface correspond to stacking fault along {111} in $CoFe_2O_4$, the intersections of these planes along <110> on interface can produce interface edge dislocations with Burger's vector along <001> which belongs to interface plane {110} (fig.4.8). This is only one of possible mechanisms of formation of interface dislocations to relax internal stresses due to phase interaction. More future study is needed to address this problem.

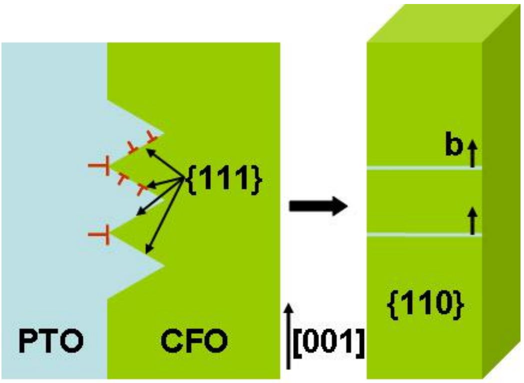

Figure 4.8 Schematics of dislocations at the $PbTiO_3$ and $CoFe_2O_4$ interface.

4.3.2 Interface Nanostructures for (110) Oriented Films

Since it is found for the (001) oriented films that macro-interface along {110} consist of nano-facets along {111}, it is possible to suggest that {111} plane is the best microscopic plane with the lowest interface energy between $PbTiO_3$ and $CoFe_2O_4$ phases. It should be the same in films of all orientations regardless changes of film compositions (fig.4.9a, 4.10a). Unlike zigzagging facets along normal direction for films of (001) orientation with different macroscale and nanoscale morphologies, for films on (110) $SrTiO_3$ substrate, the interfaces between $PbTiO_3/CoFe_2O_4$ phases are plane {111} perpendicular to the (110) substrate. It means that the {111} plane satisfy both the lowest interface energy condition and the minimum elastic energy condition simultaneously for film of {110} orientation. This coincidence results in smooth interfaces along {111} planes perpendicular to the substrate without corrugation, which is in good agreement with TEM observation (fig.4.9a, 4.9c). From the plan-view TEM image (fig.4.9b), the lamellae in the {101}-oriented films intersect film surface along two nonequivalent <112> directions maintained an angle of ~±35° against in-plane [100] direction. For film of the other composition, similar phenomenon is observed (fig.4.10a) though the structure changes from $CoFe_2O_4$ lamellas embedded in $PbTiO_3$ matrix to $PbTiO_3$ platelets embedded in $CoFe_2O_4$ matrix. Irrespective of different inclusion phases for films of different compositions, the inclusions should have similar crystallographic relations based on the crystallography analysis (fig.4.9e,f). In fig.4.9e, orange and blue shadows are {111} planes perpendicular to (101) surface. Two in-plane intersected segments can be found in fig.4.9e: either AB_1 or AB_2. It is clear in fig.4.9f which shows projected {111} planes on (101) surface. The projected planes give facets along <112> traces aligned at ~ ± 35° with respect to in-plane [010] direction. That is what observed experimentally (fig.4.9b, 4.10a, 4.10b). Based on the macro- and nanoscale interface analysis, a single $CoFe_2O_4$ inclusion embedded in $PbTiO_3$ matrix for film of {101} orientation can be schematically constructed as shown in fig.4.9d. Similarly, isolated $PbTiO_3$ platelets embedded in $CoFe_2O_4$ matrix can be schematically illustrated as in fig.4.10c with {111} interfaces perpendicular to the substrate and intersect the film surface along <112> traces.

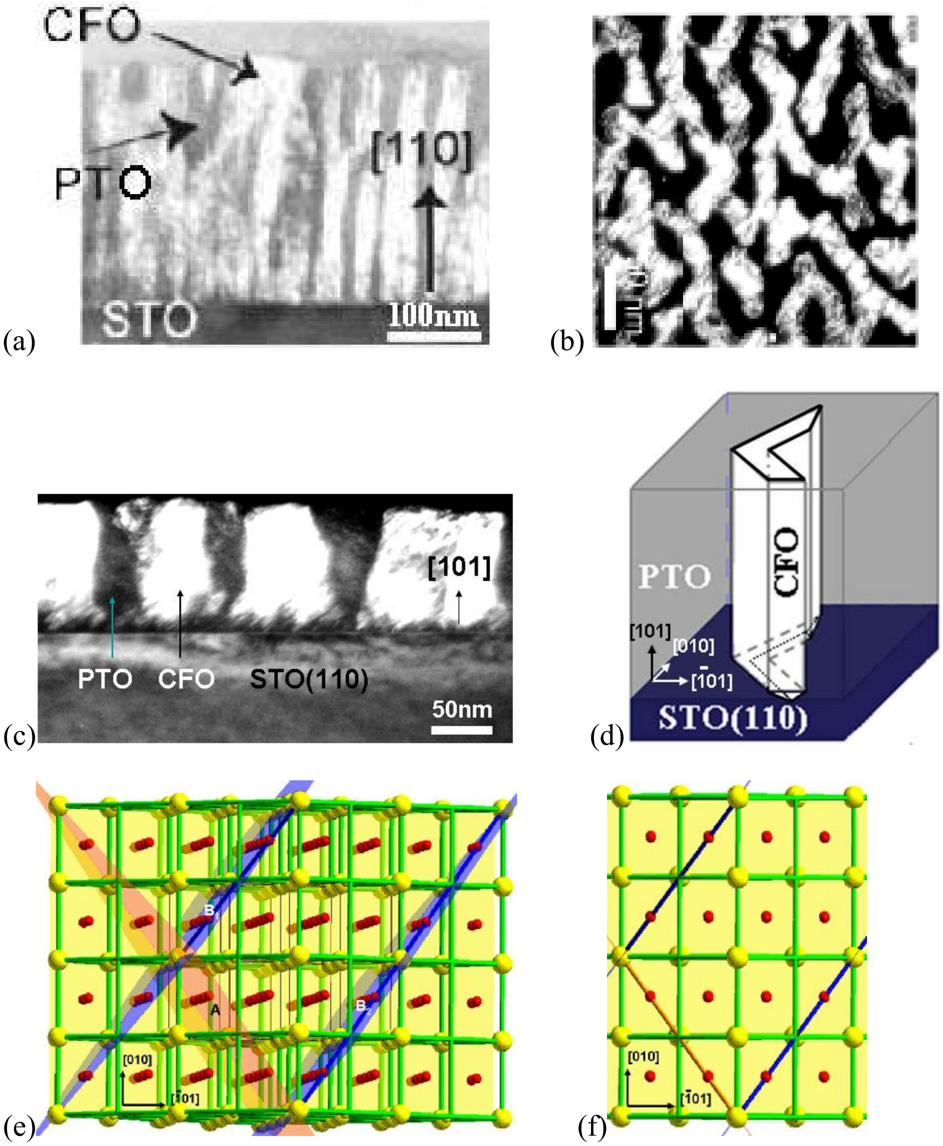
CFO
PTO
[110]
STO
100nm
(a)
(b)
[101]
PTO
CFO
STO(110)
50nm
(c)
PTO
CFO
[101]
[010]
[$\bar{1}$01]
STO(110)
(d)
B1
A
B2
[010]
[$\bar{1}$01]
(e)
[010]
[$\bar{1}$01]
(f)

Figure 4.9 (a),(b),(c) Cross-sectional, plan-view TEM images of $CoFe_2O_4$ lamellas in x=2/3 film grown on (110) $SrTiO_3$. (d) Schematic of single $CoFe_2O_4$ lamellae embedded in $PbTiO_3$ matrix. (e) Crystallographic illustration of in-plane zigzag {111} planes (A, B_1, B_2) along <112> direction. (f). Crystallographic top view of {111} planes projected on (101) plane. Blue and orange line are different {111} planes.

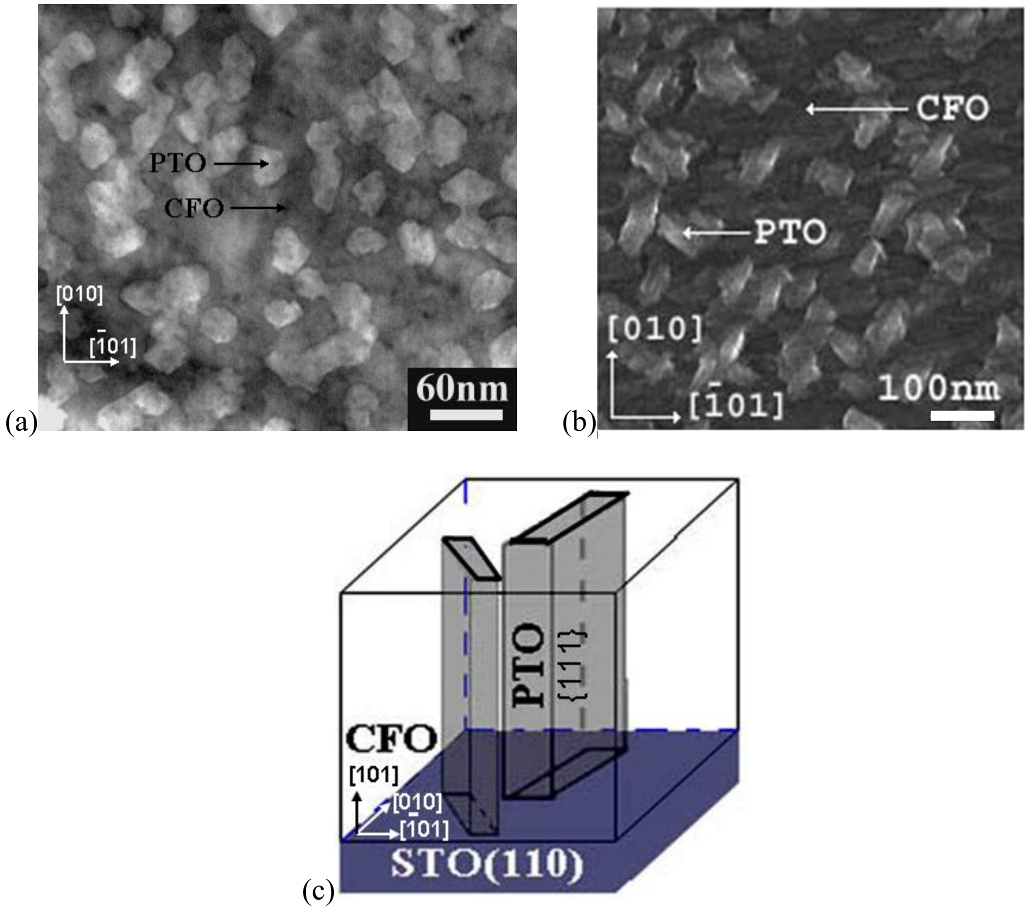

Figure 4.10 (a)Plan-view TEM image of $PbTiO_3$ platelets in x=2/3 film grown on (110) $SrTiO_3$. (b) SEM image of x=1/3 film on (110) $SrTiO_3$. $PbTiO_3$ appears as platelets embedded in $CoFe_2O_4$ matrix (c) Schematic of $PbTiO_3$ platelets embedded in $CoFe_2O_4$ matrix.

4.3.3 Interface Nanostructures for (111) Oriented Films

Regardless of different compositions (x=1/3, 2/3), $PbTiO_3$ forms inclusions embedded in $CoFe_2O_4$ matrix in films on (111) $SrTiO_3$ substrate (fig.4.1 fig.4.11a-c). Even though high resolution TEM image shows <112> traces in the plan view image (fig4.11c) and gives a false appearance of interface along{112} plane, {112} planes are not favorable crystallographic planes from point of interface energy. As observed in (001) oriented thick film (fig.4.6b) and thin films of all orientations (fig.4.3a, 4.4a

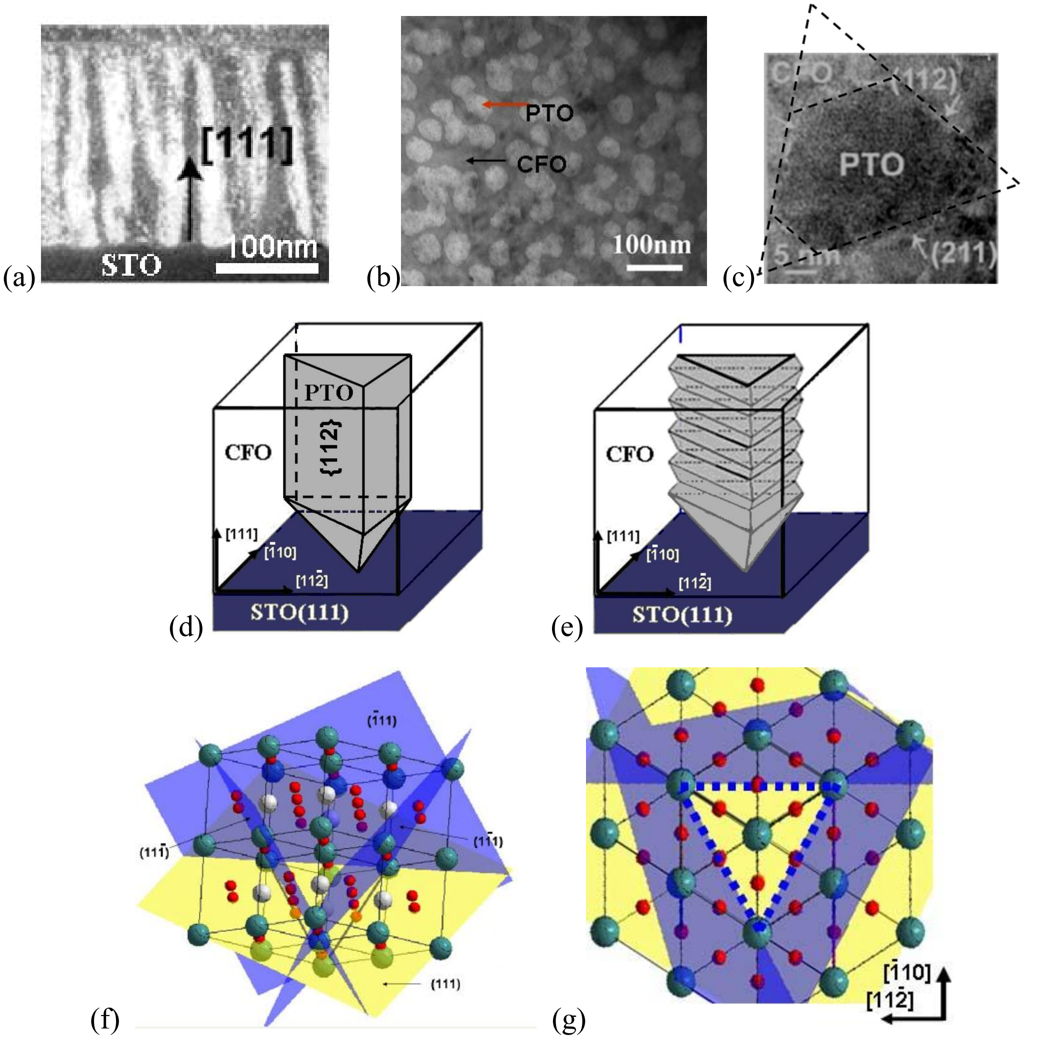
(a)
[111]
STO
100nm
(b)
PTO
CFO
100nm
(c)
CFO
(112)
PTO
5 nm
(211)
(d)
PTO
{112}
CFO
[111]
[1̄10]
[112̄]
STO(111)
(e)
CFO
[111]
[1̄10]
[112̄]
STO(111)
(f)
(1̄11)
(111̄)
(11̄1)
(111)
(g)
[1̄10]
[112̄]

Figure 4.11 (a),(b) Cross-sectional and plan-view images of the *x* = 1/3 films on the (111) $SrTiO_3$ showing the $PbTiO_3$ rods (bright) in the $CoFe_2O_4$ matrix (dark). c) Low-magnification high-resolution TEM image showing faceting of the $PbTiO_3$ nanorods. (d),(e) Schematics of micro- and nanoscale single $PbTiO_3$ pillar embedded in $CoFe_2O_4$ matrix on (111) $SrTiO_3$ substrate. (f) Crystallographic illustration of {111} planes on (111) surface. (g) Crystallographic top view illustration of {111} planes projected on $(1\bar{1}1)$ plane. The dash blue lines denote the intersection of projected {111} planes on film surface along <112> traces.

and 4.5a) , it can be concluded that {111} plane has the lowest interface energy between $PbTiO_3$ and $CoFe_2O_4$. Thick film of {111} orientation should have the same {111} interface between film constituent phases as well. After projected {111} planes on (111) surface plane (fig.4.11g), it is easily perceived that the projected structure in fig.4.11g marked by dash blue lines mimics what is observed in SEM images (fig.4.1f). The projected {111} planes form a triangle with edges along <112> traces on film surface, which is in good agreement with the plan-view observations (fig.4.9c) except small interceptions along <112> at places close to the vertex angles. It is likely that the small interceptions are formed to reduce the elastic energy at the sharp vertex angles. A single faceting $PbTiO_3$ pillar in $CoFe_2O_4$ matrix is constructed and illustrated in fig.4.11d and 4.11e. Fig.4.11d shows a single pillar with macroscopical interface along {112} plane and fig.4.11e shows a single pillar with nano-facets along {111} planes while maintaining the {112} average interface orientation.

4.4 Top Zone Structures

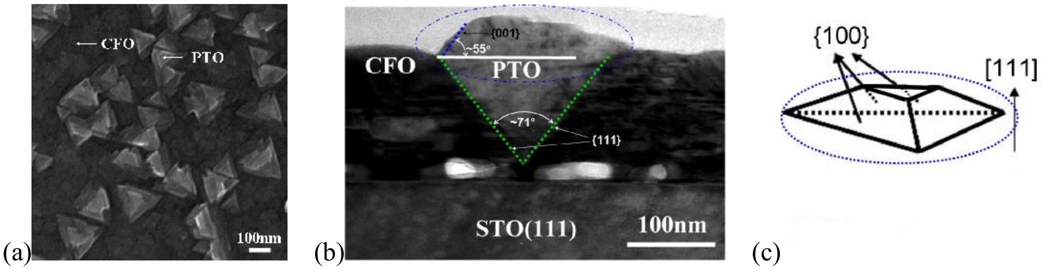

Figure 4.12 Nanostructure of x=1/3 film on (111) $SrTiO_3$ substrate. (a) SEM topography.

(b) Cross-sectional TEM image showing $PbTiO_3$ top side facets marked by dash blue circle.

(c) Schematics of $PbTiO_3$ top region side facets circled in (b) by dash blue line.

Figure 4.12a is a SEM image of x=1/3 film on (111) $SrTiO_3$ substrate showing $PbTiO_3$ triangles distributed in $CoFe_2O_4$ matrix. The cross-sectional TEM image (fig.4.12b) show that those triangles are not at the same horizontal level as $CoFe_2O_4$ matrix. The $PbTiO_3$ triangles are protruded out of the film surface for about 40nm. As the protruded portion has free surface instead of forming an interface with $CoFe_2O_4$ phase or substrate, the protruded faceting surface should prefer planes of the lowest surface energy, which is {100} for perovskite $PbTiO_3$ [22]. TEM image (fig.4.12b) with <110> viewing direction shows the side facet forms an angle of ~55^o against the film surface, which lead to a conclusion that the protruded island are side faceting along {100} planes. Both the SEM and TEM images indicate flat top of the protruded island. Observations in the SEM and TEM images lead to a structure of protruded island consisting of three {100} side facets in addition to a flat {111} top surface (fig.4.12c). It is obvious from the SEM analysis (fig.4.1) that film topographies are orientation dependent, however, our experimental observation allow us to suggest that the side facets of protruded top zone are determined by surface energy and it is highly possible that the $x$$PbTiO_3$-($1$-$x$)$CoFe_2O_4$ films with different topographies should have the same {100} side facets for $PbTiO_3$ inclusions and {111} side facets for $CoFe_2O_4$ inclusions at the protruded top zone because of lowest surface energy at these planes. This conclusion is supported by other reported experimental results as well [12].

4.5 Discussion and Conclusion

As it has been shown in our studies of self-assembled $PbTiO_3$-$CoFe_2O_4$ films on $SrTiO_3$ substrates, their two-phase morphologies can be controlled by change of orientation of substrates.

In case of (001) orientation, films are formed by $CoFe_2O_4$ pillars with rectangular shape. On macroscopic scale, the pillar faces correspond to {110} plane normal to substrate. However, these pillars consist of nano-facets along the {111} plane. $PbTiO_3$ forms matrix independently of film compositions.

In case of (111) orientation, films are formed by $PbTiO_3$ pillars with truncated triangle or round shape. On macroscopic scale, the plane section of interface between $PbTiO_3$ pillars and $CoFe_2O_4$ matrix is oriented along {112} plane normal to the substrate. These interfaces are formed by nano-facets along {111} plane. $CoFe_2O_4$ forms matrix independently of film compositions.

In case of (110) orientation, interface between film phases are {111} plane and do not reveal nanoscale facets. This observation allows us to conclude that plane {111} is the plane of best atomic fitting with minimum interface energy between crystalline lattices of perovskite $PbTiO_3$ and spinel $CoFe_2O_4$. However, this plane can not satisfy the condition dictated by film growth to be normal to the substrates with (100) and (111) orientation. Therefore, microscopical interface between the phases for these orientations are {110} and {112} planes which should correspond to the minimum elastic energy of misfit between these phases. This conclusion is supported by thermodynamics based phase field modeling [20,37]. The trend to minimize interface energy results in formation of interface faceting structure with {111} nano-facets.

The study of initial stage of film growth has strongly supported the conclusion that {111} interface is the preferable contact plane between $CoFe_2O_4$ and $PbTiO_3$.

The faceting interfaces is an important factor that can affect multiferroic properties of self-assembled nanostructures. Faceting nanostructure of interfaces together with the interface dislocations enable minimize internal stresses due to misfit between the phases at temperature higher than Curie point of ferroelectric phase. We believe the {111} nano-faceting interface observation is a generic result that can be applied to other perovskite-spinel systems. For example, {111} nano-facets can be expected in self-assembled nanostructure in $BaTiO_3$-$CoFe_2O_4$ film on (001) $SrTiO_3$. Indeed, it can be seen in presented cross-sectional TEM images of (001) oriented film published in ref.69.

In film-substrate system under investigation, $PbTiO_3$ and $SrTiO_3$ are perovskite with very close lattice parameters. Therefore, $PbTiO_3$ is expected to form matrix if it is major fraction of the films. However, it is not true in case of (111) orientation. Due to very low energy for {111} surface of $CoFe_2O_4$ and low $CoFe_2O_4$/$SrTiO_3$ interface energy [22], the first few layers of $CoFe_2O_4$ on (111) $SrTiO_3$ substrate can have less energy than $PbTiO_3$ on (111) $SrTiO_3$. In this case, the initial stage of growth determines morphology of nanostructures: $PbTiO_3$ rods embedded in $CoFe_2O_4$ matrix while the shape of the rods can be determined by elastic interactions between the phases. That is an explanation of fundamental change of nanostructure morphologies from $CoFe_2O_4$ pillars in $PbTiO_3$ matrix for (001) film orientation to $PbTiO_3$ rods in $CoFe_2O_4$ matrix for (111) oriented film.

Chapter 5 Accommodation of Transformation Strains in Self-Assembled $CoFe_2O_4$-$PbTiO_3$ Nanostructures

Chapter 5.1 Introduction

Multiferroic composite films that consist of magnetostrictive and piezoelectric phases arranged in transverse architectures exhibit significant magnetoelectric effects due to a reduced clamping by the substrate. The strain mediated magnetoelectric (ME) response of transverse multiferroic nanostructures depends strongly on the efficiency of elastic interactions across the interphase boundaries as well as on the sign and level of residual stresses in the component phases. The transformation between paraelectric and ferroelectric state of perovskite component during cooling or heating generates residual stresses accompanied by strong lattice distortion, especially for $PbTiO_3$. Unlike single-phase thin layers on a substrate, the individual phases in the transverse nanostructures are confined three dimensionally. In this chapter, we present the result of variable-temperature X-Ray study which is used to analyze the strain evolution and the effect of constraints on the ferroelectric phase transition in epitaxial self-assembled $CoFe_2O_4$-$PbTiO_3$ films on $SrTiO_3$ substrates.

5.2 Experiments

The $x$$PbTiO_3$-$(1-x)$$CoFe_2O_4$ films (x=1/3, 2/3) were grown on $SrTiO_3$(100) substrates from composite targets with fixed compositions using pulsed laser deposition. Thickness of the films is ~230nm for both compositions. The observation of strain relaxation was conducted in a Bruker D8 Discover X-ray diffractometer equipped with a high-temperature stage. Room-temperature values of the out-of-plane

($a_\perp$) and in-plane ($a_{||}$) were determined for each phase using four non-equivalent reflections (e.g. 002, 202, -202 and 222 for PbTiO3). For these measurements, the incident beam was conditioned using a Gobel mirror and a 4-bounce Ge (220) monochromator. Lattice parameters were monitored along with temperature changes using $004_{PTO}/008_{CFO}$ and $220_{PTO}/440_{CFO}$ reflections and Cu K_α radiation. X-ray diffraction patterns for the $CoFe_2O_4$–$PbTiO_3$ films were collected at 25K intervals between the ambient temperature and 903K. The temperatures were confirmed to be accurate within 5 degrees. Heating-cooling cycling in the 298–903K range demonstrated that the changes in the lattice parameters were fully reversible. Room temperature lattice parameters for $PbTiO_3$ and $CoFe_2O_4$ are summarized in Table 5.1.

Table 5.1 Room temperature values of lattice parameters of $PbTiO_3$ and $CoFe_2O_4$ in the composite $x$$PbTiO_3$-*(1-x)*$CoFe_2O_4$ films. The numbers in parentheses represent combined statistical uncertainties (1σ) from the x-ray profile fitting and squares refinements using four nonequivalent reflections.

x	$PbTiO_3$		$CoFe_2O_4$	
	$a_\perp$	$a_{//}$	$a_\perp$	$a_{//}$
2/3	4.035(1)	3.945(1)	8.420(1)	8.383(1)
1/3	4.008(1)	3.959(1)	8.396(1)	8.368(1)

At room temperature, the distribution of *d*-spacing values in $PbTiO_3$ was significantly broader than that in $CoFe_2O_4$, as inferred from the relative widths of the 002_{PTO} (full width at half maximum (FWHM) is 0.49°, x=1/3, fig.5.1) and 004_{CFO}

(FWHM=0.29°, *x*=1/3, fig.5.1), peaks, respectively. The 002_{PTO} rocking curve (FWHM=0.79°, *x*=1/3, fig.5.2a) was also broader than the 004_{CFO} rocking curve (FWHM=0.73°, *x*=1/3, fig5.2b)

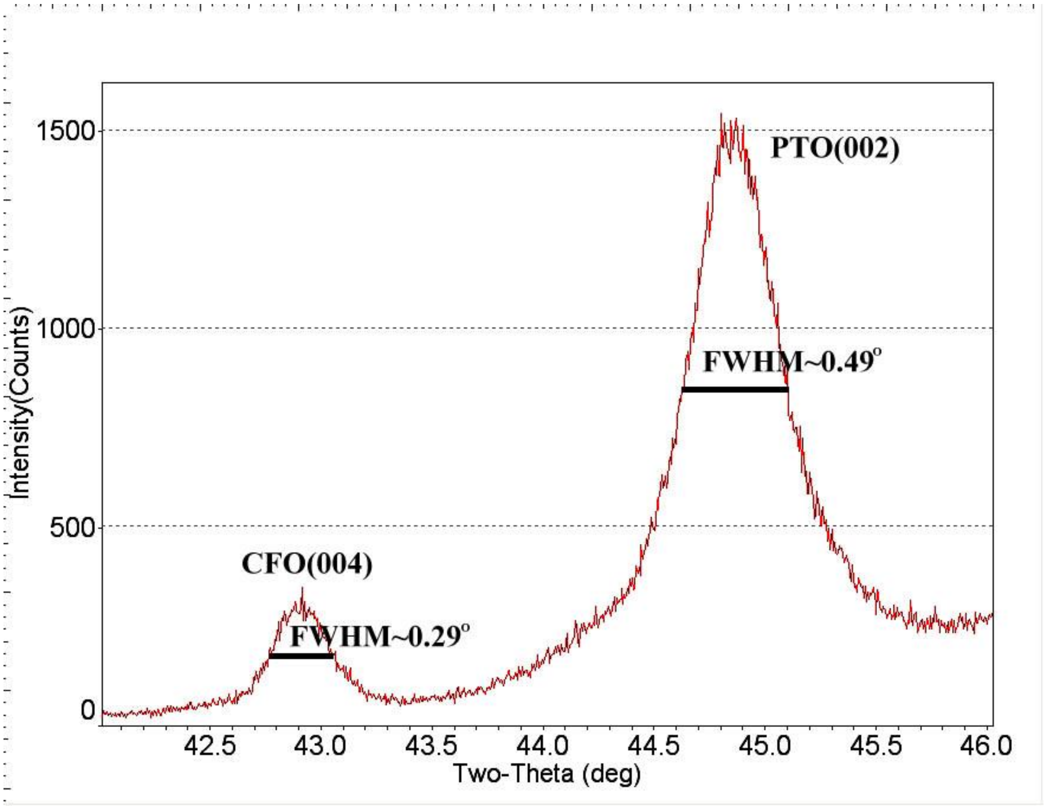

Figure 5.1 X-Ray spectrum for $2/3CoFe_2O_4$-$1/3PbTiO_3$ film on $SrTiO_3(001)$ substrate. Full width at half maximum (FWHM) are 0.49°, 0.29° for 004_{CFO} and 004_{CFO} peaks respectively.

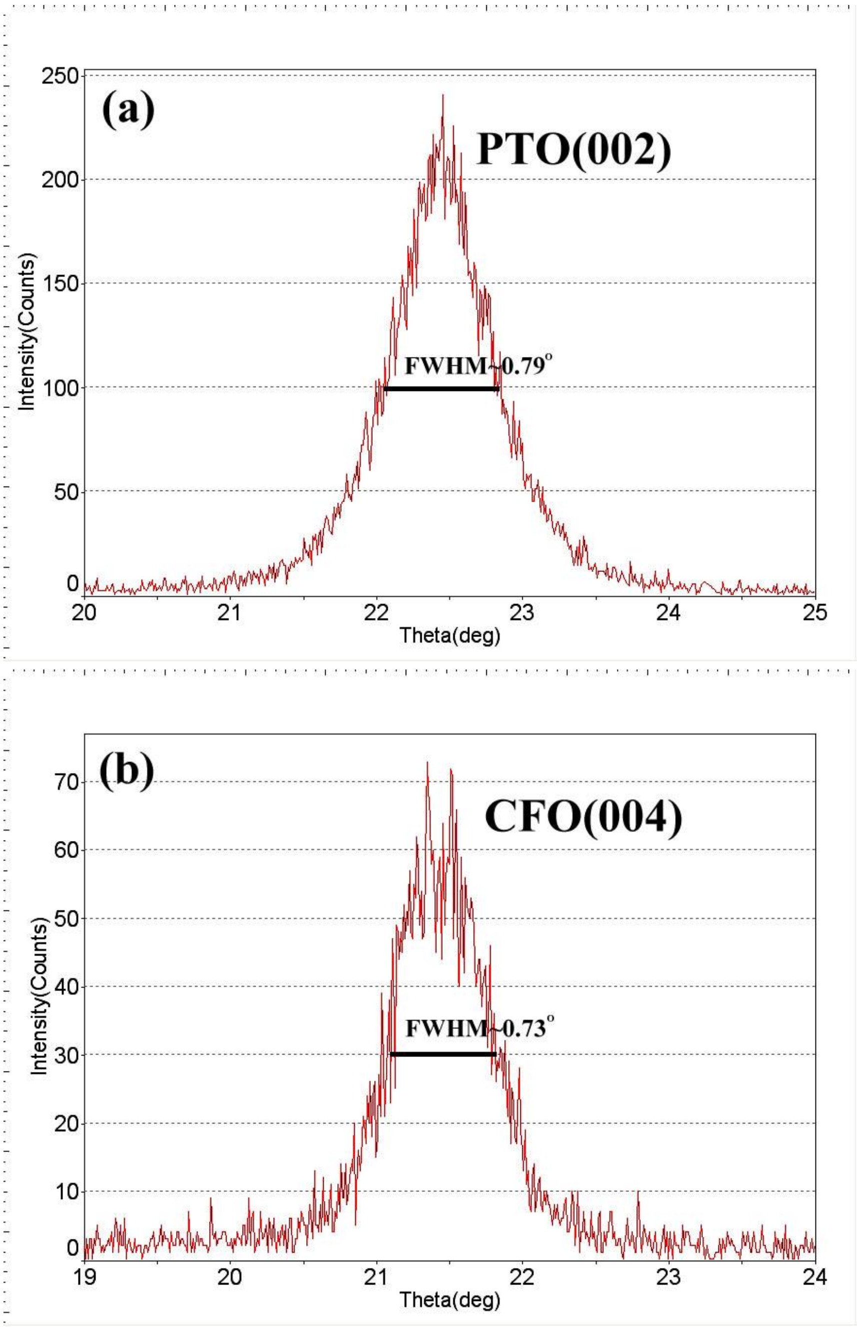

Figure.5.2 Rocking curves for 002_{PTO} and 004_{CFO} peaks in fig.5.1. (a) 002_{PTO} rocking curve with FWHM of 0.79° (b) 004_{CFO} rocking curve with FWHM of 0.73°.

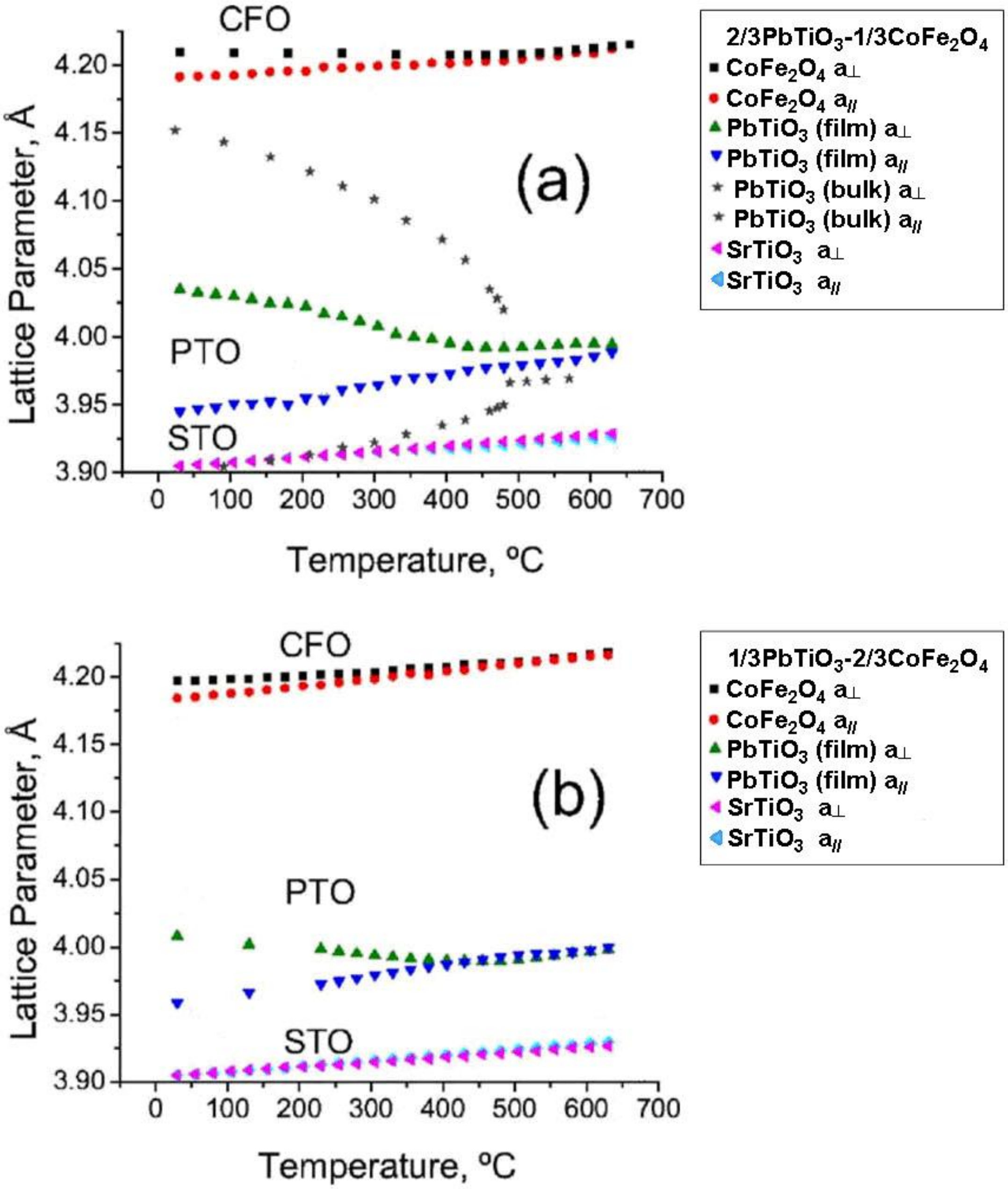

Figure. 5.3 Out-of-plane ($a_\perp$) and in-plane ($a_\parallel$) lattice parameters of $CoFe_2O_4$ (black squares and red dots) divided by 2, $PbTiO_3$,(green and blue triangles) and $SrTiO_3$ (purple and light blue triangles) in the $x$$PbTiO_3$-($1$-$x$)$CoFe_2O_4$ films on $SrTiO_3$(100) substrate measured as a function of temperature. Lattice parameters of bulk $PbTiO_3$ [70] are shown in (a) using asterisks. (a) x=2/3 and (b) x=1/3.

Figure 5.3 demonstrates results of the variable-temperature lattice parameters measurements in the films with x=1/3 (Fig. 5.3a) and x=1/3 (Fig. 5.3b); the data for bulk $PbTiO_3$ [70] are superimposed in Fig. 5.3a using asterisks. Structure transformation from cubic to tetragonal phase in $PbTiO_3$ is clearly observed at T_c~723K as a divergence of the $a_{\perp}$(T) and $a_{//}$(T) lattice parameters. Similar transition temperature is observed on figure 5.3b for film with the other composition. Though it was reported that epitaxial stresses that arise during growth are largely relaxed by misfit dislocations [13], a small tetragonal distortion of $PbTiO_3$ and $CoFe_2O_4$ above T_c (fig 5.3a) due to the nonrelaxed epitaxial stresses still can not be ruled out. Above T_c(~723K), the width of the 002_{PTO} reflection in the θ-2θ scans decreases dramatically and become comparable to that of the 004_{CFO}; concurrently, the integrated intensities of the 002_{PTO} reflections in the x=2/3 and x=1/3 films increase by the factors of ~2.25 and ~3 respectively. In contrast, the 004_{CFO} integrated intensity of reflection remains unchanged, regardless of phase fractions. The width of the 002_{PTO} rocking curve decreases by nearly a factor of 2 above the transition while some, though much smaller, narrowing of the 004_{CFO} rocking curve is observed as well. These results indicate that a broad distribution of the d-spacing values along with the broad mosaics, as encountered at room temperature in $PbTiO_3$, is associated with a phase transition rather than a growth process.

The transition temperature for $PbTiO_3$ in the composite films is about 45K lower than that in the bulk crystals (768K). The tetragonal distortion in $PbTiO_3$ is strongly suppressed yielding the c/a ratio (room temperature) of only ~1.023 for x=2/3 and

~1.013 for x=1/3 as opposed to c/a~1.064 for bulk $PbTiO_3$ crystals. The distortion of $PbTiO_3$ due to phase transition is suppressed by constrains from $CoFe_2O_4$ and thereby modifying the character of this transition from the strongly first order towards second order. The effect becomes stronger with increasing volume fraction of $CoFe_2O_4$. At the same time, a tetragonal distortion $a_\perp/a_\parallel>1$ in $CoFe_2O_4$ is observed as a result of the expansion of $PbTiO_3$. Values of the $CoFe_2O_4$ distortion varies from 1.004 for x=2/3 to 1.003 for x=1/3 at room temperature. As expected from the stress equilibrium conditions, the out-of-plane strains in $CoFe_2O_4$ decrease as the volume fraction of this phase increases, while an inverted trend is observed for $PbTiO_3$ strains. The spontaneous polarization of $PbTiO_3$ in composite films is expected to be smaller compared to its strain-free bulk value as a result of the suppressed c/a ratio.

5.3 Effect of Constraint on T_c and Nanostructure of $PbTiO_3$

The effect of elastic constraints on the Curie temperature of a ferroelectric in the composite film can be predicted by considering a free energy expansion for a constrained ferroelectric film on a substrate:

$$F=A(T-T_0)P^2+BP^4+CP^6+F_{\mathrm{el}} \tag{5.1}$$

where A, B, and C are the Landau coefficients and F_{el} is the elastic energy of the film. The F_{el} of a film consisting of cylindrical magnetic rods embedded into a ferroelectric matrix was calculated previously [21,14]. Neglecting self-strain of the magnetic phase, this energy can be expressed as:

$$F_{el}=[(1-\text{[illegible]})GQ_{11}^2(1-\delta)(1+\delta-2v\delta)+GQ_{11}^2 2\delta^2(1+v)]P^4 \tag{5.2}$$

where [illegible] is a volume fraction of the PbTiO3 phase, G is the in-plane elastic modulus of the film, υ is a Poisson ratio, Q_{11} and Q_{12} are electrostrictive coefficients of a ferroelectric phase, and $\delta = Q_{12}/Q_{11}$. Evidently, the energy associated with the interphase elastic interactions modifies just the P^4 term in the free energy expansion and thus should have no effect on the Curie temperature of a ferroelectric. However, this elastic energy affects the sign of the P^4 term thereby changing the character of a ferroelectric phase transition from the first to second order, consistent with the experimental observations (Fig. 5.3). The change in the T_c associated with this change in the order of the transition is expected to be ~13K [71], which is essentially less than the experimentally observed data.

Reduced values of a ferroelectric transition temperature in the composite films can be readily attributed to a limited but detectable dissolution of Fe in $PbTiO_3$ and dissolution of Ti in $CoFe_2O_4$ [13]. Concurrently, the transformation strain and the resulting strain-free *c*/*a* ratio for the $Pb(Ti,Fe)O_{3-\delta}$ solid solutions in the $CoFe_2O_4$–$PbTiO_3$ nanostructures should be reduced substantially compared to the pure $PbTiO_3$. Reportedly, the T_c value decreases from 768K from pure $PbTiO_3$ (a=3.899A, c=4.15A, c/a=1.064) to 420°C for $Pb(Ti0.5Fe0.5)O_{3-\delta}$ (a=3.928A, c=4.036A, c/a=1.028) [72]. Assuming a linear dependence of T_c and c/a ratio on composition, the T_c~723K observed for $PbTiO_3$ in the present films suggests up to 25 at.% of Fe substitution and c/a~1.042. The uncertainties in the strain-free states of the component phases caused by formation of the solid solutions preclude accurate determination of residual strains in the composite nanostructures. However, variable temperature measurements provide an insight into the strain accommodation mechanism as discussed below.

Strain compatibility conditions along the $CoFe_2O_4/PbTiO_3$ interfaces imply equal changes of the out-of-plane lattice parameters of $CoFe_2O_4$ and $PbTiO_3$ from their respective values in the cubic state just prior to a ferroelectric phase transition. However, the expansion of $a_\perp$ in $PbTiO_3$ observed in Fig.5.3 exceeds significantly the out-of-plane strain in $CoFe_2O_4$. Considering a reversibility of the lattice parameters upon the heating/cooling cycles, this discrepancy can be accounted for by formation of the 90° twin domains in $PbTiO_3$. Indeed, $PbTiO_3$ 90° twin domains are identified in both TEM diffraction-contrast image (fig.5.4) and XRD reciprocal space maps (fig.5.5). The $PbTiO_3$ was confirmed to possess two *a*-domain variants in addition to the *c*-domains. As a result, the average out-of-plane deformation in $PbTiO_3$ is significantly smaller than that observed just for the *c*-domains.

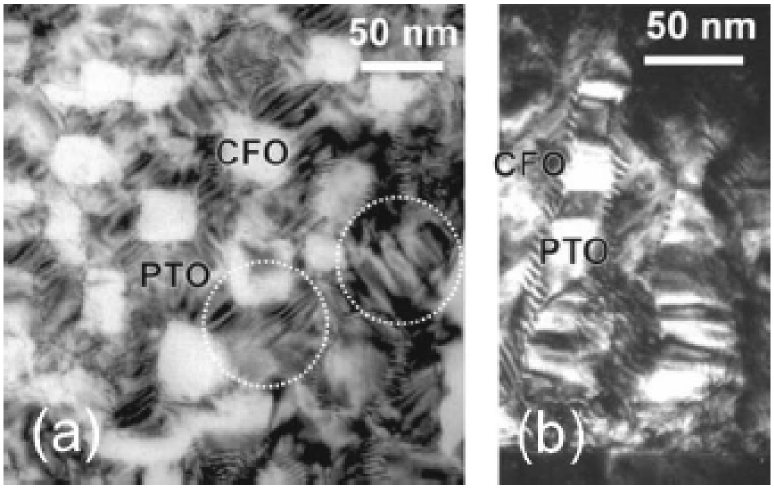

Figure 5.4 Plan-view (a) and cross-sectional (b) TEM images of the x=1/3 film. Twin domains in $PbTiO_3$ are observed as circled.

Experimentally, the volume fraction of the $PbTiO_3$ *c*-domain (β) can be estimated from the relation of the integrated intensities of the 001 and 100(×4) peaks in the x-ray diffraction rocking curves is approximately 0.5; however, the accuracy of these measurements is limited by the relatively poor separation of the broad *a*-domain peaks.

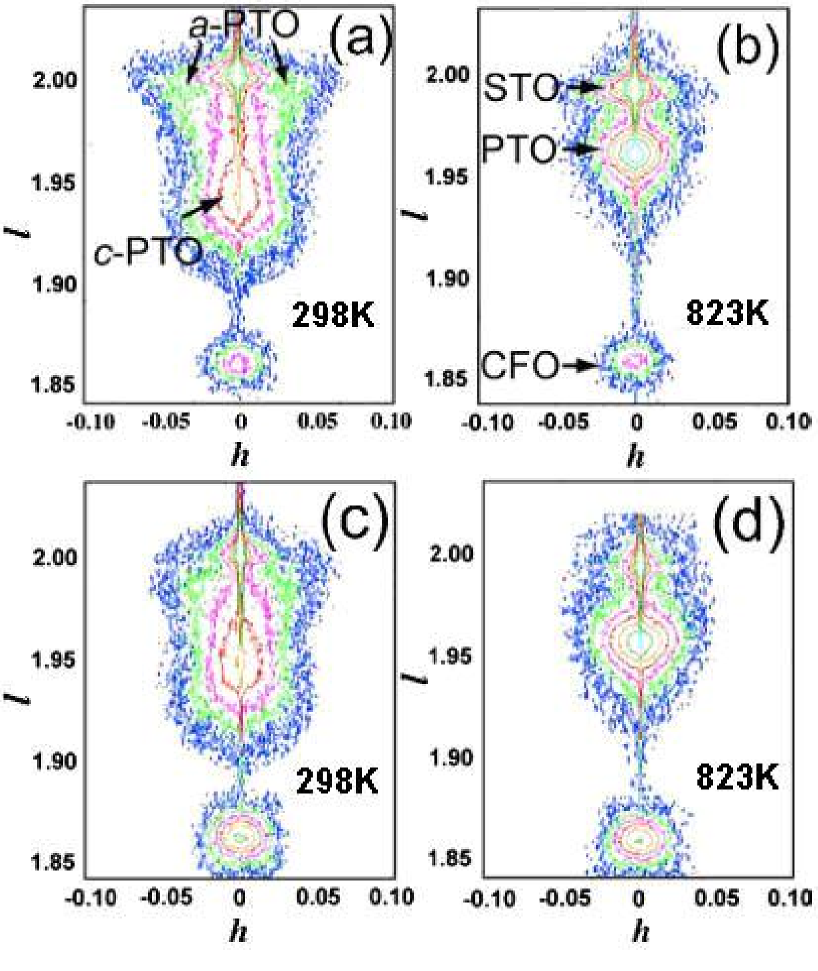

Figure 5.5 Low-resolution reciprocal space maps encompassing 200 $SrTiO_3$, 002/200 $PbTiO_3$, and 004 $CoFe_2O_4$ reflections for films with x=2/3 [(a) and (b)] and x=1/3 [(c) and (d)] acquired at 298K ((a) and (c)) and 823K ((b) and (d)). Appearance of *a*-domains in $PbTiO_3$ below a ferroelectric transition can be observed.

After cooling down to room temperature, $PbTiO_3$ can have three different domain states (c, a1 and a2 domains) as illustrated in fig.5.6. It is demonstrated in the x-ray analysis that both $PbTiO_3$ and $CoFe_2O_4$ as deposited have cubic structure and internal stress can be negligible (fig.5.7a,b). After cooled down to room temperature, if all cubic $PbTiO_3$ transform into c domains, $PbTiO_3$ will be elongated along out-of-plane direction and shrinked in-plane as illustrated in fig.5.7c. However, it should lead to large elastic energy of internal stresses and thermodynamically unfavorable. In reality, this deformation is reduced due to formation of polydomain state consisting of *c*, a_1 and a_2 domains (fig.5.7e,f). A volume fraction of the *c*-domains in $PbTiO_3$ can be calculated from the experimental data in fig.5.3 by considering the strain compatibility conditions for a composite film:

$$\varepsilon_{33}^{CFO} = \varepsilon_{33}^{PTO} \tag{5.3}$$

$$\chi\varepsilon_{11}^{PTO} + (1-\chi)\varepsilon_{11}^{CFO} = \varepsilon_s \tag{5.4}$$

where $\varepsilon_{33}^{CFO} / \varepsilon_{11}^{CFO}$ and $\varepsilon_{33}^{PTO} / \varepsilon_{11}^{PTO}$ are the out-of-plane/in-plane total strains in the $CoFe_2O_4$ and $PbTiO_3$ phases respectively, ε_s describes a thermal contraction of the substrate, and χ is a volume fraction of $PbTiO_3$. The total strains in the *a*- and *c*-domains in $PbTiO_3$ (fig.5.6) can be calculated from the experimental values of $a_\perp$ and $a_\parallel$.

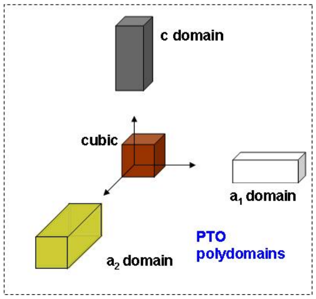
c domain
cubic
a1 domain
a2 domain
PTO polydomains

Figure 5.6 Schematics of $PbTiO_3$ domains. Cubic is the phase above transition temperature. After cooled down, it can be transformed into three types of stressed tetragonal domains denoted by grey (*c* domain), white (a_1 domain) and yellow (a_2 domain) bars.

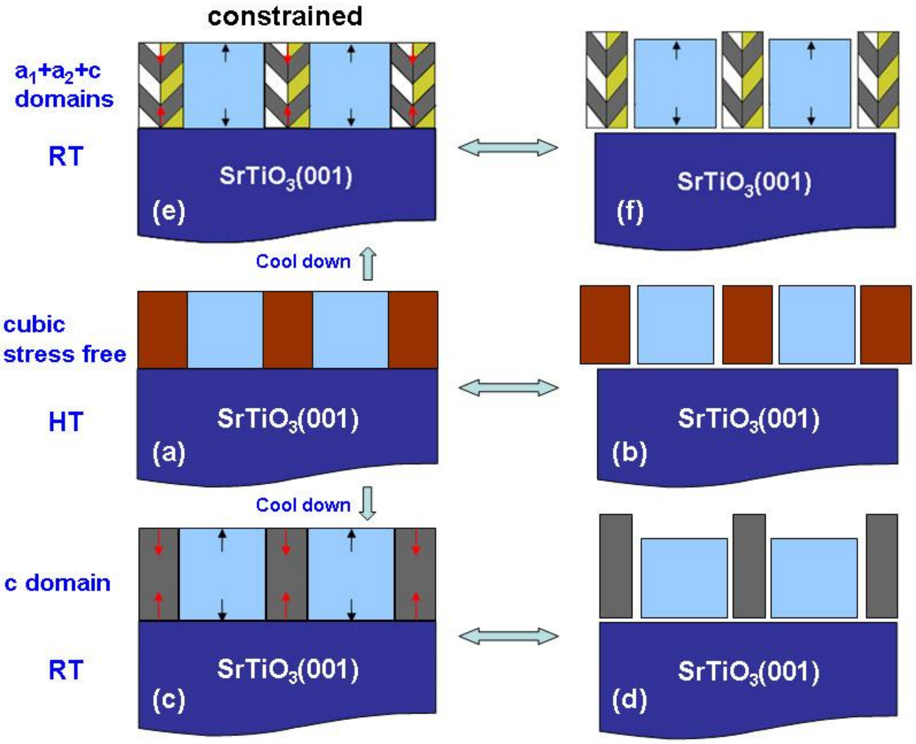
constrained
a1+a2+c domains
RT
SrTiO3(001)
(e)
(f)
Cool down
cubic stress free
HT
(a)
(b)
Cool down
c domain
RT
(c)
(d)

Figure 5.7 Schematic illustration of phase transformation of $PbTiO_3$ in self-assembled film on $SrTiO_3$ substrate. (1).constrained but stress-free state at high temperature (a),(b); (2).constrained state of pure *c* domain film at room temperature (c),(d); (3).constrained relaxed states of polydomain (a_1,a_2 and *c* domains) film at room temperature (e),(f).

Assume that in equilibrium all domains are distorted equally [73], their total strains are:

$$\hat{\varepsilon}_c = \begin{pmatrix} \varepsilon_a & 0 & 0 \\ 0 & \varepsilon_a & 0 \\ 0 & 0 & \varepsilon_c \end{pmatrix}; \quad \hat{\varepsilon}_a = \begin{pmatrix} \varepsilon_a & 0 & 0 \\ 0 & \varepsilon_c & 0 \\ 0 & 0 & \varepsilon_a \end{pmatrix}; \quad \hat{\varepsilon}_a = \begin{pmatrix} \varepsilon_c & 0 & 0 \\ 0 & \varepsilon_a & 0 \\ 0 & 0 & \varepsilon_a \end{pmatrix} \tag{5.5}$$

where $\varepsilon_c = (a_\perp - a_o)/a_o$, $\varepsilon_a = (a_\| - a_o)/a_o$ ($a_\perp$ and $a_{||}$ are experimental room temperature values of the $PbTiO_3$ lattice parameters; a_o is the lattice parameter of the cubic $PbTiO_3$ just above the transition). Taking into account that non-equivalent *a*-domains should have equal fractions, the total out-of-plane (ε_{33}^{PTO}) and in-plane (ε_{11}^{PTO}) strain components in polydomain PbTiO3 are as follows:

$$\varepsilon_{33}^{PTO} = \beta\varepsilon_c + (1-\beta)\varepsilon_a \tag{5.6}$$

$$\varepsilon_{11}^{PTO} = \varepsilon_{22}^{PTO} = \beta\varepsilon_a + \frac{(1-\beta)}{2}(\varepsilon_a + \varepsilon_c) \tag{5.7}$$

The volume fraction of the c-domains (β) is equal to:

$$\beta = (\varepsilon_{33}^{CFO} - \varepsilon_a)/(\varepsilon_c - \varepsilon_a) \tag{5.8}$$

The c-domain fractions calculated using experimental values of the lattice parameters (fig.5.3) are 0.61 and 0.51 for *x*=2/3 and *x*=1/3 respectively, which is in well agreement with the values estimated based on rocking curves. Substituting these values of β into the in-plane strain condition (equ.5.4) yields values of -0.002 (*x*=2/3) and -0.004 (*x*=1/3) which reflect a combination of the substrate contraction (ε_S~-0.006) and stress heterogeneities not accounted in β calculation using equ.5.8.

Comparing measured c/a results for *x*=1/3 and *x*=2/3, it is possible to find the stress-free strains: (stress-free here means without constraint, fig.5.7f) ε_a^0 and ε_c^0. The stress-free strains are connected to actual strains ε_a and ε_c in constrained film by the following mechanical relations:

$$\varepsilon_a = \varepsilon_a^0 + \hat{S}_a\hat{\sigma} \tag{5.9}$$

$$\varepsilon_c = \varepsilon_c^0 + \hat{S}_c\hat{\sigma} \tag{5.10}$$

$\hat{\sigma}$ is the elastic stress tensor in the ferroelectric phase; $\hat{S}_a$ and $\hat{S}_c$ are compliances in this phase corresponding to in-plane and out-of-plane strains.

With an assumption that ε_a^0 and ε_c^0 are the same for both film (i.e. solubility of Fe does not change with fraction of the phases), it can be suggested that stress in $Pb(Ti,Fe)O_3$ phase doubles when its volume fraction decreases by half. From condition of mechanical equilibrium in the two-phase film with internal stresses, follows that:

$$\varepsilon_a(x=2/3) = \varepsilon_a^0 + \hat{S}_a\hat{\sigma}\ ;\ \ \varepsilon_c(x=2/3) = \varepsilon_c^0 + \hat{S}_c\sigma \tag{5.11}$$

$$\varepsilon_a(x=1/3) = \varepsilon_a^0 + \hat{S}_a 2\hat{\sigma}\ ;\ \ \varepsilon_c(x=1/3) = \varepsilon_c^0 + \hat{S}_c 2\sigma \tag{5.12}$$

Then:

$$\varepsilon_a^0 = 2\varepsilon_a(x=2/3) - \varepsilon_a(x=1/3) \tag{5.13}$$

$$\varepsilon_c^0 = 2\varepsilon_c(x=2/3) - \varepsilon_c(x=1/3) \tag{5.14}$$

As ε_c and ε_a are known from experimental data in fig.5.3, we can calculate a^o and c^o lattices (a^o and c^o are lattice parameters of stress-free *c*-domain) and find the stress-free *c/a*=1.03~1.035. Taking into account the difference of elastic properties of the phases, it is possible to show that this ratio approaches 1.04 in good agreement with the estimates of c/a value based on composition dependence of T_c. Compared to the bulk *c/a*=1.064 value, the dissolution of Fe in $PbTiO_3$ results in about 40% reduction of $PbTiO_3$ tetragonal distortion.

5.4 Conclusion

Overall, the estimates based on the strain compatibility conditions along with the integrated intensity measurements using $002_{PTO}/200_{PTO}$ rocking curves support presence of significant fractions of both *c*- and *a*-domains in $PbTiO_3$, despite a nonoscale of the composite heterstructures. Small domain size contributes to a broadening of the $PbTiO_3$ reflections. A significant fraction of *a*-domains which dilute the net out-of-plane polarization in $PbTiO_3$ is expected to reduce the strength of electromagnetic (EH) coupling compared to the theoretical estimates made for a single-domain $PbTiO_3$.

The observation of Fe dissolution is expected to further decrease the tetragonal distortion in addition to effects from existence of *a*-domains. Thus, the intrinsic piezoresponse of the ferroelectric component of the film should dramatically decrease (more than twice in our case) even without any constraints. The relatively large value of d_{33} measured on the film with electrodes (~50 while bulk value 79pm/V [52]) allows us to speculate that this is an extrinsic effect due to domain wall movements. However, the effect of these domains on the magnitude of magnetoelectric (ME) coupling will depend on the mobility of domain walls which requires further investigation. In principle, the effect of magnetic field on polarization can be enhanced while the effect of electrical field on magnetization can be reduced providing the domain walls are sufficiently mobile. Clearly, the optimal choice of a ferroelectric component for a given nanostructure architecture should take into account a relief mechanism for the transformation stresses.

Chapter 6 Piezoelectric Properties of Nano-$PbTiO_3$ Ferroelectrics Embedded in Ferromagnetic Film

6.1 Introduction

Fundamental understanding of a ferroelectric response in nanostructured materials is critical for their implementation in practical devices. Recently, numerous theoretical studies of polarization behavior in ferroelectric nanoparticles have been reported [74,75,76]; however, experimental verification of the proposed models and hypotheses is hindered by the lack of suitable samples and difficulties with nanoscale ferroelectric measurements. Epitaxial self-assembly of lattice-matched phases on matching single crystal substrates provides a viable approach for generating nanoscale ferroelectric features embedded into a non-ferroelectric matrix. This approach has been successfully applied to the growth of transversely modulated multiferroic nanostructures consisting of ferroelectric perovskite and ferromagnetic spinel phases on single crystal substrates [10,77,78,79]. The morphology of constituent phases in these self-assembled nanostructures can be effectively controlled using substrate orientation and phase fractions. For perovskite-spinel systems, nanorods of perovskite phase in a spinel matrix were obtained for the $PbTiO_3$-$CoFe_2O_4$ on (110) and (111) $SrTiO_3$ substrate and for $BiFeO_3$-$CoFe_2O_4$ on (111) $SrTiO_3$.

Several studies examined a ferroelectric response of the (111)-oriented $BiFeO_3$-$CoFe_2O_4$ films containing $BiFeO_3$ nanorods in a $CoFe_2O_4$ matrix. Ferroelectric nature of individual $BiFeO_3$ columns has been confirmed using piezoelectric force microscopy (PFM) [22]. The direction of spontaneous polarization in rhombohedral $BiFeO_3$ coincides with the nanorods axes thereby facilitating both piezoelectric and ferroelectric responses. The situation is significantly different for tetragonal perovskite-like phase, such as $BaTiO_3$ and $PbTiO_3$, because, in the (110)- and (111)- oriented composite films, the (001) direction of spontaneous polarization is strongly inclined to perovskite/spinel interfaces. No analyses of a ferroelectric behavior in this kind of nanostructures have yet been reported. In the present study, we used both conventional piezoelectric force microscopy (PFM) and switching spectroscopy PFM (SS-PFM) to analyze a piezoelectric response of the $PbTiO_3$ nanocolumns in $1/3PbTiO_3$-$2/3CoFe_2O_4$ self-assembled nanostructures on both (110)- and (111)-oriented $SrTiO_3$ substrates [14,26]. SS-PFM enables local piezoelectric measurements without electrodes thereby alleviating electrical leakage problems associated with the $CoFe_2O_4$ matrix; this leakage complicates direct measurements of a ferroelectric response in nanostructures having $CoFe_2O_4$ as a majority phase [52,80].

6.2 Measurement techniques

6.2.1 Conventional PFM Qualitative Measurement

Piezoresponse force microscopy (PFM) is based on the detection of local piezoelectric response of a piezo- or ferroelectric material induced by an external electric field. Taking advantage of the electromechanical coupling at the tip-surface junction for imaging polarized regions was originally introduced by Guthner et al. in 1992 [81]. With the rapid development of electronic devices based on ferroelectric thin films during the most recent decade, PFM nowadays is the most popular technique among the scanning probe microscopy (SPM) techniques for characterization of nanoscale ferroelectrics [82,83,84,85].

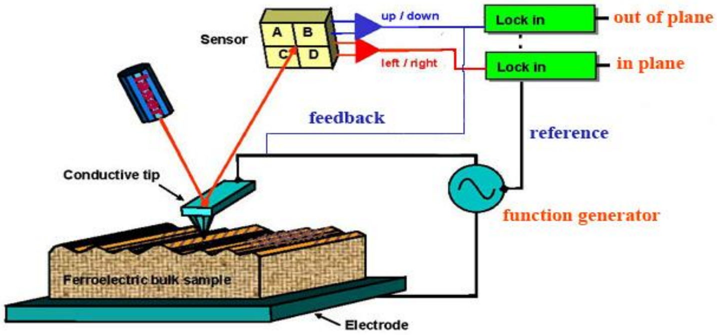
Sensor
A
B
C
D
up / down
left / right
Lock in
out of plane
Lock in
in plane
feedback
reference
Conductive tip
function generator
Ferroelectric bulk sample
Electrode

Figure 6.1 Standard PFM setup for vertical and lateral piezoresponse acquisition.

The standard experimental PFM setup is based on a commercial SPM equipped with a conductive probe, a four-quadrant photo detector, a function generator and two lock-in amplifiers as illustrated in figure 6.1. Sample is placed between the bottom electrode and the conductive tip (sometimes with top electrode on the film as well). An ac voltage between the tip and the bottom electrode is applied by the function generator. During PFM measurement, the tip is brought into contact with the surface. The voltage-induced cantilever deflection is detected by a reflected laser beam on a four quadrant photodiode. Tip deflection A and the periodic external bias V_{tip} to the tip are described as [83,84,85]:

$$A=A_0+A_{1\omega}\cos(\omega t+\varphi), \tag{6.1}$$

$$V_{tip}=V_{dc}+V_{ac}\cos(\omega t) \tag{6.2}$$

The first harmonic component in equation 6.1, $A_{1\omega}$, is the piezoelectric response of the surface under bias V_{tip}. The phase of the electromechanical response of the surface, φ, with respect to the phase of the ac voltage, yields information on the domain directions.

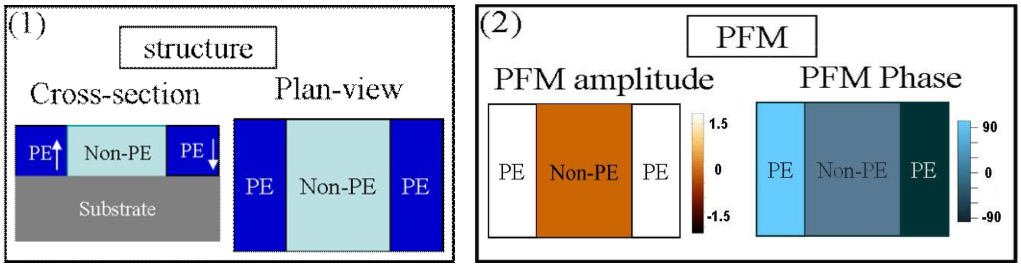
(1)
structure
Cross-section
Plan-view
PE
Non-PE
PE
Substrate
PE
Non-PE
PE
(2)
PFM
PFM amplitude
PFM Phase
PE
Non-PE
PE
1.5
0
-1.5
PE
Non-PE
PE
90
0
-90

Figure 6.2 (1) Schematics of a structure consisting of two piezoelectric domains with opposite orientations separated by a non-piezoelectric stripe. (2) Schematics of expected PFM amplitude and phase images.

As schematically illustrated in fig.6.2, piezoelectric domains (fig.6.2(1)) can be distinguished from non-piezoelectric materials by different values of piezoresponse. Strong piezoresponse is expected from piezoelectric stripes (colored as white in fig.6.2(2)) and no piezoresponse from the non-piezoelectric materials (orange stripe in fig.6.2(2)). Piezoelectric domains with different orientations can be identified by PFM phase images. For example, ideally, two piezoelectric stripes with opposite orientations (fig.6.2(1)) should have same numerical piezoresponse as schematically demonstrated in the PFM amplitude image (fig.6.2(2), left side), however, their opposite domain orientations can be identified for having 180^{o} difference in the phase image (fig.6.2(2)).

6.2.2 Quantitative Hysteresis Loop Acquisition

Formation of domains is very common in ferroelectric materials as it helps minimize system energy. These domains can be identified qualitatively using PFM. However, qualitative characterization is not enough to understand ferroelectric materials properties. A hystereis loop is essential as it contains important information, such as spontaneous polarization, saturated polarization and coercive field.

Hysteresis loop measurement using modified Sawyer-Tower circuit

Hsteresis loop measurement was usually carried out using a modified Sawyer-Tower circuit as illustrated in Figure 6.3 (a) [86,87].

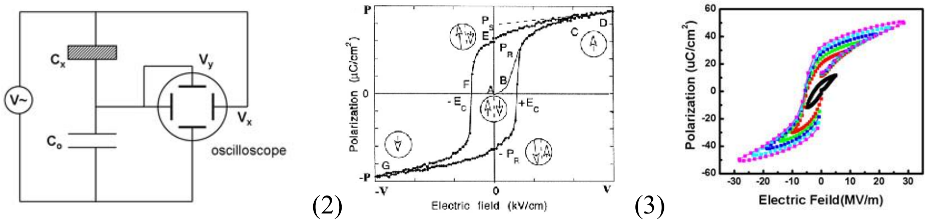
V~
C_x
V_y
V_x
C_o
oscilloscope
P
-P
-V
V
Polarization (μC/cm^2)
Electric field (kV/cm)
P_S
E
P_R
C
D
B
A
F
$-E_C$
$+E_C$
$-P_R$
G
0
Polarization (uC/cm^2)
Electric Feild(MV/m)
60
40
20
0
-20
-40
-60
-30
-20
-10
0
10
20
30

(1) (2) (3)

Figure 6.3 (1) Schematics of modified Sawyer-Tower circuit. (2) Schematic illustration of ferroelectric polarization hysteresis loop (P-E loop). (3) Experimental polarization hysteresis loops of 2/3$PbTiO_3$-1/3$CoFe_2O_4$ thin film on (100) $SrTiO_3$ substrate [52].

The voltage lying across the crystal C_x is applied on the horizontal plates of the oscilloscope, thus plotting on the horizontal axis a quantity which is proportional to the field on the crystal. The linear capacitor C_o is connected in series with the crystal C_x. Voltage across C_o is therefore proportional to the polarization of the crystal C_x.

This voltage is laid across the vertical plates of the oscilloscope.

The voltage V_y, across the vertical deflection plates of the oscilloscope is given by [88]:

$$V_y = \frac{1}{C_o}\int I dt = \frac{1}{C_o}\int \frac{dQ_x}{dt} dt = \frac{Q_x}{C_o} \tag{6.3}$$

The charges Q_x on the crystal electrodes is given in SI units by

$$Q_x = AD = A(\varepsilon_0 E + P) = A(\varepsilon_0 E + \chi\varepsilon_0 E + P_f) = A(\varepsilon\varepsilon_0 E + P_f) \tag{6.4}$$

So, $$V_y = \frac{Q_x}{C_o} = \frac{A}{C_o}(\varepsilon\varepsilon_o E + P_f) = \frac{A}{C_o}(\varepsilon\varepsilon_o \frac{V_x}{d} + P_f) \tag{6.5}$$

Here A is the electrode area, D is the electric displacement; χ and ε are the electric susceptibility and dielectric constant respectively. P_f is the nonlinear part of the polarization associated with the ferroelectric behavior. d is the thickness of ferroelectric material.

Hysteresis loop is thus obtained by measuring switch charge Q_x and polarization in figure 6.3(2) is calculated based on equation 6.4. Under an external electric field, the polarization increases linearly with the field amplitude, according to P-E relation: $P = \chi\varepsilon_o E$. This corresponds to segment AB in figure 6.3(2). The field is not strong enough to switch domains with the unfavorable direction of polarization in this region. As the field is increased the polarization of domains with an unfavorable direction starts to switch in the direction of the field and the measured charge density is increased rapidly (segment *BC*). The polarization response in this region is strongly nonlinear and equation $P = \chi\varepsilon_o E$ is no longer valid. Once all the domains are aligned (point *C*) the ferroelectricity again behaves linearly (segment *CD*). Point *C* on figure 6.3(2) represents time at which P_f has reached its maximum and its value (P_s) is determined by extrapolating line *CD* back to zero applied field as indicated on figure 6.3(2). If the field strength starts to decrease, at zero field the polarization is nonzero (point *E*); only part of the domains will back-switch due to domain pinning effects. To reach a zero polarization state the field must be reversed (point *F*). Further increase of the field in the negative direction will cause a new alignment of dipoles and saturation (point *G*). The field strength is then reduced to zero and reversed to complete the cycle. The value of polarization at zero field (point *E*) is called the remnant polarization, P_R. The field necessary to bring the polarization to zero is called the coercive field, E_C.

Hysteresis loop obtained experimentally sometimes will have some deviation from the ideal loop demonstrated in fig.6.3(2). Curves in fig.6.3(3) are hysteresis loops of 2/3PbTiO3-1/3CoFe2O4 thin film on (100) SrTiO3 with top and bottom electrodes [52]. Because of leakage caused by $CoFe_2O_4$, those curves are not closed.

Hysteresis loop measurement using PFM technique

Hysteresis loop measurement using PFM is different from technique using modified Sawyer-Tower circuit. Fundamentally, PFM base technique detects surface displacement rather than charge. Displacement loop instead of P-E loop is obtained as a direct result from the measurement. However, P-E loop can be transformed from displacement loop as there is a linear relation between piezoelectric coefficient d_{zz} and the polarization [89]:

$$d_{zz} = \varepsilon_{zz} Q_{zz} P(E)/2\pi \quad (6.6)$$

Here ε_{zz} is the dielectric constant in normal direction to the film and Q_{zz} is the electrostrictive coefficient, *P(E)* is the polarization at field E. And displacement (*S*) is:

$$S = d_{zz} * E * d \quad (6.7)$$

d is the thickness of the film.

During the hysteresis loop acquisition using PFM, a dc field plus an ac field are applied to the sample as expressed in equation 6.2 and usually measurement is carried out with both top and bottom electrodes. The dc bias with a waveform illustrated in figure 6.4 is supplied as polarizing voltage and is increased in steps from –V to +V and then decreased from +V to –V with the same step size. At each step, the dc voltage is set to zero prior to imaging.

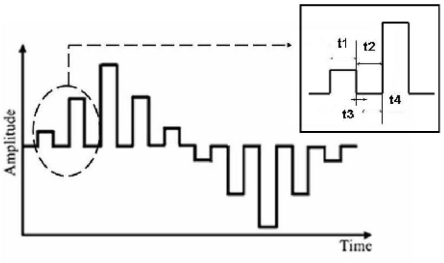

Figure 6.4 Schematics of dc bias waveform. t1 is the writing period and t4 is the reading period. t3 is a waiting interval.

Sample is polarized by the external dc bias in t1 time period (fig.6.4). Both amplitude and phase data are collected during the reading time period t4 after dc bias has been turned off for t3 time period. The amplitude and phase data are described by equation 6.1. Usually, the amplitude as a function of dc bias has a butterfly shape for ferroelectric material as illustrated in figure 6.5(1). Ideally, it is symmetric (the inset shows an ideal shape of the amplitude curve) with respect to the *y* axis because before and after switching, the ideal ferroelectric material should have the same magnitude of displacement under the same value of dc bias. In reality, the observed d_{zz} loop is asymmetric due to defects, domain wall movement and non-180^o domains involvement etc. [90]. The phase loop in figure 6.5(2) gives information on domain orientations. Both amplitude and phase information are integrated into a single piezoresponse hysteresis loop (PR-E) as shown in fig.6.5(3). The absolute value in fig.6.5(3) denotes the piezoresonse amplitude and the positive/negative sign of the piezoresponse denote domain orientations. For example, in fig.6.5(3), domains under -20V external bias have the same magnitude of piezorepsonse as domains under +20V external bias. However, domains under -20V external bias has the opposite orientation as domains under +20V external bias.

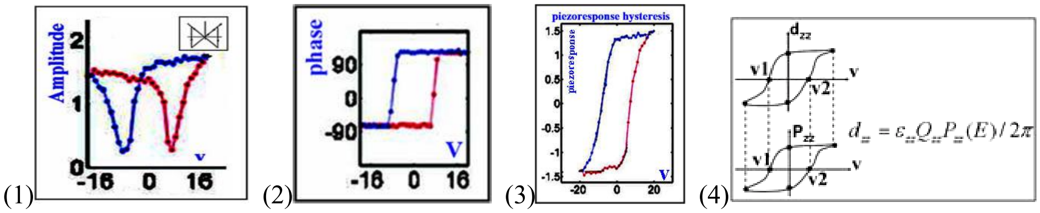

Figure 6.5 (1) Illustration of butterfly amplitude loop. (2) Illustration of phase loop. (3) Piezoresponse (piezoelectric) hysteresis loop generated based on amplitude and phase data in (1) and (2). (4) Schematics of transforming d_{zz} piezoresponse hysteresis loop to polarization hysteresis loop.

Polarization hysteresis loop (P-E) can be obtained by transforming piezoresponse hysteresis loop (PR-E) into P-E loop accoding to equation 6.5 and 6.6. The relative relationship between the PR-E loop and P-E loop is illustrated in fig 6.5(4). Coercive field for both PR-E loop and P-E loop is the same and the field at saturated point for both loops is the same as well.

6.2.3 Switching Spectroscopy piezoresponse force microscopy

Switching spectroscopy piezoresponse force microscopy (SS-PFM) is a novel technique based on PFM and is developed to quantitatively address local properties of ferroelectrics [26].

A typical SS-PFM setup is illustrated in figure 6.6. A specific custom-built shielded sample holder is used to allow direct tip biasing and to avoid capacitive crosstalk. For conducting purpose, measurement is performed using metal coated tips. Two function generators and a summation amplifier are adopted to superimpose the PFM imaging voltage $V_1(\omega_1)$ to the triangle switching voltage V_2. V_2 with a waveform schematically illustrated in fig.6.4 is supplied as a polarizing bias and V_1 is supplied as an imaging voltage. The oscillation of the sample under V1 ac voltage will be transferred to the cantilever and sensed by the sensor. The output is further sent to the lock-in amplifier and only signal with the same frequency as the ac driving voltage will be locked and amplified. Depending on whether vertical PFM signal or lateral PFM signal is interested, different ac driving frequencies are selected. Vertical PFM measurement is usually performed with frequency ranging from 20KHz to

2MHz and lateral PFM measurement is normally conducted with a frequency around 10KHz.

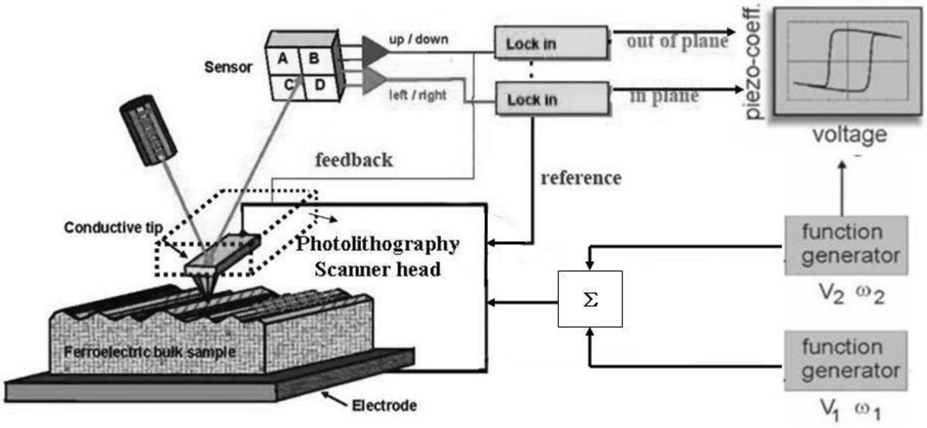
Sensor
A
B
C
D
up / down
left / right
Lock in
Lock in
out of plane
in plane
piezo-coeff.
voltage
feedback
reference
Conductive tip
Photolithography Scanner head
Ferroelectric bulk sample
Electrode
Σ
function generator
V2 ω2
function generator
V1 ω1

Figure 6.6 Typical SS-PFM setup including two function generators, a summation amplifier (Σ) two lock-in amplifiers and a photolithography scanner head.

One of the major hardware differences between PFM and SS-PFM is the extra photolithography scanner head in SS-PFM. Customized Matlab/LabView software is used to generate a scanning pathway illustrated as a grid shown in fig.6.7(1). The grid covers the interested area on the sample. The photolithography scanner head allows tip to trace the grid point by point and acquire hysteresis loop at each intersected point on the grid. Thus an X by Y local data map with spacing f between two neighboring points is obtained.

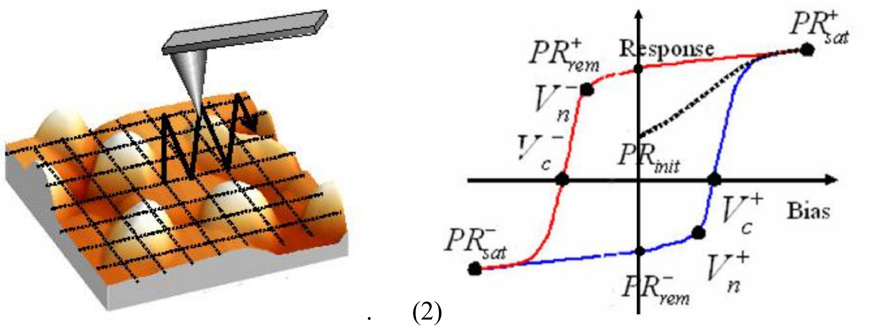

(1) . (2)

Figure 6.7 (1) Illustration of a pathway grid used in SS-PFM measurement. Data will be collected at each of the intersection. (2) Illustration of a piezoelectric hysteresis loop from one single point at the intersection.

A schematic local piezoelectric hysteresis loop is shown in fig.6.7(2). It contains two piezoresponse (PR) branches: forward piezoresponse ($PR^+(V)$) and reverse piezoresponse ($PR^-(V)$) respectively. Neglecting other contributions to the Piezoresponse loop, the corresponding voltages for zero $PR^+(V)$ and $PR^-(V)$ are coercive voltage V_c^+ and V_c^- respectively. PR^+_{rem} and PR^-_{rem} in the figure are positive and negative remnant response. PR^+_{sat} and PR^-_{sat} defines the saturation response and $PR_s = PR^+_{sat} - PR^-_{sat}$ is the maximal switchable response. The bias at the crossover between constant and rapidly changing regions of the loop are defined as domain nucleation voltages shown in fig.6.7(2) as V_n^+ and V_n^-. The SS-PFM measurement finally yields a real-space 3D data array of imprint, coercive bias, nucleation bias, work of switching, electromechanical activity and other dynamics characteristics of switching [26].

Traditional ferroelectric hysteresis loop measurement usually requires top and bottom electrodes. However, $CoFe_2O_4$ will cause devastating leakage to the piezoelectric measurement with electrodes [80]. As SS-PFM is capable of performing local piezoresponse measurement without electrodes, it is chosen for our study.

6.3 Experimental Results obtained by SS-PFM

1/3$PbTiO_3$-2/3$CoFe_2O_4$ films were grown on differently oriented $SrTiO_3$ substrates using pulsed laser deposition and a composite ceramic target as described previously. In all cases, film thicknesses were about 50nm. $PbTiO_3$ and $CoFe_2O_4$ self-assembled during growth into epitaxial nanostructures having $PbTiO_3$/$CoFe_2O_4$ interface approximately perpendicular to the film/substrate interface. Films grown on (001) $SrTiO_3$ contain $CoFe_2O_4$ pillars surrounded by a continuous $PbTiO_3$ matrix. In contrast, nanostructures grown on (110) and (111) $SrTiO_3$ contain nanocolumns of PbTiO3 distributed in $CoFe_2O_4$. X-ray diffraction, scanning (SEM) and transmission (TEM) electron microscopy were used to assess the crystalline quality and phase morphologies as discussed in previous chapters.

The SS-PFM (Asylum MFP3D) was implemented using a commercial atomic force microscope equipped with additional function generator, lock-in amplifier (DS 345 and SRS 830, Stanford Research Instruments), photolithography scanning head and data acquisition system. Measurements were performed using Micromasch Au-Cr coated Si tips having a spring constant of 3N/m. During the acquisition process, the tip was biased using electrical voltage V_{tip} and the electromechanical response of the surface was detected as the first harmonic component ($A_{1\omega}$) of bias-induced tip deflection described by equ.6.1. The measurements were conducted using a step (pixel) size of 6 nm. At each point, a piezoelectric response was recorded as a function of the tip bias.

6.3.1 SS-PFM Results for (110) Oriented Thin Film

Fig.6.8(2) is a real-space SS-PFM map of piezoresponse. Domains of different piezoresponse magnitude and orientations can be identified using the scale bar. $PbTiO_3$ platelets distributed in $CoFe_2O_4$ is observed and schematically illustrated in fig.6.8(3). The morphology given by SS-PFM is similar to what observed by SEM (fig.6.8(1)). The observation from conventional PFM amplitude image (fig.6.8(4)) and phase image (fig.6.8(5)) is also in good agreement with results from SEM (fig.6.8(1)) and SS-PFM (fig.6.8(2)).

Piezoelectric loops are collected at each small step pixel in the SS-PFM map (fig.6.8(2)). Individual piezoresponse and phase loops from points marked 1 to 4 in fig.6.8(2) are demonstrated in fig.6.9. Only generated piezoresponse hysteresis loops for points 1,2 and 4 are demonstrated. Separated piezoresponse amplitude and phase loops in addition to the generated piezoreposne hysteresis loop are demonstrated for point 3.

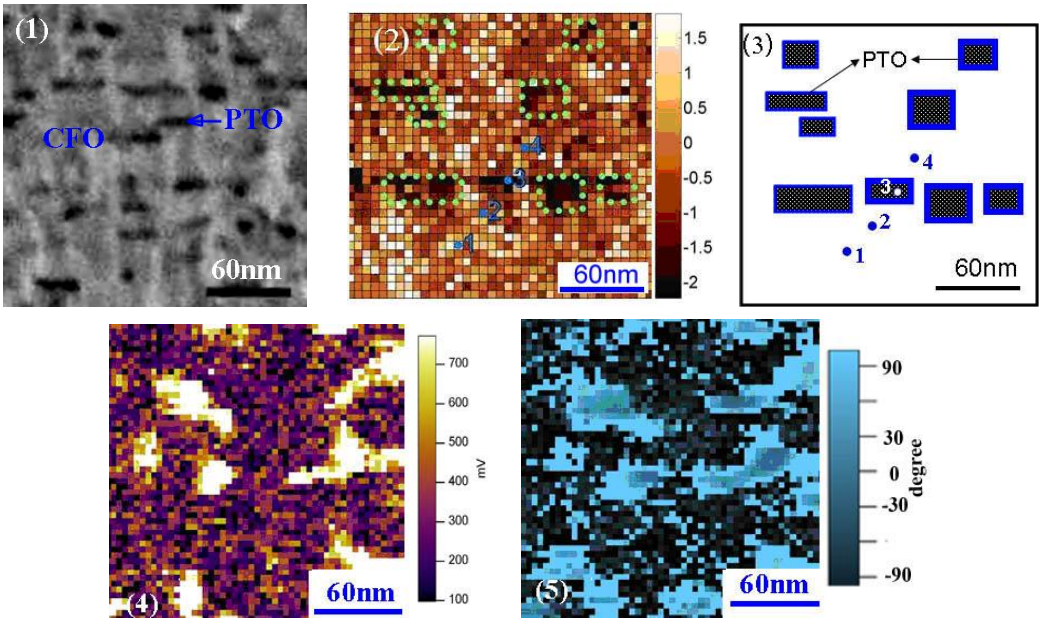
(1)
CFO
PTO
60nm
(2)
4
3
2
1
60nm
1.5
1
0.5
0
-0.5
-1
-1.5
-2
(3)
PTO
4
3
2
1
60nm
(4)
60nm
700
600
500
400
300
200
100
mV
(5)
60nm
90
30
0
-30
-90
degree

Figure 6.8 1/3PbTiO$_3$-2/3CoFe$_2$O$_4$ (110) oriented film (1) SEM Topography image. The dark-grey platelets with width of ~15nm are PbTiO$_3$ (PTO) and the rest is CoFe$_2$O$_4$ (CFO) matrix. (2) SS-PFM map of piezoresponse (3) schematics of the PbTiO$_3$ platelets identified based on the SS-PFM image. (4) Conventional PFM amplitude image (5) Conventional PFM phase image coupled with (4).

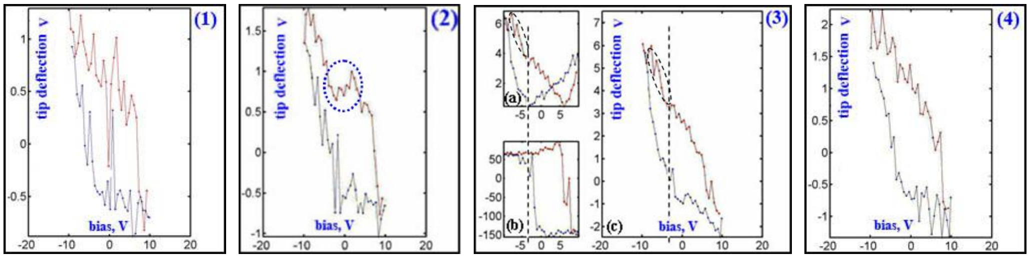

Figure 6.9 Piezoelectric hysteresis loops and calculated piezoresponse. (1),(2),(4) are piezoelectric hysteresis loops at point 1,2 and 4. (3a) Amplitude curve at point 3. (3b) Phase curve at point 3. (3c) Piezoelectric hysteresis loop at point 3.

6.3.2 SS-PFM Results for (111) Oriented Thin Film

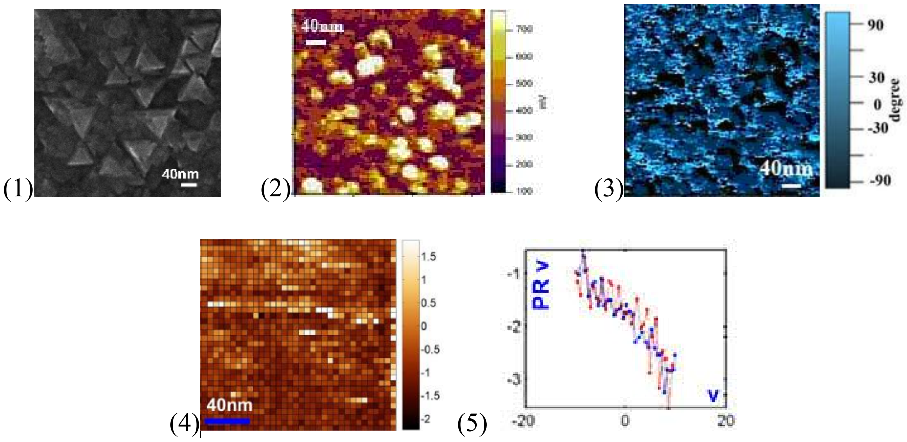

Figure 6.10 (111) oriented 1/3$PbTiO_3$-2/3$CoFe_2O_4$ thin film on $SrTiO_3$(111) substrate. (1) SEM topography image. (2) Amplitude image from PFM measurement. (3) Phase image from PFM measurement. (4) SS-PFM map (5) One typical piezoelectric loop with relatively strong piezoreponse from SS-PFM measurement.

Piezoelectric properties of (111) oriented 1/3PbTiO3-2/3CoFe2O4 film with a PbTiO3 nanorods embedded in CoFe2O4 matrix (fig.6.10(1)) is investigated using both PFM and SS-PFM. Bright spots in the conventional PFM amplitude image (fig.6.10(2)) shows clear piezoresponse and the PFM phase image (fig.6.10(3)) shows different phase of these bright spots from the surrounding material. The bright sports in fig.6.10(2) must be $PbTiO_3$ phase as $CoFe_2O_4$ is non-piezoelectric materials, which is in agreement with SEM observation (fig.6.10(1)) regarding the size and density of $PbTiO_3$ phase. Qualitatively, the conventional PFM images demonstrate that confined (111) $PbTiO_3$ phase is piezoelectrics. However, isolated $PbTiO_3$ structures can not be identified in the SS-PFM map (fig.6.10(4)). Fig.6.10(5) is a typical piezoresponse loop from a cell among those having relatively strong piezoresponse in SS-PFM map. Quantitatively, the piezoresponse of (111) oriented $PbTiO_3$ (fig.6.10(5)) is about half of the value from (110) oriented $PbTiO_3$ (fig.6.9(3)).

6.3.3 SS-PFM Results for (001) Oriented Thin Film

For comparison and system calibration purpose, SS-PFM measurement on (001) $1/3PbTiO_3$-$2/3CoFe_2O_4$ is carried out as well.

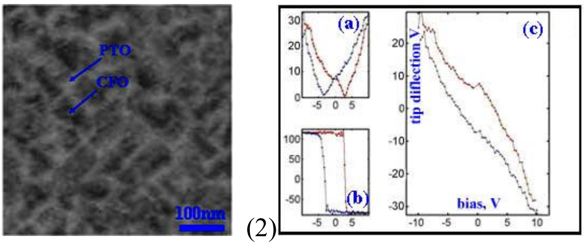

(1) (2)

Figure 6.11. (100) oriented film of composition $1/3PbTiO_3$-$2/3CoFe_2O_4$. (1) SEM topography. (2) SS-PFM results including (a) amplitude curve, (b) phase curve and (c) generated piezoelectric hysteresis loop.

6.3.4 Lateral Piezoresponse

10K Hz ac frequency is used for the lateral piezoresonse measurement in order to minimize the resonant effects and enable the transduction of the lateral surface vibrations to the tip. (110) oriented film does not give clear lateral piezoresponse (fig.6.12(1) and fig.6.12(2)) while for (111) oriented film, isolated piezoelectric domains are observed in the lateral piezoresponse measurement (fig.6.12(3) and fig.6.12(4)). Domain sizes in fig.6.12(3) and (4) is similar to what observed in SEM image (fig.6.10(1)).

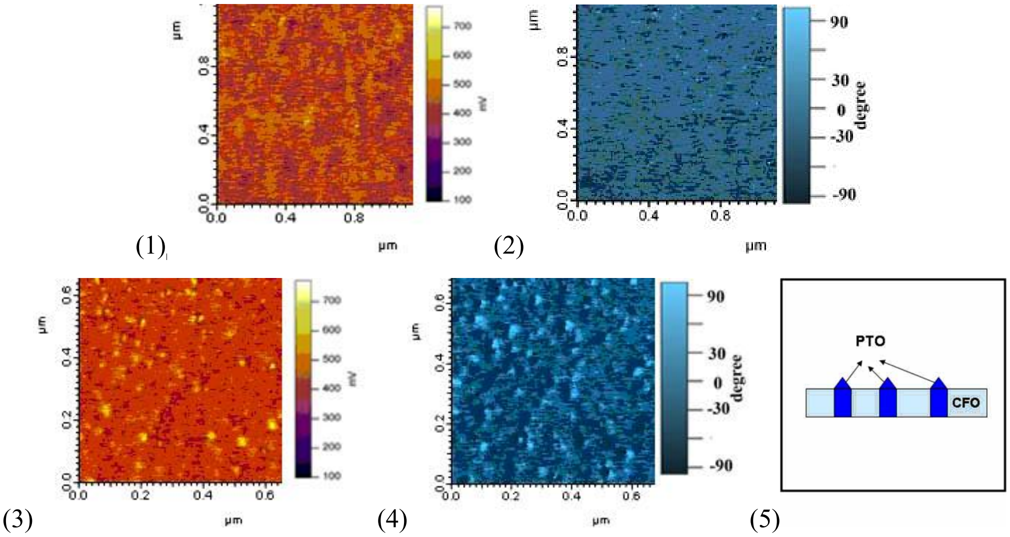
(1) (2) (3) (4) (5)

Figure 6.12 PFM lateral piezoresponse. (1) and (2) are amplitude and phase image respectively for (110) oriented 1/3$PbTiO_3$-2/3$CoFe_2O_4$ film. (3) and (4) are amplitude and phase image respectively for (111) 1/3$PbTiO_3$-2/3$CoFe_2O_4$ oriented film. Both (111) and (110) oriented film are measured under the same experimental conditions. (5) Schematics of intruded $PbTiO_3$ nanorods out of the $CoFe_2O_4$ matrix for the (111) oriented film.

6.4 Discussion

Semi-quantitatively theoretical calculation of piezoresponse for (110) $PbTiO_3$ is performed. Under circumstance of SS-PFM measurement, there is neither top nor bottom electrode and the tip serves as a moving top electrode while the sample holder serves as bottom electrode. The electrical field distribution under this geometry is inhomogeneous and needs to be considered in the semi-quantitative calculation.

For transversely isotropic material, the electrical field structure for spherical tip geometry can be solved using image charge method. In this method, the tip geometry is represented by an isopotential voltage contour expressed as [83,91,92]

$$V_Q(\rho,z)=\frac{1}{2\pi\varepsilon_0(\varepsilon_e+\kappa)}\sum_{m=0}^{\infty}\frac{Q_m}{\sqrt{\rho^2+(z/\gamma+d_m)^2}} \tag{6.8}$$

Where $\rho=\sqrt{x_1^2+x_2^2}$ is radial coordinate and z are vertical coordinate (figure 6.13a).

ε_e: dielectric constant of the ambient;

$\kappa=\sqrt{\varepsilon_{33}\varepsilon_{11}}$: effective dielectric constant of the material;

$\gamma=\sqrt{\varepsilon_{33}/\varepsilon_{11}}$: dielectric anisotropy factor;

-d_m: *z* coordinate of the point charge Q_m.

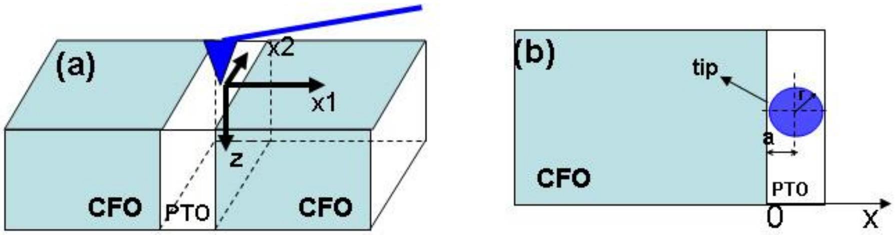

Figure 6.13(a) Tip coordinate system (x_1,x_2,z). (b) 2D projection from the top. *r* is the tip radius, a is the *x* coordinate of the tip center. 0 point of *x* axis is at the interface of $CoFe_2O_4/PbTiO_3$.

Q_m named image charge can be expressed as

$$Q_{m+1}=Q_m(\kappa-\varepsilon_e)r/[(\kappa+\varepsilon_e)(r+\Delta R+d_m)] \tag{6.9}$$

and $d_{m+1}=r+\Delta R-r^2/(r+\Delta R+d_m)$

where, $Q_0=4\pi\varepsilon_0\varepsilon_e rU$, $d_0=r+\Delta R$, U is the tip bias, *r*: tip radius

ΔR: distance between the tip and the sample surface

The inhomogeneous electrical field distribution can thus be solved by replacing the tip geometry with a charge contour described by equation 6.7. However, the above method is quite complicated practically. There is an alternative simpler approach to solve the inhomogeneous electrical field distribution issue, which names effective point charge model [91]. In the effective point charge model, the tip is represented by a single charge described as

$$Q = 2\pi\varepsilon_0\varepsilon_e rU(\kappa + \varepsilon_e)/\kappa \tag{6.10}$$

The single charge Q is located at: $d = \varepsilon_e r/\kappa$

For simplicity reason, effective point charge model is adopted in the following calculation. For (110) $PbTiO_3$ ferroelectric platelet with γ=0.6 embedded in a nonferroelectric media, the vertical piezoresponse $PR_v(a,r)$ under the bias can be calculated as [92]:

$$PR_V(a,r) \approx C_{(110)}\left[\frac{Qg(a,\gamma,\nu)}{2\pi\varepsilon_0(1+\kappa)d}(d_{31}f_1(\gamma) + d_{15}f_2(\gamma) + d_{33}f_3(\gamma))\right] \tag{6.11}$$

$$f_1(\gamma) = \frac{1+2(1+\gamma)\nu}{(1+\gamma)^2}$$

$$f_2(\gamma) = \frac{\gamma^2}{(1+\gamma)^2}$$

$$f_3(\gamma) = \frac{1+2\gamma}{(1+2\gamma)^2}$$

were $C_{(110)}$ is a coefficient which converse piezoreponse along (001) orientation into piezoresponse along (110) orientation [93]. Function g(a,r,υ) represents tip position with respect to the $PbTiO_3$ platelet as illustrated in figure 6.12(b) and can be expressed as [92]:

$$g(a,r,v) \approx \begin{cases} \pi r^2 - [ArcCos(\frac{a}{r}) \cdot r^2 - a \cdot \sqrt{r^2 - a^2}] - [ArcCos(\frac{L-a}{r}) \cdot r^2 - (L-a) \cdot \sqrt{r^2 - (L-a)^2}], & \mathrm{L}/2 > a \geq 0 \\ r^2 \cdot ArcCos[\frac{-a}{r}] - a \cdot \sqrt{r^2 - a^2}, & -r \leq a < 0 \\ 0, & a < -r \end{cases} \tag{6.12}$$

where L (~15nm) is the average width of (110) $PbTiO_3$ platelets. *r* (~30nm) is the tip radius.

Normalized theoretical piezoresponse for (110) oriented sample as the tip scans along *x* axis (fig.6.13b) is demonstrated in fig.6.14(2). The blue round dots labeled 1 to 4 are normalized experimental piezoresponse at points 1 to 4 marked in fig.6.8(2) and the tip positions at these 4 points are illustrated in fig.6.14(2). As shown in fig.6.14(1), the normalized experimental values fit the theoretical piezoresponse curve very well except point 1 because the electrostatic noise is not considered in the calculation. At point 1, tip locates mainly on $CoFe_2O_4$ with very weak contact on the edge of $PbTiO_3$ as shown in fig.6.14(2). Electrostatic response is strong in this scenario which results a deviation of the experimental value from the theoretical curve. At point 2, the experimental value fits the curve very well, however, there is a

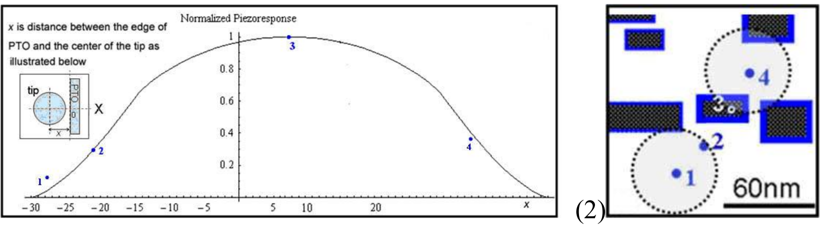

(1) (2)

Figure 6.14 (1) Normalized calculated piezoresponse as a function of tip position and experimental results (points 1 to 4). (2) Illustration of tip position with respect to $PbTiO_3$ nanoplatelets.

shoulder in the hysteresis loop (circled area in fig.6.9(2)). Existence of the shoulder is believed due to unstable domain switching during the loop acquisition cycle. At this location, tip still touches the $PbTiO_3$ platelet on the edge as shown in fig.6.14(2) which causes the unstable domain switching. Tip covers the $PbTiO_3$ in full width when it moves to point 3. The most strong piezoresponse out of the four points is observed at this position (fig.6.9(3)). Though piezoresponse is the strongest at point 3, saturated piezoresponse is not observed. When tip moves to point 4, the piezoresponse behaves similar to that at point 2 as tip again only touches $PbTiO_3$ platelet on edge at point 4. Unambiguous domain switching is observed at point 2,3 and 4, especially at point 3 as shown in fig.6.9(3).

For (111) oriented sample, domain switching is not observed. The SS-PFM measurement shows the forward branch and reverse branch of the piezoresponse loop overlap with each other (fig.6.10(5)). As the PFM measurement (fig.6.10(2) and fig.6.10(3)) proves that the (111) $PbTiO_3$ nanorods are piezoelecrics, the hysteresis loop in fig.6.10(5) must be a part of a hysteresis loop. Curve showing domain switching features is not observed only because 10V maximum applied bias is not enough to switch the (111) oriented confined $PbTiO_3$ domains.

The tip deflection recorded by SS-PFM equipment in unit of volt as shown in fig 6.9 and fig.6.10(5) can be converted into real film surface displacement in unit of nanometer:

$$h = v\gamma\beta \tag{6.13}$$

where, v is the tip deflection voltage shown in the piezoresponse loops. β defines the equipment sensitivity. The Asylum system for this measurement has a sensitivity of 1.2×10^{-4}. γ=47.03nm/V is the equipment calibration coefficient.

Though accurate surface displacement can be calculated using equation 6.13., accurate calculation of d_{zz} is difficult because of the inhomogeneous field distribution under the tip. Under this circumstance, d_{zz} can be roughly estimated as $d_{zz} = displacement / bias$ under an assumption that the strain and electrical field have same dependence on locations inside the film. Compared to the d_{zz} value obtained by others [52], d_{zz} from SS-PFM measurement (d_{zz}(100)~11pm/V, d_{zz}(110)~4pm/V, d_{zz}(111)~2pm/V) are about 1/5~1/6 of the value of their counterparts. (001) oriented $PbTiO_3$ has the strongest piezoresponse, (111) oriented $PbTiO_3$ has the weakest piezoresponse and piezoresponse from (110) oriented $PbTiO_3$ falls in between, which is largely due to their projection angle to [100] easy polarization direction. Considering the existence of ~50% *a* $PbTiO_3$ domains and the dissolution of Fe in $PbTiO_3$, the polarization is expected to be reduced by about 80%, which explains the weak piezoresponse we observe using SS-PFM. In addition, the nano-faceting structure also affects the polarization especially for our structures with small lateral size. The depolarization field is likely increased because of the nano-facets in case of {111} oriented film. For film of {110} orientation, effects of nano-facets on polarization is minimized by the coincidence of macro- and nanoscale interface which gives smooth {111} oriented interface.

6.5 Conclusion

The SS-PFM measurement shows possession of piezoelectricity and unambiguously domain switching under 10V bias for isolated $PbTiO_3$ nanoplatelets in {110} oriented film. However, 10V is not enough to drive the polarization to a saturated value. For lateral piezoresponse of (110) oriented film, PFM measurement shows no piezoresponse which is reasonable as the nanoplatelets are confined by matrix. For film of {111} orientation, domain switching is not observed for isolated $PbTiO_3$ nanorods under 10V bias using SS-PFM. However, piezoelectric response is proven by conventional PFM measurement. Weak lateral piezoresponse as shown in fig.6.12(3) and fig.6.12(4) is possibly due to the protruded $PbTiO_3$ above the film surface as illustrated in fig.6.12(5). (111) $PbTiO_3$ nanorods beneath the $CoFe_2O_4$ surface are confined by $CoFe_2O_4$ matrix and no lateral piezoresponse is expected. As piezoelectricity is a direct evidence of ferroelectricity for $PbTiO_3$, both (110) and (111) isolated $PbTiO_3$ nanostructures under confinement are ferroelectric. However, it is very unlikely to have extrinsic piezoeffect in these confined nanoferroelectrics under local electrical field due to mechanical constraint and depolarizing field. It is worth to mention that for <111> direction of electrical field, there is no preferent 90^o domains and extrinsic effect is impossible. Therefore, the SS-PFM measurement allows us to estimate intrinsic piezoeffect which is much weaker than the value measured with electrodes [52]. Roughly estimated value based on our SS-PFM measurement is about 10 times less than the bulk value (~79pm/V). For quantitative measurement of piezoelectric constant of confined nanoferroelectrics, more theoretical and experimental work needs to be done due to the complicated inhomogeneous field distribution and the unknown depolarizing field.

Summary

1. $PbTiO_3$-$CoFe_2O_4$ films with various compositions, thicknesses and orientations have been fabricated on $SrTiO_3$ substrates after a systematic study on PLD growth process of self-assembled biphasic films. It is found that growth temperature is sensitive and critical as Pb is volatile at elevated temperatures. Considerable impact on film quality can be seen for films grown at temperature 20K higher or lower than the optimum temperature. Each of the constituent phases has a growth temperature range for producing high quality single crystal film. Optimum growth temperature for two-phase self-assembled films is located in the overlap temperature range. This empirical finding could apply as well to other two-phase self-assembled epitaxial film growth using PLD. Oxygen environment is necessary to maintain stoichiometric Pb/Ti ratio, however, too much oxygen will create extra oxidized Pb phase (e.g., Pb_3O_4, PbO_2) with different valence state especially when $PbTiO_3$ is the majority phase. On the other hand, not enough oxygen pressure will result in nonstoichiometric Pb/Ti ratio. Therefore, the tolerant range for oxygen pressure is narrow. This leads to a rigid condition for target-substrate distance. Thus, the optimum growth conditions to obtain high quality films with distinct separation of epitaxial $PbTiO_3$ and $CoFe_2O_4$ nanophases corresponds to a very narrow range of growth parameters centered at substrate temperature (903K), oxygen pressure (100mTorr), target-substrate distance (~3.7cm) and laser fluence (~1.0J/cm^2).

2. Analysis of the two-phase morphologies and nanostructures of interfaces

between $PbTiO_3$ and $CoFe_2O_4$ phases shows that all interfaces have nano-facets along {111} plane. For films of {001} and {111} orientations, these nano-facets form macroscopic (average) interfaces which are normal to the substrate and have preferable orientations along {110} for {001} films and along {112} for {111} films. For {101} film, the {111} planes are perpendicular to the film/substrate interface; therefore go through the entire film thickness. Since the two-phase morphologies are described well by modeling based on the dominant role of elastic interaction between the phases, it is possible to conclude that the morphologies which are determined by the configuration of macroscopic interfaces are dictated by the trend of minimizing the elastic energy of internal stress while the faceting nanostructures of these interfaces minimize the interface energy. It can be suggested that faceting nanostructures of interfaces are important for relaxation of the internal stresses and electromagnetic/magnetoelectric properties of the films through the depolarizing and demagnetizing effects.

The study of small thickness films for all orientations shows that the $PbTiO_3/CoFe_2O_4$ interfaces deviate from the vertical direction near the substrate but reside on {111} planes. Direction of deviations determines the phase that covers the substrate during the initial growth stage and is determined by the energy of interface with substrate and surface energy. The $PbTiO_3/SrTiO_3$ interface energy is the lowest for all film orientations compared to $CoFe_2O_4/SrTiO_3$ interface energy because the crystal lattices of these phases are very close. However, the thermodynamics of the first few layers of deposited phases depends also on surface energy of these phases.

Therefore, for the {111} films, the substrate is covered by $CoFe_2O_4$ which has much lower surface energy than the surface energy of $PbTiO_3$. It may explain why $PbTiO_3$ forms matrix in {001} film while $CoFe_2O_4$ forms matrix in {111} film.

Thus we can conclude that accounting of interface and surface energies is important for description of nano-faceting of interfaces and the near substrate zone of the films while the two-phase morphology (shape, orientation and mutual arrangement of nanophases) is determined by the elastic interactions. Both contributions to thermodynamics should be included in theoretical model for design of controlled nanostructure.

3. The investigation of the stress state of the {001} film arising due to paraelectric-ferroelectric transition of $PbTiO_3$ have discovered the polydomain nanostructure of the ferroelectric phase. Relative fractions of the in-plane and out-of-plane domains are determined. It is found that only 50%-60% domains (*c*-domains) have polarization normal to the film. Together with the effect of dissolution of Fe in $PbTiO_3$, which decreases $PbTiO_3$ tetragonality (down to ~1.04 according to our estimation), existence of the *a* domains and constraint should lead to essential decrease of intrinsic piezoresponse of the film. Since the measurement of the piezoelectricity with cover electrodes gives a value of piezoelectric constant normal to film/substrate interface around 50pm/V while for bulk crystal it is about 80pm/V, we can conclude that this relative large piezoelectric constant contains large extrinsic contribution due to movement of nano-domain walls. This large extrinsic piezoeffect of $PbTiO_3$ phase is important for estimation of mechanical interaction between

$PbTiO_3$ and $CoFe_2O_4$ and their electromagnetic coupling. In principle, movable $PbTiO_3$ domains will diminish ME coupling while enhance EH coupling. Overall, formation of domains as a main mechanism of strain relaxation can exist in all self-assembled epitaxial films and needs to be considered carefully when dealing with composite multiferroic coupling.

4. Switching spectroscopy piezoresponse force microscopy (SS-PFM) is used to characterize local piezo- ferroelectric property of confined ferroelectrics in {110} and {111} oriented films with composition of $1/3PbTiO_3$-$2/3CoFe_2O_4$. It is proved that $PbTiO_3$ nano-inclusions exhibit ferroelectricity in both films. 180^o domain switching is observed under measurement condition (<10V) for the {110} oriented films but not for the {111} film. Quantitatively, both films yield a piezoresponse of about 15% compared to bulk single crystal $PbTiO_3$. It is a reasonable value of intrinsic piezoeffect taking into account mechanical and electrical constraints (depolarizing field) as well as the effect of Fe dissolution and possible in-plane domains.

Appendix.1 Growth parameters of 1/3$CoFe_2O_4$-2/3$PbTiO_3$ films

Substrate	Temp (K)	Distance (cm)	Laser Fluence (J/cm^2)	Repetition rate(Hz)	Oxygen (mTorr)	Pulses
STO(100)	903	6.5	0.7	10	100	54000
STO(100)	903	6.5	1.1	10	100	54000
STO(100)	903	6.5	1.1	10	100	72000
STO(100)	863	6.5	1.1	20	100	24000
STO(100)	863	6.5	1.1	20	65	48000
STO(110)	863	6.5	1.1	20	65	48000
STO(100)	903	4.5	1	20	65	48000
STO(100)	863	4.5	1	20	65	48000
STO(100)	863	4.5	1	20	100	48000
STO(100)	863	4.5	1	10	65	48000
STO(100)	608	4.5	1.1	10	65	48000
STO(100)	863	4.5	1.1	5	65	48000
STO(100)	863	4.5	1	10	100	48000
STO(100)	878	6.5	0.8	10	100	48000
STO(100)	878	6.5	0.7	5	100	24000
STO(100)	873	6.5	0.7	5	100	24000
STO(100)	883	6.5	0.7	5	100	24000
STO(100)	883	6.5	0.8	5	134	15000
STO(100)	883	6.5	0.8	5	165	15000
STO(100)	883	6.5	0.8	10	165	15000
STO(100)	883	6.5	0.8	3	165	15000
STO(100)	903	4.5	0.8	5	160	24000
STO(100)	881	4.5	0.8	5	160	24000
STO(100)	903	4.5	0.8	5	160	24000
STO(100)	888	4.5	0.8	5	160	24000
STO(100)	903	4.5	0.8	5	160	36000
STO(100)	898	4.5	0.8	5	160	24000
STO(100)	898	4.8	0.8	5	160	24000
STO(100)	898	4.5	1.7	5	100	24000
STO(100)	898	4.5	1.7	5	130	24000
STO(100)	898	4.5	1.6	5	100	24000
STO(100)	883	5.2	1.7	3	100	36000
STO(100)	898	5.5	1.7	5	100	24000
STO(111)	903	4.5	1.3	5	100	24000
STO(110)	903	3.6	0.9	5	100	24000
STO(111)	903	3.6	0.9	5	100	24000
STO(110)	903	3.6	0.9	5	100	24000
STO(111)	903	3.6	0.9	5	100	24000

Bibliography:

1 D. N. Astrov, *J. Exptl. Theor: Phys.* (USSR) Vo1.38, p.984, 1960. *[Sov. Phys. JETP* Vol.11, p.708, 19601

2 M.I. Bichurin, V.M. Petrov, and G. Srinivasan, *J. Appl. Phys.* Vo1.92, p.7681,2002.

3 M.I. Bichurin, V.M. Petrov, Yu.V. Kiliba, and G. Srinivasan,. *Phys. Rev.* B, Vol.66, p.134404, 2002.

4 D.A. Filippov, M.I. Bichurin, V.M. Petrov, V.M. Laletin, N.N. Poddubnaya, and G. Srinivasan: *Tech. Phys. Lett.* Vo1.30, p.6,2004.

5 S. Dong, J.F. Li, D. Viehland, J. Cheng, and L.E. Cross, *Appl. Phys. Lett.* Vo1.85, P.3534,2004.

6 S. Stein, M. Wuttig, D. Viehland, and E. Quandt, *J. Appl. Phys.* Vo1.97, p. 1 OQ30 1,2005.

7 V.M. Laletin, N. Paddubnaya, G. Srinivasan, C.P. De Vreugd, M.I. Bichurin, V.M. Petrov, and D.A. Filippov, *Appl. Phys. Lett.* Vo1.87, p.222507,2005.

8 D.A. Filippov, M.I. Bichurin, C.W. Nan, and J.M. Liu,. *J. Appl. Phys.* Vo1.97,p.113910,2005.

9 R.Ramesh and N. A. Spaldin, *Nature Mater.* Vo1.6, p.21,2007

10 H.Zheng, J.Wang, S.E.Lofland, Z.Ma, L.Mohaddes-Ardabili, T.Zhao, L.Salamanca-Riba, S.R.Shinde, S.B.Ogale, F.Bai, D.Viehland, Y.Jia, D.GSchlom, M.Wuttig, Roytburd, R.Ramesh, *Science,* Vo1.303, p.66 1,2004

11 L. Mohaddes-Ardabili, H. Zheng, Q. Zhan, S.Y. Yang, R. Ramesh, L. Salamanca-Riba, M. Wuttig, S.B. Ogale and X. Pan, *Appl. Phys. Lett.,* Vo1.87, p.203110,2005

12 HM. Zheng, F. Straub, Q. Zhan, PL. Yang, WK. Hsieh, F. Zavaliche, YH. Chu, U. Dahmen and R. Ramesh, *Adv. Mater:* Vo1.18, p.2747,2006

13 I.Levin, JH. Li, J.Slutsker, and A.L.Roytburd, *Adv. Mater.* Vol.18, p.2044,2006.

14 J. Slutsker, Z. Tan, A.L. Roytburd, I. Levin, *J. Mater: Res.* Vo1.22(8), p.2087,2007

15 S.Q. Ren and M. Wuttig, *Appl. Phys. Lett.,* Vo1.91, p.083501,2007

16 M.Murakami, K-S. Chang, M.A. Aronova, C-L. Lin, Ming H. Yu, J. Hattrick Simpers, M.Wuttig, I. Takeuchi, C.Gao, B.Hu, S.E.Lofland, L. A. Knauss and L. A. Bendersky, *Appl. Phys. Lett.,* Vo1.87, p.112901,2005

17 F. Jona and G. Shirane, Ferroelectric Crystals, 1993

18 J. Smit and H. P. J. Wijn, *Ferrites,* ed. N. V. Philips (Phlips Technical Library, Eindhoven, 1959).

19 M.J. Madou, *Fundamentals of Microfabrications* 2nd edition, 2002

20 A.Artemev, J.Slutsker and A.L.Roytburd, *Acta mater:* Vo1.53, p.3425~~2005

2 1 J.Slutsker, I.Levin, JH.Li, A.Artemev and A.L.Roytburd, *Phys. Rev.* B. Vo1.73, p. 184127,2006

22 HM. Zheng, Q. Zhan, F. Zavaliche, M. Sherburne, F1 Straub, M.P.Cruz, LQ. Chen, U. Dahmen and R. Ramesh, *Nono Lett.,* Vo1.6(7), p.1401,2006

23 W. S. Yun, J. J. Urban, Q.Gu and **HIS.** Park, *Nano Letters,* Vo1.2, p.447,2002

24 G. Suyal, E. Colla, R. Gysel, M. Cantoni and N. Setter, *Nano Letters,* Vo1.4, p.1339,2004

25 Z. L. Wang and J.H. Song, *Science,* Vo1.312, p.242,2006

26 S. Jesse, A. P. Baddorf and S.V. Kalinin, *Appl. Phys. Lett.* Vo1.88, p.062908,2006

27 F. Leonard and R.C. Desai, *Appl. Phys. Lett.* Vo1.73, p.208, 1998

28 F. Leonard and R.C. Desai, *Phys. Rev.* B, Vo1.57, p.4805,1998

29 M. Atzmon, D. A. Kessler and D. J. Srolovitz, *J. Appl. Phys.* Vo1.72, p.442, 1992

30 A.L.Roytburd, *J. Appl. Phys.* Vo1.83(1), p.228, 1998

3 1 A.L.Roytburd, *J. Appl. Phys.* Vo1.83(1), p.239, 1998

32 A. G. Khachaturyan, *Theory of Structural Transformations in Solids,* Wiley, New York 1983.

33 A. Artemev, Y. Jin, A. G. Khachatutyan, *Acta Mater:,* Vo1.49, p.1165.2001

34 I. M. Kaganova and A.L.Roitburd, *Kristallorgrajiya (Sov. Phys. Crystallogr:*), Vo1.34, p.1076, 1989

35 B.D. Chapman, E.A. Stem, S.W. Han, J.O. Cross, GT. Seidler, V.Gavrilyatchenko, R.V. Vedrinskii and V. L. Kraizman, *Phys. Rev.* B. Vo1.71, p.020102,2005

36 Z.R. Chen, S.W. Yu, L. Meng and Y. Lin, *Compos. Struct.* Vo1.57, p.177,2002

37 A.L.Roitburd, *Phys. Status Solidi A* Vo1.37, p.329,1976

38 W.L. Winterbottom, *Acta Metall.* Vo1.15, p.303, 1967

39 Dijkkamp, D., et al. *Appl. Phys. Lett.,* Vo1.51, p.6 19, 1987

40 D. Chrisey, G. K. Hubler, *PulsedLaser Deposition of Thin Films,* Wiley, 2003

41 J. F. Ready. *Appl. Phys. Lett.,* Vo1.3(1), p. 11 -1 3, 1963

42 J.F. Ready, *JofAppl Phys,* Vo1.36(2), p462-468, 1964

43 Yu. V. Afanasev and O.N. Krokhin, *Soviet Physics JETP,* Vo1.25(4), p.639 1967

44 C.R.M. Grovenor, H.T.G.hentze11 and D.A. Smith, *Acta metal.* Vo1.32(5), p.773, 1984

45 Y. Shibata, K.Kaya, K.Alkashi, et al. *Appl. Phys. Lett.* Vo1.61, p.1000, 1992

46 H. Koinuma, H.Nagata, T.Tsukahara, S.Gonda, and M.Yoshimoto, *Appl. Phys. Lett.* Vo1.58, p.2027 1991

47 K. Nashimoto, D.K. Fork, and T.Geballe, *Appl. Phys. Lett.* Vo1.60, p1199, 1992

48 Leuchtner, R.E., J.S.Horowitz, and D.B. Chrisey, *Matel: Res. Soc. Symp. Proc.* Vo1.285, p87, 1993

49 Hitoshi Tabata, Tomoji Kawai, Shichio Kawai, Osamu Murata, Junzo Fujioka and Shun-ichi Minakata, , *Appl. Phys. Lett.* Vo1.59, p.2354, 1991

50 P.C. Dorsey, P. Lubitz, D.B. Chrisey and J.S. Horwitz, *J. Appl. Phys.* Vo1.79(8), p.6338, 1996

51 K.Mohan Kant and M.S. Ramachandra Rao, *Mater Res. Symp. Proc.* Vo1.962, 0962-P09-08, 2007

52 J.H. Li, Dissertation, University of Maryland at College Park, 2006
53 C.D. Adams, M.Atunon, Y.T.Cheng, D.J. Srolovitz,, *J. Mater Res.* Vo1.7(3), p.653, 1992
54 H.Zheng, Dissertation, University of Maryland at College Park, 2004
55 J. Lappalainen, J. Frantti and V. Lantto, *Appl SurJ: Sci* Vo1.142 p.407, 1999
56 D.B. Geohegan, *Appl. Phys. Lett.,* Vo1.60, p.2732, 1992
57 T. Venkatesan, X.D. Wu, A.Inam and J.B.Watchman, *Appl. Phys. Lett.* Vo1.52, p. 1193, 1987
58 H.S. Kim and H.S.Kwok, *Appl. Phys. Letts.* VoL61(18), p.2234, 1992
59 U. Sudarshan, N.w.Cody, M.J.Bozack and R.Solanki, *LMatel: Res.* Vo1.3 p.825 1988
60 R.K.Singh, O.W. Hollan and J.Narayan, *J Appl. Phys.* Vo1.68(1), p.233,1990
61 YB. Yao, SG. Lu, H. Chen, J. Zhao and K. Wong, *J. Appl. Phys.,* Vo1.96, p.569,2004
62 L.S. Hong and C.C. Wei, Materials Letters, Vo1.46, p.149,2000.
63 T. Nakamura, Y.Yamanaka, A. Morimoto and T. Shimizu, *Jpn. J. Appl. Phys.* Vo1.34, p.5150, 1995.
64 Dwight E. Gray, *American Institute of Physics Handbook,* 3th Edition, 1972
65 0. Auciello, R. Krauss, J.Santiago-Susles, P.F.Schreiner, and D.M.Gruen, *Appl. Phys. Lett.,* Vo1.52(3), p.239, 1988
66 S.R. Foltyn, R.C.Dye, K.C.Ott, E.Peterson, W.B.Hutchinson, K.M.Hubbard, R.E. Muenchausen, R.C.Estler and X.D.Wu, *Appl. Phys. Lett.,* Vo1.59(5), p.594, 1991
67 Meyer, B.; Padilla, J.; Vanderbilt, D. *Faraday Discuss.,* Vo1.114, p.395, 1999
68 R. I. Eglitis and David Vanderbilt, *PHYSICAL REVIEWB* Vo1.76, p.155439,2007
69 H. Zheng, J. Wang, L. Mohaddes-Ardabili, M. Wuttig, and L. Salamanca-Riba, D. G Schlom, R. Ramesh, *Appl. Phys. Lett.,* Vo1.85, p.2035,2004
70 M.J.Haun, E.Furman, S.J.jang, H.A.McKinstry and L.E.Cross, *J.Apl.Phys.* Vo1.62, p.3331, 1987
71 M.J. haun, E.Furman, H.A.McKinstry and L.E.Cross, *Ferroelectrics,* Vo1.99, p.27, 1989
72 V.R. Palkar and S.K. Malik, *SolidState Comm.,* Vo1.134, p.783,2005
73 A.L.Roytburd and J.Slustker, *J. Mech. Phys. Solids* Vo1.49, p. 1795,2001
74 Q.Jiang and J.H.Qiu, *J. OfAppl. Phys.,* Vo1.99, p.103901,2006
75 N. Setter and D.Damjanovic et. al. *J. OfAppl. Phys.* Vo1.100, p.05 1606,2006
76 S.H.Ahn, W.W.Jung and S.K.Choi, *Appl. Phys. Lett.,* Vo1.86, p.172901,2005
77 JH.Li, I.Levin, J.Slutsker, V.Provenzano, P.K.Schenck, R.Ramesh, J.Ouyang and A.L.Roytburd, *Appl. Phys. Lett.* Vo1.87, p.072909,2005
78 B.T.Cong, N.N.Dinh, D.V.Hien, N.L.Tuyen, *Physica B,* Vo1.327, p.370,2003
79 D.R. Patil, S.A. Lokare, R.S. Devan, S.S. Chougule, Y.D. Kolekar and B.K. Chougule, *J of Physics and Chemistry of Solids* Vo1.68, p.1522,2007
80 Y. Yamazaki and M. Satou, *Jan. J. ofApp1. Phys.* Vo1.12(7), p.998, 1973

81 P.Guthner and K.Dransfei1, *Appl. Phys. Lett.* Vo1.61, p. 1137, 1992

82 Alexei Gruverman, Orlando Auciello and Hiroshi Tokurnoto, Annu. Rev. Matel: Sci. Vo1.28 p.101, 1998

83 S.V. Kalinin and Dawn A. Bonnell, Phys. Rev B. Vo1.65 p.125408,2002

84 S. V. Kalinin, Andrei Rar and Stephen Jesse, IEEE Transactions of Ultrasonics, Ferroelectrics, and Frequency Control, Vo1.53(12), p.2226,2006

85 A. Gruverman and S.V.Kalinin, *J.* Mater: Sci. Vo1.41, p.107,2006

86 C. B. Sawyer and C. H. Tower, Physical Review Vo1.35, p.269, 1930

87 J.K.Sinha, *J.* Sci. Instrum., Vo1.42 p.696, 1965

88 V. Hugo Schmidt, Am. *J.* Phys., Vo1.37, p.35 1, 1969

89 M.E.Caspari and W.J.Merz, Phys. Rev. Vo1.80(6), p.1082, 1950

90 Dragan Damjanovic, Rep. Prog. Phys. Vo1.61, p.1267, 1998

91 A.Morozovska, E.A.Eliseev, S.L.Bravina, S.V.Kalinin, Phys. Rev. B. Vo1.75, p.174109,2007

92 B.J.Rodriguez, S.Jesse, A.P.Baddorf, T.Zhao, Y.H.Chu, R.Ramesh, E.A.Eliseev, A.N.Morozovska and S.V.Kalinin, Nanotechnology, Vo1.18, p.405701 2007

93 J. Ouyang, S.Y.Yang, L.Chen, R.Ramesh and A.L.Roytburd, Appl. Phys. Lett., Vo1.85(2), p.278,2004